INFORMATION TO USERS

This reproduction was made from a copy of a manuscript sent to us for publication and microfilming. While the most advanced technology has been used to photograph and reproduce this manuscript, the quality of the reproduction is heavily dependent upon the quality of the material submitted. Pages in any manuscript may have indistinct print. In all cases the best available copy has been filmed.

The following explanation of techniques is provided to help clarify notations which may appear on this reproduction.

1. Manuscripts may not always be complete. When it is not possible to obtain missing pages, a note appears to indicate this.
2. When copyrighted materials are removed from the manuscript, a note appears to indicate this.
3. Oversize materials (maps, drawings, and charts) are photographed by sectioning the original, beginning at the upper left hand corner and continuing from left to right in equal sections with small overlaps. Each oversize page is also filmed as one exposure and is available, for an additional charge, as a standard 35mm slide or in black and white paper format.*
4. Most photographs reproduce acceptably on positive microfilm or microfiche but lack clarity on xerographic copies made from the microfilm. For an additional charge, all photographs are available in black and white standard 35mm slide format.*

***For more information about black and white slides or enlarged paper reproductions, please contact the Dissertations Customer Services Department.**

UMI University Microfilms International

Lu, Xing-Ze

RESONANT-BRILLOUIN-SCATTERING STUDIES OF THE A-EXCITON IN CADMIUM SULPHIDE

City University of New York PH.D. 1985

University
Microfilms
International 300 N. Zeeb Road, Ann Arbor, MI 48106

RESONANT-BRILLOUIN-SCATTERING STUDIES OF THE A-EXCITON IN CADMIUM SULPHIDE

By

XING-ZE LU

A dissertation submitted to the Graduate Faculty in Physics in partial fulfillment of the requirements for the degree of Doctor of Philosophy, The City University of New York.

1985

This manuscript has been read and accepted for the Graduate Faculty in Physics in satisfaction of the dissertation requirement for the degree of Doctor of Philosophy.

September 23, 1985
date

Chairman of Examining Committee

Sept 23, 1985
date

Executive Officer

Myriam P. Sarachik
Joseph L. Birman

Supervisory Committee

The City University of New York

Abstract

RESONANT-BRILLOUIN-SCATTERING STUDIES
OF THE A-EXCITON IN CADMIUM SULPHIDE

by

Xing-Ze Lu

Adviser: Professor Herman Z. Cummins

High-resolution resonant-Brillouin-scattering experiments in the spectral region of the A-exciton in cadmium sulphide were performed at liquid-helium and superfluid-helium temperatures with a single-mode tunable dye laser and a Fabry-Perot interferometer followed by a double-grating spectrometer. A frequency-dependent polariton damping model was proposed to quantitatively explain the observed RBS linewidth behavior near the exciton resonance. We have given the first evidence for the k-linear interaction in the A-exciton in CdS by performing RBS experiments in a weak magnetic field. We also observed three-branch polariton behavior and measured the k-linear coefficient of the A-exciton in CdS for the first time by performing RBS experiments at superfluid-helium-temperatures. We have shown that frequency-dependent polariton damping is crucial for solving the additional boundary condition (ABC) problem from RBS intensity measurement. None of the three commonly used ABCs agree with the RBS experiments. A fit of the theoretical intensity curve calculated from a generalized ABC and the frequency-

dependent damping model to the observed intensity data indicates that the dead layer effect is negligible in the A-exciton in CdS and the correct choice of ABC falls between ABC 1 and ABC 2 but close to ABC 2.

ACKNOWLEDGEMENTS

I am indebted to Professor Herman Z. Cummins for his continued support, encouragement and patient guidance during the course of this research.

I am extremely grateful to Dr. Takeshi Shigenari for his important contributions in the resonant-Brillouin-scattering (RBS) linewidth and intensity investigations and the construction of the frequency-dependent polariton damping model.

I am grateful to Dr. Mitra Dutta for her collaboration in the magneto-RBS and RBS experiments at superfluid-helium-temperature. I thank Dr. James Wicksted and Dr. Mitsugu Matsushita for their participation in the early stage of this research and important contributions to our high-resolution RBS apparatus. I thank Prof. J. L. Birman, Dr. S. Geschwind, Dr. E. J. Flynn, Dr. E. S. Koteles, Prof. M. P. Sarachik, and Prof. F. Pollak for their helpful discussions and advice. I thank all the current members of the light scattering group, Prof. H. Cummins, Dr. M. Dutta, Dr. Tarlok Aurora, Dr. Gabriela Livescu, Mr. Shen-Li Qiu, Mr. Henry Chou, Miss Wen Li, Prof. Guang-Yin Zhang, and Mrs. Frances Tritt, and former members Dr. M. Matsushita, Mr. Ben-Yuan Gu, Dr. J. Wicksted, Dr. Dennis Neal, Dr. T. Shigenari, Dr. Mohammed Awal, and Dr. Oscar Mesquita.

I thank Prof. Z. M. Zhang, Prof. Y. F. Li, Prof. G. J. Ni, Prof. Z. Y. Wang and President X. D. Xie of Fudan University, and Prof. N. P. Chang and Prof. C. Yuan of CCNY for their help and encouragement before and after I came to the United States.

DEDICATION

I dedicate this thesis to my father De-Pei Lu, my mother Yu-Fang Shi, my wife Hui-Na Zhang for their love and comprehension during this work.

TABLE OF CONTENTS

LIST OF TABLES

LIST OF FIGURES

Chapter 1 . Introduction

Since the pioneering paper by Brenig, Zeyher, and Birman (BZB),[1] many resonant Brillouin scattering (RBS) experiments have been performed on nonmetallic crystals such as GaAs, Cu_2O, CdS, and CdSe. It was shown that the kinematics of RBS (i.e. the dependence of the Brillouin shift on the incident laser frequency) was very well fitted by BZB's theory. However, other interesting and important dynamical aspects including the Brillouin linewidth and integrated scattered intensity have not yet been clarified. The research discussed in this thesis was designed to explore these dynamical aspects of the theory in the wurtzite-structure semiconductor CdS.

Before presenting our theoretical and experimental investigations on RBS, we present in this chapter some elementary concepts and preliminary background information. Throughout the thesis, we will use $\tilde{\omega} = \omega/(2\pi c)$ to represent frequency expressed in units of cm^{-1}, with a similar definition for the damping constant $\tilde{\gamma}$, and $\tilde{k} = k/(2\pi)$ to represent wave number expressed in units of cm^{-1}.

1.1. Exciton

An exciton is an elementary electronic excitation in nonmetallic solids exhibiting hydrogen-like energy levels of the Coulomb-bound electron-hole pair.

1. Electronic Excitation

In atomic physics one usually neglects the interaction between atoms. Using the central field approximation, each electron is considered to be moving independently in a self-consistent Coulomb potential due to a single isolated nucleus (or ion) and the other electrons in the same atom. The electronic excitations can be described by a series of atomic orbits.

In solid state physics, one considers the periodic structure of crystals and the interaction between this structure and the electrons. Using the energy band approximation, each electron is considered to be moving independently in an averaged self-consistent periodic potential due to all the nuclei (or ions) and the other electrons in the crystal. The electronic excitations can be described by a series of energy bands.

When an electron is excited from a full valence band to an empty conduction band, an additional interaction between the excited electron and the hole it leaves behind appears as a part of the energy gain due to the transition. This interaction, which is neglected in the band scheme, causes the formation of hydrogen-like bound states of an electron and a hole. The compound particle formed by an electron in a conduction band and a hole in a valence band is referred to as an exciton. Therefore the exciton scheme is a more complete description of electronic excitations in solids than the band scheme.

In metals the exciton lifetime is extremely short (~ 10^{-16} sec.) due to the screening effect of the electron-hole interaction by conduction electrons. Electrons and holes essentially move independently of each other and the band scheme is a good approximation for the description of electronic excitations. However, in semiconductors and insulators, the population of conduction electrons as well as screening effects are negligibly small under normal conditions because of the large energy gap between the highest valence band and the lowest conduction band; thus excitons can live long enough (~ 10^{-11} sec.) so that the exciton scheme is necessary to describe the electronic excitations in these crystals.

2. Frenkel and Wannier Excitons

Excitons whose radii are comparable to the lattice constant and which are localized are referred to as Frankel excitons. Mobile excitons with a radius much larger than the lattice constant are called Wannier excitons. The excitons in the semiconductor CdS are Wannier excitons. In the following we only discuss Wannier excitons.

3. Exciton Wave Functions and Degrees of Freedom[2]

Using the two-particle model and effective mass approximation, the equation of motion for an exciton in an isotropic medium is given by

$$\left[-\frac{\hbar^2\nabla_e^2}{2m_e} - \frac{\hbar^2\nabla_h^2}{2m_h} - \frac{e^2}{\varepsilon|\mathbf{r}_e - \mathbf{r}_h|} + E_g \right] \psi = E\,\psi \,. \tag{1.1}$$

Making a transformation

$$R = \frac{m_e\mathbf{r}_e + m_h\mathbf{r}_h}{m_e + m_h} \,, \quad \mathbf{r} = \mathbf{r}_e - \mathbf{r}_h \tag{1.2}$$

where **R** is the center of mass coordinate of the exciton and **r** is the relative (electron-hole) coordinate, we obtain

$$\left[-\frac{\hbar^2\nabla_{\mathbf{r}}^2}{2\mu} - \frac{\hbar^2\nabla_R^2}{2M} - \frac{e^2}{\varepsilon r} + E_g \right] \psi = E\,\psi \tag{1.3}$$

where

$$\mu = \frac{m_e m_h}{m_e + m_h} \,, \quad M = m_e + m_h \,, \tag{1.4}$$

μ is the reduced mass and M is the total mass. The exciton wave functions and energy levels are obtained by solving Eq. (1.3):

$$\psi(\mathbf{r}_e,\mathbf{r}_h) = \exp(i\mathbf{k}\cdot\mathbf{R})\,\phi_{nlm}^{(\varepsilon)}(\mathbf{r})\,u_{c_0}(\mathbf{r}_e)\,u_{v_0}(\mathbf{r}_h) \tag{1.5}$$

$$E_n(\mathbf{k}) = E_g - \frac{\mu e^4}{2\hbar^2\varepsilon^2 n^2} + \frac{\hbar^2 k^2}{2M} \tag{1.6}$$

where $\phi_{nlm}^{(\varepsilon)}(\mathbf{r})$ are the hydrogenic envelope functions in a medium of dielectric constant ε, while u_{c_0} (u_{v_0}) are the periodic parts of the Bloch functions in the conduction (valence) band at $\mathbf{k} = 0$.

Since the excitons formed from two given bands may have both translational motion and internal motion of the electron relative to the hole, the following information is needed to specify an exciton state:

(a) from which conduction and valence band an exciton is formed,

(b) quantum numbers of the internal motion,

(c) wave vector **k** of the translational motion,

(d) spins of the electron and the hole.

4. Symmetry Properties of Excitons

At **k** = 0, the symmetry of an exciton state is determined by the point symmetries of the conduction band, valence band, and the envelope function (wave function of the internal motion), and the spin wave function. Thus we may characterize the exciton states by their point symmetries at **k** = 0, e.g. the ground state (1s) of the A-exciton in CdS at **k** = 0 consists of four substates of point symmetries Γ_5 , Γ_5 , Γ_6 , and Γ_6, respectively. The first two are spin singlet states in which the electron spin is anti-parallel to the hole spin, and the other two are spin triplet states in which the electron spin is parallel to the hole spin.

5. L-T Splitting and Exciton Dispersion

Using the classical harmonic oscillator model we easily obtain the dielectric function near an exciton resonance in an isotropic medium:

$$\varepsilon = \varepsilon_b + \frac{4\pi\alpha_0\omega_0^2}{\omega_0^2 + (\frac{\hbar\omega_0}{M})\,k^2 - \omega^2 - i\omega\gamma} . \tag{1.7}$$

The transverse exciton modes occur at the poles of ε. Thus their dispersion relation is

$$\omega = \omega_0 + \frac{\hbar k^2}{2M} , \tag{1.8}$$

where $\omega_0 = \omega_T$. The longitudinal exciton mode occurs at the zero of ε. Thus its dispersion relation is

$$\omega = \omega_L + \frac{\hbar k^2}{2M} \tag{1.9}$$

where

$$\omega_L = \omega_0 \left[1 + \frac{4\pi\alpha_0\omega_0}{\varepsilon_b} \right]^{\frac{1}{2}} . \tag{1.10}$$

6. Observation of Excitons

The structure of excitons depends critically upon the temperature. When the temperature increases, the band gap and the energy separations between exciton levels decrease. On the other hand, the exciton lifetime decreases due to the increase in the number of free electrons and holes (which screen the Coulomb interaction between the electron and hole in an exciton) and phonons (which scatter excitons or cause phonon-related broadband background emissions). In order to observe excitons clearly one must keep the samples at very low temperatures, e.g. liquid nitrogen or liquid helium temperatures.

The first indication of a possible hydrogenic exciton series in CdS was observed in absorption measurement by Gross et al in 1957, and in reflectivity measurements by Dutton in 1958 and Thomas and Hopfield in 1959.

1.2. Polariton

1. Polariton, Phonon-Polariton and Exciton-Polariton

The mechanical modes (phonon, exciton, plasmon etc.) in a dielectric medium produce polarizations which couple to the electromagnetic waves in the medium. Polaritons are the composite particles formed by the coupled polarizations and photons.

The polaritons are referred to as phonon-polaritons if the polarization is produced by polar optical phonons, or exciton-polaritons if the polarization is produced by excitons. In the following we discuss only exciton-polaritons.

2. Polariton Dispersion Relation

Since the electromagnetic waves in an isotropic medium are transverse waves, they will only couple to the transverse dipole-allowed exciton modes propagating in the same direction. The dispersion relation of the transverse polariton modes is given by

$$\frac{c^2k^2}{\omega^2} = \varepsilon(\omega,\mathbf{k}) \qquad (1.11)$$

where ε is the dielectric function of the medium.

In the vicinity of the Brillouin zone center the polar optic phonon energy and its contribution to the dielectric function are independent of **k**; thus media with only phonon-polaritons will display classical dispersion. However, media with exciton-polaritons will display spatial dispersion (i.e. dependence of ε on **k**) due to the **k**-dependence of the free exciton energy. In the presence of s non-interacting exciton states, the exciton-polariton dispersion is given by

$$\frac{c^2k^2}{\omega^2} = \varepsilon_b + \sum_{j=1}^{s} \left[\frac{4\pi\alpha_j\omega_j^2}{\omega_j^2 + (\frac{\hbar\omega_j}{M_j})\,k^2 - \omega^2 - i\omega\gamma_j} \right] \qquad (1.12)$$

where ω_j is the j'th exciton (internal motion) frequency, $4\pi\alpha_j$ is the oscillator strength, γ_j is the polariton damping essentially due to exciton scattering by phonons, impurities etc., and M_j is the effective translational mass. Since we will consider processes stationary in time, ω in Eq. (1.12) is real but **k** can be complex.

3. Significance of the Polariton Picture

Since excitons excited by light are always coupled to photons, in principle all phenomena related to optically generated excitons should be described in terms of the polariton picture. However, if the coupling between excitons and photons is relatively weak compared to other interactions involved in the process, as in resonant

Raman scattering (RRS)[3] and optical absorption,[4] one may use the bare exciton picture. In RBS, as it will be shown later, the polariton picture is absolutely necessary to explain all the relevent phenomena.

1.3. Spatial Dispersion

1. Definition

The variation with wave vector of the susceptibility (or dielectric function) tensor of a medium is referred to as spatial dispersion, or equivalently, the nonlocal response of the medium to the external electric field is called spatial dispersion. In a spatially dispersive medium, energy is transported not only via the electromagnetic waves, but also via the coupled polarization waves.

2. Anomalous Waves and Necessity of the Additional Boundary Condition (ABC)

Consider light normally incident on the boundary of a medium which has only one optically active exciton state in the vicinity of the light frequency. In the normal incidence case, only the transverse polariton modes are excited in the medium whose dispersion relation is then given by

$$\frac{c^2k^2}{\omega^2} = \varepsilon_b + \frac{4\pi\alpha_0\omega_0^2}{\omega_0^2 + (\frac{\hbar\omega_0}{M})\,k^2 - \omega^2 - i\omega\gamma}. \qquad (1.13)$$

Fig. 1.1 is the schematic representation of Re $k(\omega)$ vs. ω in the A-exciton region in CdS at T = 4.2 K according to Eq. (1.13). For each $\omega > \omega_L$, there exist two polarization modes (anomalous waves, or Pekar waves) with the same propagation direction and the same polarization direction but different wave vectors in the spatially dispersive medium. The amplitudes of the two transmitted polariton modes and the reflected wave cannot be ascertained solely by the Maxwell boundary conditions. An additional boundary condition (ABC) is needed to determine the relative amplitude of the two polariton modes. Note that in the oblique-incidence case, there will be also a longitudinal exciton wave in the medium. Thus two ABCs are required to determine the amplitudes of the three transmitted waves.[5]

In Fig. 1.1, ω_L is the onset frequency of the upper transverse polariton branch. We can obtain this frequency by setting $k = 0$ in Eq. (1.13), but this turns out to be exactly the same condition as the one for the longitudinal exciton frequency at $k = 0$. Thus the onset frequency of the upper transverse polariton mode is the same as the frequency of the bare longitudinal exciton mode at $k = 0$.

1.4. Additional Boundary Conditions

ABC is concerned with the surface behavior of the exciton-polaritons in a spatially dispersive medium.

1. Three Representative ABCs

(1) ABC 1 (Pekar)[5]

The sum of the exciton polarizations must vanish at the crystal boundary:

$$\sum_{i=1}^{2} P_{e_i} = 0 \quad \text{at} \quad x = 0 \tag{1.14}$$

where the x-axis is perpendicular to the crystal surface , and P_{e_i} denotes the exciton polarization associated with the i'th polariton mode. Note that the total polarization associated with the i'th polariton mode is

$$P_i = P_{e_i} + P_{b_i} = P_{e_i} + \chi_b E_i = P_{e_i} + \left(\frac{\varepsilon_b - 1}{4\pi}\right) E_i ,$$

where P_{b_i} is the "background" polarization due to other degrees of freedom and χ_b is the associated "background" permittivity. Since

$$P_i = \left(\frac{n_i^2 - 1}{4\pi}\right) E_i ,$$

we can relate P_{e_i} to E_i by

$$P_{e_i} = \left(\frac{n_i^2 - \varepsilon_b}{4\pi}\right) E_i \tag{1.15}$$

where E_i is the electric field associated with the i'th polariton mode, and

$$n_i = \frac{ck_i}{\omega} \tag{1.16}$$

is the complex refractive index of the i'th polariton mode. Thus we can rewrite Eq. (1.14) in terms of E_i:

$$\sum_{i=1}^{2} (n_i^2 - \varepsilon_b) E_i = 0 \,. \tag{1.17}$$

(2) ABC 2 (Ting et al)[6]

We may write ABC 2 as follows:

$$\sum_{i=1}^{2} n_i P_{e_i} = 0 \qquad \text{at} \quad x = 0 \tag{1.18}$$

or in terms of E_i:

$$\sum_{i=1}^{2} n_i (n_i^2 - \varepsilon_b) E_i = 0 \,. \tag{1.19}$$

(3) ABC 3 (Dielectric Approximation)[7,8,9]

We may write ABC 3 as follows:

$$\sum_{i=1}^{2} \frac{P_{e_i}}{(n_i - n_e)(n_i^2 - \varepsilon_b)} = 0 \qquad \text{at} \quad x = 0 \,, \tag{1.20}$$

or in termes of E_i:

$$\sum_{i=1}^{2} \frac{E_i}{n_i - n_e} = 0 \tag{1.21}$$

where n_e is the refractive index of bare transverse excitons:

$$n_e = \frac{ck_e}{\omega} \qquad (1.22)$$

and k_e is the wave vector of bare excitons determined by the poles of the dielectric function:

$$k_e^2 = \left(\frac{M}{\hbar\omega_0}\right)(\omega^2 - \omega_0^2 + i\omega\gamma) \, . \qquad (1.23)$$

2. A Simple Generalized ABC[10]

The three representative ABCs were shown to be special cases of a simple (excluding surface effect of excitons) generalized ABC:

$$\sum_{i=1}^{2} \left[\frac{1}{k_i - k_e} + \frac{S}{k_i + k_e}\right] E_i = 0 \, , \qquad (1.24)$$

where S is the exciton reflection coefficient introduced through the exciton wavefunction near the surface

$$\psi_k(x) = [\exp(-ik_{ex}x) + S\exp(ik_{ex}x)]\,\theta(x) \, .$$

Rewriting the polariton dispersion relation as

$$n_i^2 - \varepsilon_b = \frac{4\pi\alpha_0\omega_0^2}{\frac{\hbar\omega_0}{M}} \, \frac{1}{n_i^2 - n_e^2}$$

we can easily reduce this simple generalized ABC to ABC 1, 2, and 3 by setting S = -1, 1, and 0, respectively.

1.5. Resonant Brillouin Scattering

1. Definition

Brillouin scattering is the scattering of light by acoustic phonons. The quantum theory of light scattering, developed by Loudon, considered free electrons and holes as the intermediate states. Subsequently, BZB[1] showed that RBS is light scattering by acoustic phonons via exciton-polaritons as intermediate states in the vicinity of an exciton resonance in a spatially dispersive medium where the polaritons are strongly exciton-like. A backward RBS process is shown schematically in Fig. 1.2.

RBS is a powerful technique for studying exciton-polaritons and spatial dispersion. Using this technique, accurate measurements of the Brillouin shift can be obtained, yielding accurate determinations of the exciton parameters such as the effective mass, transverse exciton frequency, L-T splitting etc. In addition, linewidth measurements provide information on polariton lifetimes while intensity measurements can be used to determine the ABC.

2. Predictions of BZB's Theory

According to BZB's theory, as the incident laser frequency scans upward through the exciton resonance, there should be:

(1) A rapid increase in Brillouin shift due to the curvature of the lower polariton branch (branch 2) near ω_o. The Brillouin shift is very sensitive to the exciton parameters, especially the exciton effective mass.

(2) A Brillouin octet resulting from the two-branch polariton model instead of the usual Brillouin doublet which is observed when

the incident laser frequency ω_I is well below ω_0.

(3) An increase in the Brillouin linewidth due to the onset of the upper polariton branch (branch 1) when $\omega_I > \omega_L$. The Brillouin linewidth is sensitive to the polariton damping constant, which is closely related to the exciton-polariton lifetime.

(4) The scattering cross section (integrated intensity) for different Brillouin components should be strongly frequency-dependent and very sensitive to the choice of ABC.

Based on BZB's theory, Matsushita et al have recently developed a factorization procedure to calculate RBS cross sections numerically.[11] The differential cross section for backward Stokes-RBS from the i'th to the j'th polariton branch is given by

$$\frac{d^2\sigma}{d\Omega\, d\omega} = \frac{A\,[1 + n_{\mathrm{phonon}}(\omega_{Ii} - \omega_{Sj})]}{(2\pi)^3\,(\hbar c)^2\, c_S}\; T_i(\omega_{Ii})\; T_j(\omega_{Sj})\; \frac{\omega_{Sj}^{\;2}\, \left| A_{ij}(\mathbf{k}_{Ii}, \mathbf{k}_{Sj}) \right|^2}{V_{Ei}(\omega_{Ii})\, \left| V_{Gj}(\omega_{Sj}) \right|}$$

$$\times \left| \Gamma_0(\mathbf{q} = \mathbf{k}'_{Ii} - \mathbf{k}'_{Sj}) \right|^2 \times \frac{1}{\left(k'_{Ii} + k'_{Sj} - \frac{\omega_{Ii} - \omega_{Sj}}{c_S}\right)^2 + \left(k''_{Ii} + k''_{Sj}\right)^2} \qquad (1.25)$$

where $T(\omega)$ is the ABC-dependent transmissivity of photons at the crystal boundary, V_E and V_G are the energy and group velocities of polaritons, A_{ij} is the exciton strength function which measures the proportion of exciton-like behavior in the polariton under consideration, $\mathbf{k}_I = \mathbf{k}'_I + i\mathbf{k}''_I$ and $\mathbf{k}_S = \mathbf{k}'_S + i\mathbf{k}''_S$ are the complex wave vectors of the incident and scattered polaritons, A is the illuminated area on the crystal surface and c_S is the sound velocity.

The exciton-phonon interaction kernal $\Gamma_0(\mathbf{q})$ is given by

$$\Gamma_0(q) = \left(\frac{\hbar}{2\rho c_{LA}}\right)^{\frac{1}{2}} q^{\frac{1}{2}} (D_e + D_h) \tag{1.26}$$

for LA phonons, and

$$\Gamma_0(\mathbf{q}) = \frac{2\pi e a^2\, e_{15}}{\varepsilon_b} \left(\frac{\hbar}{2\rho c_{TA}}\right)^{\frac{1}{2}} q^{\frac{3}{2}} \left(\frac{m_e - m_h}{m_e + m_h}\right) \tag{1.27}$$

for TA phonons. The parameters c_{LA}, c_{TA}, ρ, D_e, D_h, e_{15} etc. for CdS are given in Table 1.4.

Since the last factor in Eq. (1.25) is the only one which strongly depends on frequency, the scattered spectrum is expected to have a Lorentzian line shape. Thus the Stokes Brillouin shift will be

$$\Delta = \omega_{Sj} - \omega_{Ii} = - c_S \left| k'_{Ii} + k'_{Sj} \right| \tag{1.28}$$

and the Brillonin linewidth

$$\delta = 2\, c_S \left| k''_{Ii} + k''_{Sj} \right| . \tag{1.29}$$

As originally pointed out by Sandercock, this linewidth is determined by the uncertainty of the phonon wave vector $\mathbf{q}$, and $(k''_I + k''_S)^{-1}$ represents the effective scattering length in which RBS takes place.[12] Damping of the acoustic phonons, which would also contribute to the RBS linewidth, can be neglected at liquid helium temperatures.

The integrated intensity is given by

$$\frac{d\sigma}{d\Omega} = \pi A \frac{[1 + n_{phonon}(\omega_{Ii} - \omega_{Sj})]}{(2\pi)^3 (\hbar c)^2} T_i(\omega_{Ii})\, T_j(\omega_{Sj}) \frac{\omega_{Sj}^2 \left|A_{ij}(\mathbf{k}_{Ii}, \mathbf{k}_{Sj})\right|^2}{V_{Ei}(\omega_{Ii}) \left|V_{Gj}(\omega_{Sj})\right|}$$

$$\times \left|\Gamma_0(k'_{Ii} + k'_{Sj})\right|^2 \times \frac{1}{k''_{Ii} + k''_{Sj}} . \tag{1.30}$$

For details see Eqs. (7.26) to (7.35) in this thesis.

3. Previous RBS Experiments

(1) Zincblende Structure

In 1977, Ulbrich and Weisbuch[13] employed a tunable near-infrared dye laser as an exciting source to study RBS at the 1s exciton formed by the Γ_6 conduction band and Γ_8 valence band in the III-V compound GaAs (zincblende cubic structure). Utilizing a [100] backscattering configuration and analyzing the scattered light with a grating spectrometer, they were able to observe the enhancement of the Brillouin intensity near resonance, the Brillouin shift dispersion, and the multiple Brillouin components resulting from the interbranch and intrabranch longitudinal acoustic (LA) phonon scattering between two exciton-polariton branches. A two-branch model was also used to explain the RBS experiments performed in the [110] direction where both transverse and longitudinal phonon scattering between polariton branches were observed, although the former (TA) is normally "forbidden" by deformation potential selection rules. Similar results, by the same group, were obtained from the RBS experiments performed on the II-VI compound CdTe.[14]

A three polariton branch model, however, was needed to explain the RBS data obtained from the semiconductor ZnSe. Sermage and Fishman,[15] also utilizing a tunable dye laser and a grating spectrometer, performed RBS experiments in both [100] and [110] backscattering configurations, the latter direction once again showing both TA and LA phonon components. For crystals of zincblende structure, the degenerate Γ_8 valence band results in two distinct exciton bands, each of which can couple with an incoming photon yielding overall a three exciton-polariton branch system. These two excitons are distinguishable via their effective translational masses, one exciton having a larger mass than the other. Both of these "light" and "heavy" excitons have been observed to participate in RBS in ZnSe. However, only the heavy exciton contributes to RBS in GaAs.

It should also be noted that only one-phonon scattering processes were observed in all the RBS data on cubic zincblende crystals.

(2) Wurtzite Structure

The crystal which has had its Raman and Brillouin components most extensively studied in the region of an exciton resonance is the II-VI semiconductor CdS. Even prior to the RBS prediction by BZB, Pine.[16] had investigated the Brillouin spectrum of CdS by temperature-tuning its 1s A-exciton towards a fixed frequency (6328 Å) laser. He observed a strong resonance enhancement in the LA Brillouin cross section as the frequency of this exciton was lowered (via increasing crystal temperature) towards the laser frequency. This temperature-tuning technique was also utilized by Bruce and Cummins.[17] who observed both resonant dispersion and enhancement of the LA Brilouin component as the A-exciton frequency was lowered towards the 4880 Å line of an argon laser. However, the two-branch features predicted by BZB could not be observed due to the severe broadening effects at the temperatures required to achieve resonance. Both of these studies used the Fabry-Perot interferometer to analyze the scattered light.

In 1977, Winterling and Koteles[18] utilized an experimental setup similar to the one used in the GaAs studies (dye laser and grating spectrometer) to perform RBS experiments from both 1s A- and B-exciton resonances in CdS. For the A-exciton, both LA and TA phonons were observed in the backscattering geometry with the incident laser wave vector $\mathbf{k}_I$ perpendicular to the hexagonal c-axis. Only intrabranch scattering involving the lower exciton-polariton branch (2-2') could be observed in these one-phonon scattering processes. Upper branch participation (1-1', 1-2', 2-1'), however, was witnessed in two-phonon scattering processes[19] which occured when the incident laser frequency was above the longitudinal exciton frequency. These two-phonon effects are possible due to the anisotropic and piezoelectric properties of CdS, the latter effect also being responsible for the observation of the "forbidden" TA phonon which was first observed in CdS.[20] The B-exciton was also investigated by this same group.[21] These RBS experiments proved to be extremely interesting since this exciton resonance was shown to exhibit either a two or three-branch behavior for the incident laser light polarized either parallel or perpendicular to the c-axis. The three-branch behavior results from terms in the B-exciton energy linear in wave vector which produce mixing among its ground states. As in the A-exciton case, both LA and TA one-phonon scattering were observed, although no two-phonon scattering processes were seen.

Yu and Evangelisti[22] have also carried out an investigation of RBS in CdS. They considered the role of the ABCs in determining the cross section, as proposed by BZB, and have suggested a new model for the CdS surface. Following Hopfield and Thomas, they introduced a surface "dead layer" with a large damping constant with which they were able to fit their cross section data reasonably well.

Broser and Rosenzweig[23] have performed RBS experiments in CdS with a high magnetic field perpendicular to the crystal c-axis. Due to the field-induced mixing and splitting of the allowed Γ_{5T} and forbidden Γ_6 states of the 1s A-exciton, a three-polariton-branch model was used to fit the Brillouin shift data. The Stokes LA 2-2' line at **H** = 0 was seen to split into three sub-lines with increasing magnetic field. For a fixed field, the Brillouin shifts of these three lines were theoretically fitted by considering interbranch and intrabranch LA phonon scattering between the two lower polariton branches only. These fits resulted in a determination of the singlet(Γ_{5T})-triplet(Γ_6) energy splitting. Corresponding splitting of the TA Stokes line could not be resolved in these experiments.

Recently, J. Wicksted et al[24] performed RBS experiments in the 1s A-exciton in CdS using a tunable dye laser and a triple-pass Fabry-Perot interferometer in series with a tandam double-grating spectrometer. With this high resolution setup, they have observed all the Brilouin components (1-1', 1-2', 2-1', 2-2', for both LA and TA phonon scattering) in one-phonon RBS processes for the first time. Their RBS intensity data favored ABC 2 formulated by Ting et al. But it was found that the intensity ratio between the Stokes LA 1-1' and

2-2' components was ~ 100 times smaller than BZB's prediction.

CdSe is another II-VI wurtzite semiconductor in which RBS has been investigated by Hermann and Yu.[25] In addition to observing LA and TA scattering as in the case of CdS, non-wave-vector-conserving scattering processes involving defects were also observed near the A-exciton in CdSe. No two-phonon scattering processes were observed, however. A two-branch model was used to fit the measured Brillouin shifts which resulted solely from the lower polariton branch scattering.

(3) Other Crystal Structures

RBS in the layered semiconductor HgI_2 near its A-exciton was investigated by Goto and Nishina.[26] This semiconductor, like CdS, is highly anisotropic with single LA phonon scattering being observed in the [001] direction while both LA and TA scattering processes were detected in the [201] direction. All Brillouin shift data were fitted using a two-branch model.

The 2p yellow exciton state in the cubic crystal Cu_2O has recently been investigated by So[27] using the RBS technique. This exciton state, however, is only weakly dipole-allowed and does not couple strongly to photons. Only the photon-like upper polariton branch was observed throughout the resonance region of this exciton state.

1.6. Properties of CdS

1. Primitive Unit Cell,[28] Group Symmetry and the Character Table[29]

As shown in Fig. 1.3, CdS has a hexagonal Bravais lattice. The basis (primitive unit cell) contains two cadmium ions located at (0, 0, 0) and (a/3, 2a/3, c/2) and two sulphur ions at (0, 0, u) and (a/3, 2a/3, c/2 + u), respectively.

The point group of CdS is C_{6v} ; all ions in the unit cell have C_{3v} site symmetry. The space group of the CdS crystal is C_{6v}^{4} which belongs to the wurtzite structure.

Each ion has four ions of the other kind as its nearest neighbours positioned at the corners of a tetrahedron. The conventional hexagonal axes ($\mathbf{a}_1$, $\mathbf{a}_2$, $\mathbf{a}_3$) have been used with the lattice parameters a = 4.16 Å , c = 6.75 Å , and u = 2.53 Å.

The symmetries of normal modes in the long wavelength limit, as well as the symmetries of electronic bands at the zone center, can be determined by neglecting translations and considering only the symmetry operations of the macroscopic point group C_{6v}.

The effects of electronic spin are described by the crystal double group, the character table of which is given in Table 1.1.

2. Normal Vibrational Modes and RBS Selection Rules[30]

Since a primitive unit cell contains four ions, there should be twelve normal vibrational modes in CdS. A group-theoretical analysis using Table 1.1 shows that those twelve modes at the Brillouin zone center have the symmetries $2\Gamma_1 + 2\Gamma_4 + 2\Gamma_5 + 2\Gamma_6$. One pair ($\Gamma_1 + \Gamma_5$) acounts for the three acoustic modes. The other Γ_1 is an infrared and Raman active optic mode, and the other Γ_5 is also an infrared and Raman active mode. The two doubly degenerate modes $2\Gamma_6$ are also Raman active and the $2\Gamma_4$ modes are both infrared and Raman inactive.

Using the macroscopic elasticity theory of Brillouin scattering, we may show that in the scattering geometry $x(y\ y)\bar{x}$ only the LA phonon (wave vector $\mathbf{q}$ // $\mathbf{x}$, ionic displacement vector $\mathbf{u}$ // x) will participate in Brillouin scattering events. However, in the case of RBS in CdS, one of the TA phonon modes ($\mathbf{q}$ // $\mathbf{x}$, $\mathbf{u}$ // z) can produce a longitudinal electric field due to the piezoelectric effect. Since the incident polaritons are strongly exciton-like near an exciton resonance, they can couple to this piezoelectrically induced longitudinal field via the Fröhlich interaction. Thus one of the TA phonon modes (q // **x**, **u** // z) will also contribute to RBS in the $x(y\ y)\bar{x}$ geometry in CdS.

3. Energy Bands

The band structure at $\mathbf{k} = 0$ in CdS[31] is given in Fig. 1.4 showing the symmetries of the s-like lowest conduction band (Γ_1) and the p-like highest valence bands (Γ_1 and Γ_5 , Γ_5 being higher in energy than Γ_1 due to the existence of crystal fields). In the presence of the spin-orbit coupling, the doubly degenerate Γ_5 valence band splits into Γ_9 and Γ_7 sub-bands with Γ_9 lying higher in energy than Γ_7 while the conduction and lower valence bands, both having Γ_1 symmetry, become Γ_7 . The Γ_7 conduction band and Γ_9 valence band are two-fold spin degenerate and have extrema at the center of the Brillouin zone. The two Γ_7 valence bands and the lowest Γ_7 conduction band have a k-linear term associated with their structure for $\mathbf{k} \perp \mathbf{c}$.

4. Exciton Series

An electron in the Γ_7 conduction band can combine with a hole from either the Γ_9 , upper Γ_7 , or lower Γ_7 valence bands forming the A, B, or C-exciton series respectively.

The 1s state of the A-exciton series has overall symmetries

$$\Gamma_1 \times \Gamma_9 \times \Gamma_7 = \Gamma_5 + \Gamma_6$$

where both the Γ_5 and Γ_6 excitons are two-fold degenerate at $\mathbf{k} = 0$. The Γ_5 level, which transforms like P_x and P_y (i.e. like x and y), is accessible by a dipole allowed transition[32] and has been observed as a strong absorption line[33] and a sharp reflectivity peak[34] when the incident light is polarized perpendicular to the c-axis ($E \perp \mathbf{c}$). The Γ_6 level is a pure triplet state (electron and hole spins are parallel) which has been observed in absorption experiments as a weak "forbidden" transition[33] when $\mathbf{E} // \mathbf{c}$.

The splitting of the Γ_5 and Γ_6 levels of the 1s A-exciton is primarily due to the electron-hole exchange Coulomb interaction.[35,36] The short-range (analytic) part of the exchange effect leads to the splitting of the dipole allowed Γ_5 state from the spin triplet Γ_6 state. There is also a long-range (non-analytic) exchange contribution which results in the longitudinal-transverse splitting of the Γ_5 state. The latter effect is dependent on the direction of the exciton wave vector **k**. For **k** // **c**, Γ_5 consists of two degenerate transverse modes; but for **k** $\perp$ **c**, Γ_5 has both longitudinal and transverse modes, as shown in Fig. 1.5.

The 1s states of the B- (and also C-) exciton series have symmetries

$$\Gamma_1 \times \Gamma_7 \times \Gamma_7 = \Gamma_1 + \Gamma_2 + \Gamma_5$$

where Γ_1 (transforming like z) and Γ_2 (pure spin triplet) are nondegenerate at **k** = 0. The 1s B-exciton state has been observed in reflectivity and absorption experiments as a dipole allowed transition for both **E** //**c** (due to the Γ_1 state) and **E** $\perp$ **c** (due to the Γ_5 state) polarizations.

The parameters of the 1s A- and B-excitons in CdS are given in Table 1.2 and Table 1.3 respectively.

Table 1.1. The Character Table and Basis Functions[29] for the Group C_{6v}

	Γ	E	$\bar{E}$	C_2 $\bar{C}_2$	$2C_3$	$2\bar{C}_3$	$2C_6$	$2\bar{C}_6$	$3\sigma_d$ $3\bar{\sigma}_d$	$3\sigma_v$ $3\bar{\sigma}_v$	Basis Functions
A_1	Γ_1	1	1	1	1	1	1	1	1	1	x^2+y^2, z^2 z
A_2	Γ_2	1	1	1	1	1	1	1	-1	-1	R_z
B_2	Γ_3	1	1	-1	1	1	-1	-1	1	-1	x^3-3xy^2
B_1	Γ_4	1	1	-1	1	1	-1	-1	-1	1	y^3-3yx^2
E_1	Γ_5	2	2	-2	-1	-1	1	1	0	0	(xz,yz) (x,y) (R_x,R_y)
E_2	Γ_6	2	2	2	-1	-1	-1	-1	0	0	x^2-y^2, xy
	Γ_7	2	-2	0	1	-1	$\sqrt{3}$	$-\sqrt{3}$	0	0	$\{\phi(1/2,-1/2),$ $\phi(1/2,1/2)\}$
	Γ_8	2	-2	0	1	-1	$-\sqrt{3}$	$\sqrt{3}$	0	0	$\Gamma_7 \times \Gamma_3$
	Γ_9	2	-2	0	2	2	0	0	0	0	$\{\phi(3/2,-3/2),$ $\phi(3/2,3/2)\}$

Remark: Basis function $\phi(j,m)$ means a function which transforms like an eigenstate of the angular momentum operators J^2 and J_z.

Table 1.2. Parameters
for the 1s A-Exciton in CdS at T = 4.2 K

Transverse Frequency[24]	$\tilde{\omega}_T$	$20588.8\ \mathrm{cm}^{-1}$
Oscillator Strength[24]	$4\pi\alpha_0$	0.0142
Background Dielectric Constant[24]	ε_b	9.38
Damping Constant	$\tilde{\gamma}$	$0.625\ \mathrm{cm}^{-1}$
Exciton Effective Mass[24]	$M_\perp$	$0.83\ m_0$
Exciton Effective Mass[36]	$M_{//}$	$2.7\ m_0$
Electron Effective Mass[34]	$m_{e\perp}$	$0.2\ m_0$
Electron Effective Mass[33]	$m_{e//}$	$0.198\ m_0$
Hole Effective Mass[37]	$m^A_{h\perp}$	$0.7\ m_0$
L-T Splitting[37]	$\tilde{\Delta}_{LT}$	$15.4\ \mathrm{cm}^{-1}$
Singlet-Triplet Splitting[23]	$\tilde{\Delta}_{st}$	$1.6\ \mathrm{cm}^{-1}$
k-Linear Coefficient of Electron[38]	C_e	1.6×10^{-10} eV cm
k-Linear Coefficient of Hole[39]	C_{hA}	0
k-Linear Coefficient of Exciton[39]	ϕ_A	1.9×10^{-11} eV cm
Binding Energy[33]	B	0.0298 eV
Bohr Radius[33]	a	28 Å
Electron Effective g-value[23]	$g_{e\perp}$	1.75
Electron Effective g-value[40]	$g_{e//}$	1.79
Hole Effective g-value[40]	$g_{h\perp}$	0
Hole Effective g-value[40]	$g_{h//}$	1.23
Diamagnetic Shift[40]	$\delta_\perp$	1.9×10^{-14} eV/Gauss^2
Diamagnetic Shift[40]	$\delta_{//}$	2.2×10^{-14} eV/Gauss^2

Table 1.3. Parameters
for the 1s B-Exciton in CdS at T = 4.2 K

Transverse Frequency[41]	$\tilde{\omega}_{TB}$	20711.3 cm^{-1}
Oscillator Strength[30]	$4\pi\alpha_{o_B}$	0.01
Background Dielectric Constant[41]	ε_{bB}	8.9
Damping Constant[42]	$\tilde{\gamma}_B$	0.605 cm^{-1}
Effective Mass[41]	$M_{\perp B}$	1.2 m_0 (if E $\perp$ c)
		1.5 m_0 (if E // c)
L-T Splitting[41]	$\tilde{\Delta}_{LTB}$	7.7 cm^{-1}
K-Linear Coeffilient of Electron[38]	C_e	1.6×10^{-10} eV·cm
K-Linear Coefficient of Hole[21]	C_{hB}	-6.7×10^{-10} eV·cm
K-Linear Coefficient of Exciton[21]	ϕ_B	5.6×10^{-10} eV·cm
Binding Energy[34]	B_B	0.028 eV
Bohr Radius[34]	a_B	28 Å

Table 1.4. Parameters Used in the Expressions for Polariton-Phonon Interaction Kernels

Sound Velocity[43]	c_{LA}	4.25×10^5 cm/sec
Sound Velocity[43]	c_{TA}	1.76×10^5 cm/sec
Crystal Density[43]	ρ	4.84 gm/cm^3
Piezoelectric Constant[44]	e_{15}	-0.21 Coulomb/m^2
Deformation Potential[45]	D_e	4.5 eV
Deformation Potential[45]	D_h	-2.9eV

References

1. W. Brenig, R. Zeyher and J. L. Birman, Phys. Rev. B**6**, 4617 (1972).

2. R. J. Elliot, in: Polaritons and Excitons edited by C. G. Kuper and G. D. Whitfield (Plenum Press, New York, 1963) p.269.

3. P. Y. Yu, Study of Excitons and Exciton-Phonon Interactions by Resonant Raman and Brillouin Spectroscopies in: Excitons, Topics in Current Physics 14, edited by K. Cho (Springer-Verlag, Berlin, Heidelberg, New York, 1979) p.231 and B. Bendow, J. L. Birman: Phys. Rev. B1, 1678 (1970).

4. R. S. Knox, Theory of Excitons in Solid State Physics Supplyment 5 (Academic Press, New York and London, 1963) p.133.

5. S. I. Pekar, Sov. Phys. JETP3**4**, 813 (1958); S. I. Pekar, Sov. Phys. JETP**6**, 785 (1958).

6. C. S. Ting, M. Frankel and J. L. Birman, Solid State Commun. **17**, 1285 (1975).

7. J. L. Birman and J. J. Sein, Phys. Rev. B**6**, 2482 (1972); J. J. Sein, Phys. Letters **32A**, 141 (1970).

8. A. A. Maradudin and D. L. Mills, Phys. Rev. B**7**, 2787 (1973).

9. G. S. Agarwal, D. N. Pattanyak and E. Wolf, Phys. Rev. Lett. **27**, 1022 (1971); Phys. Rev. B**8**, 4768 (1973).

10. R. Zeyher, J. L. Birman, and W. Brenig, Phys. Rev. B**6**, 4613 (1972).

11. M. Matsushita, J. Wicksted and H. Z. Cummins, Phys. Rev. B**29**, 3362 (1984).

12. J. R. Sandercock, Phys. Rev. Lett. **29**, 1735 (1972).

13. R. G. Ulbrich and C. Weisbuch, Phys. Rev. Lett. **38**, 865 (1977).

14. R. G. Ulbrich and C. Weisbuch, Festkorperprobleme XVIII - Advances in Solid State Physics edited by J. Treusch, Braunschweig: Vieweg, (1978) p.217.

15. B. Sermage and G. Fishman, Phys. Rev. Lett. **43**, 1043 (1979); Phys. Rev. B**23**, 5107 (1981).

16. A. S. Pine, Phys. Rev. B**5**, 3003 (1972).

17. R. H. Bruce and H. Z. Cummins, Phys. Rev. B1**6**, 4462 (1977).

18. G. Winterling and E. S. Koteles, Solid State Commun. **23**, 95 (1977).

19. P. Y. Yu and F. Evangelisti, Solid State Commun. **27**, 87 (1978).

20. G. Winterling and E. S. Koteles and M. Cardona, Phys. Rev. Lett. **39**, 1286 (1977).

21. E. S. Koteles and G. Winterling, Phys. Rev. Lett. **44**, 948 (1980).

22. P. Y. Yu and F. Evangelisti, Phys. Rev. Lett. **42**, 1642 (1979).

23. I. Broser and M. Rosenzweig, Solid State Commun. **36**, 1027 (1980).

24. J. Wicksted, M. Matsushita, H. Z. Cummins, T. Shigenari and X. Z. Lu, Phys. Rev. B**29**, 3350 (1984).

25. C. Hermann and P. Y. Yu, Solid State Commun. **28**, 313 (1978); Phys. Rev. B**21**, 3675 (1980).

26. T. Goto and T. Nishina, Solid State Commun. **31**, 751 (1979).

27. C. Y. So, Ph.D. Thesis, University of Toronto, Toronto, 1981, unpublished.

28. R. W. Wyckoff, Crystal Structures (Interscience, New York, 1960) vol.1, p.111.

29. G. F. Koster, J. O. Dimmock, R. G. Wheeler and H. Statz, Properties of the Thirty-Two Point Groups (M.I.T. Press, Cambridge, 1963) p.67.

30. J. Wicksted, Ph.D. Thesis, The City College of New York, New York, 1983, unpublished, p18.

31. J. L. Birman, Phys. Rev. **114**, 1490 (1959).

32. R. J. Elliot, Phys. Rev. **108**, 1384 (1957).

33. J. J. Hopfield and D. G. Thomas, Phys. Rev. **122**, 35 (1961).

34. D. G. Thomas and J. J. Hopfield, Phys. Rev. **116**, 573 (1959).

35. K. Cho, Phys. Rev. B**14**, 4463 (1976).

36. K. Cho, in: Excitons edited by K. Cho (Springer-Verlag, New vork, 1979).

37. G. Winterling and E. S. Koteles, in: Lattice Dynamics edited by M. Balkanski (Flammarion Sciences, Paris, 1978) p.170.

38. R. Romestain, S. Geschwind, and G. E. Devlin, Phys. Rev. Lett. **39**, 1583 (1977).

39. T. Shigenari, X. Z. Lu, and H. Z. Cummins, Phys. Rev. B**30**, 1962 (1984).

40. H. Vanhaus, S. Suga, and K. Cho, Phys. Rev. B**16**, 4419 (1977).

41. See the review article by P. Y. Yu, in: Light Scattering in Solids, edited by J. L. Birman, H. Z. Cummins and K. K. Rebane (Plenum Press, New York, 1979).

42. G. D. Mahan and J. J. Hopfield, Phys. Rev. **135**, A428 (1964).

43. D. Gerlich, J. Phys. Chem. Solids, 28, 2575 (1967).

44. A. R. Huston, J. Appl. Phys. Suppl. 32, 2287 (1961).

45. D. W. Langer, R. N. Euwena, K. Era and T. Koda, Phys. Rev. B2, 4005 (1970).

Chapter 2. Multicomponent Exciton-Polariton Dispersion

In this chapter, we will give a general method for calculating exciton states and multicomponent exciton-polariton dispersion in the presence of any type of perturbation.

2.1. Effective Hamiltonian Theory

Effective Hamiltonian Theory[1,2] is a general group-theoretical method used to calculate exciton levels in the presence of any type of perturbation. From group-theoretical analysis one can find out the most general form of Hamiltonian allowed by the symmetry of a crystal in terms of representative variables for all the possible perturbations on a set of unperturbed exciton states. For any particular perturbations, one may simply ascribe them to their corresponding representative variables and write out the effective Hamiltonian matrix directly, and then obtain the perturbed exciton states by diagonalizing that matrix.

In the following, we will consider only the ground state (1s) excitons formed from an s-like conduction band and a p-like valence band at the Γ-point ($\mathbf{k} = 0$) in a wurtzite crystal.

1. Exciton Basis Functions

(1) Conduction Electron Eigenstates

Since the conduction band is s-like, the orbital wavefunction of the conduction electron is totally symmetric and transforms like Γ_1, the conduction electron eigenstates are characterized by their spin states only. We denote them as α_e and β_e for spin-up and spin-down states, respectively.

(2) Valence Electron Eigenstates

The p-like valence electron spin states are denoted by α and β for spin-up and spin-down states, respectively. The orbital states are

$$\begin{aligned} |1\rangle &= -2^{-1/2}(x + iy) \\ |0\rangle &= z \\ |-1\rangle &= 2^{-1/2}(x - iy) \; . \end{aligned} \tag{2.1}$$

Thus the valence electron states may take the following 6 combinations: $|1\rangle\alpha$, $|1\rangle\beta$; $|0\rangle\alpha$, $|0\rangle\beta$; $|-1\rangle\alpha$, $|-1\rangle\beta$. The valence electron eigenstates may be obtained by diagonalizing the spin-orbit interaction and anisotropic crystal field:

$$\begin{aligned} \Gamma_7(B): &\qquad \phi_1 = \delta|0\rangle\alpha - \gamma|1\rangle\beta \\ &\qquad \phi_2 = \gamma|-1\rangle\alpha - \delta|0\rangle\beta \\ \Gamma_7(C): &\qquad \phi_3 = -\gamma|0\rangle\alpha - \delta|1\rangle\beta \\ &\qquad \phi_4 = \delta|-1\rangle\alpha + \gamma|0\rangle\beta \\ \Gamma_9(A): &\qquad \phi_5 = -|1\rangle\alpha \\ &\qquad \phi_6 = |-1\rangle\beta \; , \end{aligned} \tag{2.2}$$

where

$$\gamma = [2/(2 + B_0^2)]^{1/2}$$

$$\delta = B_0(2 + B_0^2)^{-1/2} \qquad (2.3)$$

$$B_0 = -2 + 3\Delta_1/\Delta_{SO} \ ,$$

and Δ_1 is the energy difference between $\Gamma_9(A)$ and $\Gamma_7(B)$ valence bands, while Δ_{SO} is the spin-orbit splitting of the valence band in the virtual cubic limit. The band structure at **k** = 0 and the relevant parameters in CdS are shown in Fig. 1.4.

(3) Electron-Hole Pair States

Electron-hole pair states could be obtained by combining conduction electron and valence hole states and antisymmetrizing them:

$$\Phi_1 = |\alpha_e(\phi_5)|,\ \Phi_2 = |\alpha_e(\phi_6)|,\ \Phi_3 = |\beta_e(\phi_5)|,\ \Phi_4 = |\beta_e(\phi_6)|$$

$$\Psi_1 = |\alpha_e(\phi_1)|,\ \Psi_2 = |\alpha_e(\phi_2)|,\ \Psi_5 = |\beta_e(\phi_1)|,\ \Psi_6 = |\beta_e(\phi_2)| \qquad (2.4)$$

$$\Psi_3 = |\alpha_e(\phi_3)|,\ \Psi_4 = |\alpha_e(\phi_4)|,\ \Psi_7 = |\beta_e(\phi_3)|,\ \Psi_8 = |\beta_e(\phi_4)|,$$

where $|\alpha_e(\phi_5)|$ represents the normalized Slater determinant for the multielectron state in which the valence state ϕ_5 is missing and the conduction state α_e is occupied.

(4) Exciton Eigenstates

For ground state (1s) excitons with **k** = 0, we may approximately take the electron-hole pair wavefunctions as the exciton wavefunctions. However, in order to characterize the polarization behavior of excitons, we choose the following combinations as our exciton basis functions:

$\Gamma_5(A)$: $\quad |x)_A = 2^{-1/2}\,(\Phi_1 + \Phi_4) \qquad (3^{1/2})$

$\qquad\qquad |y)_A = i2^{-1/2}\,(\Phi_1 - \Phi_4) \qquad (3^{1/2})$

$\Gamma_6(A)$: $\quad |t')_A = 2^{-1/2}\,(\Phi_3 - \Phi_2) \qquad (0)$

$\qquad\qquad |t)_A = -i2^{-1/2}\,(\Phi_3 + \Phi_2) \qquad (0)$

$$
\begin{array}{llll}
\Gamma_5(B): & |x)_B = 2^{-1/2}\,(\Psi_5 + \Psi_2) & (3^{1/2}\gamma) & \\
 & |y)_B = i2^{-1/2}\,(\Psi_5 - \Psi_2) & (3^{1/2}\gamma) & \\
\Gamma_1(B): & |z)_B = 2^{-1/2}\,(\Psi_1 - \Psi_6) & (6^{1/2}\delta) & (2.5) \\
\Gamma_2(B): & |t)_B = -i2^{-1/2}\,(\Psi_1 + \Psi_6) & (0) & \\
\Gamma_5(C): & |x)_C = 2^{-1/2}\,(\Psi_7 + \Psi_4) & (3^{1/2}\delta) & \\
 & |y)_C = i2^{-1/2}\,(\Psi_7 - \Psi_4) & (3^{1/2}\delta) & \\
\Gamma_1(C): & |z)_C = 2^{-1/2}\,(\Psi_8 - \Psi_3) & (6^{1/2}\gamma) & \\
\Gamma_2(C): & |t)_C = i2^{-1/2}\,(\Psi_8 + \Psi_3) & (0) &
\end{array}
$$

where $|x)$, $|y)$, and $|z)$ represent the states polarized along x, y, and z directions, respectively, i.e. the states optically active for light polarized in those directions. $|t)$ represents the pure spin triplet state which is optically inactive. The numbers in parentheses represent the relative magnitudes of the transition dipole moments of the exciton states, and γ and δ are defined in Eq. (2.3).

2. Effective Hamiltonian on the Exciton Basis

The total effective Hamiltonian in the presence of perturbations can be separated into three parts, i.e. conduction band contribution, valence band contribution and electron-hole exchange interaction:

$$H(\vec{\sigma}_e, \vec{\sigma}, l, \Xi) = H^{(c)}(\vec{\sigma}_e, \Xi) + H^{(v)}(\vec{\sigma}, l, \Xi) + H_{ex}(\vec{\sigma}_e, \vec{\sigma}) \qquad (2.6)$$

where $\vec{\sigma}_e$ ($\vec{\sigma}$) is the conduction electron (valence hole) spin operator, **l** is the orbital angular momentum operator of the valence hole, Ξ are the representative variables of the perturbation. Since we neglected the electron-hole exchange interaction in deriving the hydrogen-like exciton states, the electron-hole exchange interaction will appear as a perturbation to the unperturbed exciton basis. For convenience we ignore l and Ξ-dependences of the exchange interactions and separate $H^{(c)}$ and $H^{(v)}$ into time-reversal-symmetric and antisymmetric parts.

We define the components of Ξ according to their symmetry properties:

Γ_1:	S	[z]
Γ_2:	T	[l_z]
Γ_3:	V	[$(3y^2-x^2)x$]
Γ_4:	U	[$(3x^2-y^2)y$]
Γ_5:	(X,Y)	[x,y]
Γ_6:	(W,Z)	[x^2-y^2, 2xy] ,

where the third column gives transformation properties of each type of Ξ. Some simple perturbation examples for those components are given in Table 2.1 in which E represents electric field, B is magnetic field, K is exciton wave vector, and ε is strain tensor. Product perturbations of Ξ = (S, T, V, U, X, Y, W, Z) and Ξ' = (S',T',V',U',X',Y',W',Z') are given in Table 2.2. Based on the above exciton basis functions and the definitions of representative variables, we obtain the matrix representations of effective Hamiltonians in the presence of perturbations as follows (We restrict ourselves to the A, and B-excitons in CdS):

(1) Exchange Interaction Matrix Representation

The exchange interaction only exists in the dipole allowed exciton states whose matrix representation is given in Table 2.3 where

$$j(u) = j_0 + j_1(3u^2 - 1) \tag{2.7}$$

and j_0 is the short-range exchange interaction parameter, j_1 is the long-range exchange interaction parameter, (ξ, η, ζ) are the direction cosines of the exciton wave vector **k** with respect to x, y, z-axes, and γ, δ are defined in Eq. (2.3).

(2) Matrix Representation for the Bloch Band Contributions to the Effective Hamiltonian

These matrix representations are given in Tables 2.4 and 2.5. In Table 2.5, the complete matrix should be obtained by adding complex conjugate of all the elements to their opposite corners.

3. Recipe: How to Find the Matrix Representation of the Effective Hamiltonian of the 1s Excitons in the Presence of Perturbation in C_{6v} Structure.

(1) Unperturbed Hamiltonian $H_0^{(0)}$:

The matrix representation of the unperturbed effective Hamiltonian can be obtained by setting S = 1, T = V = U = X = Y = W = Z = 0 in $H_S^{(c)} + H_S^{(v)}$ (Table 2.4):

$$H_0^{(0)} = \begin{pmatrix} \alpha_2 & 0 & 0 & 0 & 0 & 0 & 0 & 0 \\ 0 & \alpha_2 & 0 & 0 & 0 & 0 & 0 & 0 \\ 0 & 0 & \alpha_2 & 0 & 0 & 0 & 0 & 0 \\ 0 & 0 & 0 & \alpha_2 & 0 & 0 & 0 & 0 \\ 0 & 0 & 0 & 0 & \alpha_1 & 0 & 0 & 0 \\ 0 & 0 & 0 & 0 & 0 & \alpha_1 & 0 & 0 \\ 0 & 0 & 0 & 0 & 0 & 0 & \alpha_1 & 0 \\ 0 & 0 & 0 & 0 & 0 & 0 & 0 & \alpha_1 \end{pmatrix}$$

We define $\Delta_1 = \alpha_1 - \alpha_2$, then

$$H_0^{(0)} = \left(\begin{array}{cccccccc} 0 & 0 & 0 & 0 & 0 & 0 & 0 & 0 \\ 0 & 0 & 0 & 0 & 0 & 0 & 0 & 0 \\ 0 & 0 & 0 & 0 & 0 & 0 & 0 & 0 \\ 0 & 0 & 0 & 0 & 0 & 0 & 0 & 0 \\ 0 & 0 & 0 & 0 & \Delta_1 & 0 & 0 & 0 \\ 0 & 0 & 0 & 0 & 0 & \Delta_1 & 0 & 0 \\ 0 & 0 & 0 & 0 & 0 & 0 & \Delta_1 & 0 \\ 0 & 0 & 0 & 0 & 0 & 0 & 0 & \Delta_1 \end{array}\right) \begin{array}{l} |x)_A \\ |y)_A \\ |t')_A \\ |t)_A \\ |x)_B \\ |y)_B \\ |z)_B \\ |t)_B \end{array} \qquad (2.8)$$

(2) Exchange Hamiltonian H_{ex}:

Suppose we consider excitons with **k** = (k,0,0), thus

$$\xi = 1, \quad j(\xi) = j_0 + 2j_1$$

$$\eta = \zeta = 0, \quad j(\eta) = j(\zeta) = j_0 - j_1$$

and we obtain from Table 2.3:

$$H_{ex} = \left(\begin{array}{ccccc} J_L & J_L\gamma & 0 & 0 & 0 \\ J_L\gamma & J_L\gamma^2 & 0 & 0 & 0 \\ 0 & 0 & J & J\gamma & 0 \\ 0 & 0 & J\gamma & J\gamma^2 & 0 \\ 0 & 0 & 0 & 0 & J\delta^2 \end{array}\right) \begin{array}{l} |x)_A \\ |x)_B \\ |y)_A \\ |y)_B \\ |z)_B \end{array} \qquad (2.9)$$

where $J_L = 3(j_0 + 2j_1)$, $J = 3(j_0 - j_1)$.

(3) Other Perturbation Hamiltonian

We consider the k-linear term in finite k effects for **k** = (k,0,0). From Table 2.1 we find the representative variable for k_x is X and is antisymmetric, so we pick up only the terms containing X in $H_{as}^{(c)}$ +

$H_{as}^{(v)}$ (Table 2.5) and write out:

$$H_{KL}=\left(\begin{array}{cccccccc|l}
0 & 0 & i\bar{\mu}K & 0 & 0 & 0 & i\bar{\varepsilon}_1 K & 0 & |x)_A \\
 & 0 & 0 & -i\bar{\mu}k & 0 & 0 & 0 & -i\bar{\varepsilon}_1 K & |y)_A \\
 & & 0 & 0 & i\bar{\varepsilon}_1 K & 0 & 0 & 0 & |t')_A \\
 & & & 0 & 0 & -i\bar{\varepsilon}_1 K & 0 & 0 & |t)_A \\
 & & & & 0 & 0 & -i(\bar{\varepsilon}_3+\bar{\mu})K & 0 & |x)_B \\
 & & \text{H.C.} & & & 0 & 0 & -i(\bar{\varepsilon}_3-\bar{\mu})K & |y)_B \\
 & & & & & & 0 & 0 & |z)_B \\
 & & & & & & & 0 & |t)_B
\end{array}\right) \quad (2.10)$$

(4) The total Effective Hamiltonian H_0

If we restrict ourselves to the A and B-exciton subspace, we obtain the matrix representation of the total effective Hamiltonian

$$H_0 = H_0^{(0)} + H_{ex} + H_{KL} \qquad (2.11)$$

$$=\left(\begin{array}{cccccccc|l}
J_L & 0 & i\bar{\mu}K & 0 & \gamma J_L & 0 & i\bar{\varepsilon}_1 K & 0 & |x)_A \\
 & J & 0 & -i\bar{\mu}K & 0 & \gamma J & 0 & -i\bar{\varepsilon}_1 K & |y)_A \\
 & & 0 & 0 & i\bar{\varepsilon}_1 K & 0 & 0 & 0 & |t')_A \\
 & & & 0 & 0 & -i\bar{\varepsilon}_1 K & 0 & 0 & |t)_A \\
 & & & & \gamma^2 J_L+\Delta_1 & 0 & -i(\bar{\varepsilon}_3+\bar{\mu})K & 0 & |x)_B \\
 & & & & & \gamma^2 J+\Delta_1 & 0 & -i(\bar{\varepsilon}_3-\bar{\mu})K & |y)_B \\
 & & & \text{H.C.} & & & 2\delta^2 J+\Delta_1 & 0 & |z)_B \\
 & & & & & & & \Delta_1 & |t)_B
\end{array}\right)$$

Exciton state mixing and level splitting in the presence of perturbation (symmetry breaking effect) can be obtained by diagonalizing H_0.

2.2. Eigenvalue Method[3]

Suppose there is a set of unperturbed exciton states of energies $\omega_j + \hbar k^2/(2M_j)$ and oscillator strengths $4\pi\alpha_j$ $(j = 1,2,\cdots,s)$ in a narrow energy region. They interact with each other via some perturbations and also couple to the photon fields. As a result, there will be 2s+2 polariton components. In principle one can calculate the polariton dispersion $k(\omega)$ by diagonalizing the exciton Hamiltonian to obtain the perturbed exciton states of energies $\omega'_j + \hbar k^2/(2M_j)$ and oscillator strengths $4\pi\alpha'_j$ and solving the polariton dispersion equation

$$\frac{c^2k^2}{\omega^2} = \varepsilon_b + \sum_{j=1}^{s} \frac{4\pi\alpha'_j\omega'^2_j}{\omega'^2_j - \omega^2 + \dfrac{\hbar\omega'_j}{M_j} k^2 - i\omega\gamma_j} .$$

However, due to the mathematical difficulties in solving the above complex polynomial equation, we need to find some more practical method. The eigenvalue method reduces the problem from solutions of a high order polynomial to eigenvalues of a matrix which can be easily solved by computer programs.

1. Derivation

Assume that there are s unperturbed exciton states of energies $\omega_j + \hbar k^2/(2M_j)$ and oscillator strengths $4\pi\alpha_j$; the interactions between them are specified by a matrix $h_{ij}(\mathbf{k})$ which could be found by using the effective Hamiltonian method as described above. We define

$$\nu_j = \langle 0|\ e(\mathbf{r}_h - \mathbf{r}_e)\ |j\rangle\cdot\mathbf{e}\ , \tag{2.12}$$

where **e** is the polarization unit vector of a photon. One can relate ν_j to α_j by:

$$\nu_j = (\alpha_j\hbar\omega_j/2)^{1/2}\ . \tag{2.13}$$

The exciton Hamiltonian in the second quantized form is

$$H_0 = \sum_{i,j=1}^{s} h_{ij}(\mathbf{k})b_i^\dagger b_j \tag{2.14}$$

where $b_i^\dagger$ (b_j) is the creation (annhilation) operator of an exciton in j'th unperturbed exciton state at **k** = 0. We treat photons classically, thus the electric field is written:

$$\mathbf{E} = \mathbf{e}\ E_0\ (e^{-i\omega t} + e^{i\omega t})\ . \tag{2.15}$$

The exciton-photon interaction Hamiltonian is

$$H' = -\ E_0 \sum_{j=1}^{s} (\nu_j b_j e^{-i\omega t} + \nu_j^* b_j^\dagger e^{i\omega t})\ . \tag{2.16}$$

The total Hamiltonian of the exciton-photon system will be

$$H = H_0 + H'\ . \tag{2.17}$$

Using the Heisenberg equation of motion for $b_j^\dagger$ and b_j one obtains

$$\sum_{i=1}^{s} (\mathbf{h} - \hbar\omega\ \mathbf{1})_{ji}\ b_i^\dagger = \nu_j E_0 \tag{2.18}$$

$$\sum_{i=1}^{s} (\mathbf{h}^\tau + \hbar\omega\ \mathbf{1})_{ji}\ b_i = \nu_j^* E_0 \tag{2.19}$$

where $\mathbf{h}^\tau$ is the transposed **h**, and **1** is the unit matrix. On the other hand, $P_{ex} = \chi_{ex}E_0$, thus

$$\sum_{j=1}^{S} (\nu_j b_j + \nu_j^* b_j^\dagger) = \frac{n^2 - \varepsilon_b}{4\pi} E_0 , \qquad (2.20)$$

where

$$n = \frac{ck}{\omega} .$$

Combining Eqs. (2.18), (2.19) and (2.20) one obtains

$$\left(\begin{array}{ccccccc}
h_{11}-\hbar\omega & \cdots & h_{1S} & & & & \nu_1 \\
\vdots & & \vdots & & & & \vdots \\
h_{S1} & \cdots & h_{SS}-\hbar\omega & & & & \nu_S \\
 & & & h_{11}+\hbar\omega & \cdots & h_{S1} & \nu_1^* \\
 & & & \vdots & & \vdots & \vdots \\
 & & & h_{1S} & \cdots & h_{SS}+\hbar\omega & \nu_S^* \\
\nu_1^* & \cdots & \nu_S^* & \nu_1 & \cdots & \nu_S & (c^2k^2/\omega^2 - \varepsilon_b)/(4\pi)
\end{array}\right)
\left(\begin{array}{c} b_1^\dagger \\ \vdots \\ b_S^\dagger \\ b_1 \\ \vdots \\ b_S \\ -E_0 \end{array}\right) = 0 .$$

(2.21)

If we approximate

$$\mathbf{h}^\tau + \hbar\omega\,\mathbf{1} \approx 2\hbar\bar{\omega}\,\mathbf{1} ,$$

and define

$$\varepsilon_b' = \varepsilon_b + 2\pi \sum_{j=1}^{S} \frac{|\nu_j|^2}{\hbar\bar{\omega}} , \qquad (2.22)$$

Eq. (2.21) is simplified as

$$\left(\begin{array}{ccc|c}
 & & & \nu_1 \\
 & h_{ij}(\mathbf{k})-\hbar\omega\delta_{ij} & & \vdots \\
 & & & \nu_S \\
\nu_1^* & \cdots & \nu_S^* & (c^2k^2/\omega^2 - \varepsilon_b')/(4\pi)
\end{array}\right)
\left(\begin{array}{c} b_1^\dagger \\ \vdots \\ b_S^\dagger \\ -E_0 \end{array}\right) = 0 . \qquad (2.23)$$

Letting

$$h_{ij}(\mathbf{k}) = H_{ij} + L_{ij}k + J_{ij}k^2 \tag{2.24}$$

one obtains

$$(S + Tk + Uk^2)X = 0 \ ,$$

where

$$S = \left[\begin{array}{ccc} & & \nu_1 \\ & H_{ij}-\hbar\omega\delta_{ij} & \vdots \\ & & \nu_S \\ \nu_1^* & \cdots\cdots \quad \nu_S^* & -\varepsilon_b'/(4\pi) \end{array} \right] \tag{2.25}$$

$$T = \left[\begin{array}{ccc} & & 0 \\ & L_{ij} & \vdots \\ & & 0 \\ 0 & \cdots\cdots\cdots\cdots \quad 0 & 0 \end{array} \right] \tag{2.26}$$

$$U = \left[\begin{array}{ccc} & & 0 \\ & J_{ij} & \vdots \\ & & 0 \\ 0 & \cdots\cdots\cdots\cdots \quad 0 & c^2/(4\pi\omega^2) \end{array} \right] \tag{2.27}$$

$$X = \left[\begin{array}{c} b_1^\dagger \\ \vdots \\ b_S^\dagger \\ -E_0 \end{array} \right] \tag{2.28}$$

Defining

$$kX = Y \ , \tag{2.29}$$

We obtain

$$SX + TY + UkY = 0$$

i.e.

$$U^{-1}SX + U^{-1}TY + kY = 0 \; . \qquad (2.30)$$

Combining Eqs. (2.29) and (2.30) we obtain

$$\begin{bmatrix} U^{-1}T+k & U^{-1}S \\ \\ -1 & k \end{bmatrix} \begin{bmatrix} Y \\ \\ X \end{bmatrix} = 0 \; ,$$

namely

$$\left[\begin{array}{ccccccc} & & & & & & \\ & U^{-1}T + k & & & U^{-1}S & & \\ & & & & & & \\ -1 & & & k & & & \\ & \ddots & & & \ddots & & \\ & & \ddots & & & \ddots & \\ & & -1 & & & & k \end{array}\right] \begin{bmatrix} kb_1^\dagger \\ \vdots \\ kb_s^\dagger \\ -kE_0 \\ b_1^\dagger \\ \vdots \\ b_s^\dagger \\ -E_0 \end{bmatrix} = 0 \; .$$

$$. \qquad (2.31)$$

The polariton dispersion relation could be obtained by setting the determinant in Eq. (2.31) equal to zero, i.e., $k(\omega)$ is the negative of the eigenvalue of the matrix

$$A = \begin{bmatrix} & U^{-1}T & & U^{-1}S & \\ & & & & \\ -1 & & 0 & & \\ & \ddots & & \ddots & \\ & & -1 & & 0 \end{bmatrix}. \tag{2.32}$$

Obviously, the dimension of matrix A is $(2s+2)\mathrm{x}(2s+2)$ which gives $2s+2$ k's for each ω.

2. Recipe: How to Find the Polariton Dispersion $k(\omega)$ for Each Real ω in the Presence of Several Interacting Exciton States.

(1) Write out the effective Hamiltonian matrix of excitons.

Suppose we consider the k-linear interaction in the A-exciton of CdS with $\mathbf{k} = (k,0,0)$. According to Eq. (2.11), the effective Hamiltonian of excitons is

$$H_o = \begin{array}{c} \\ \\ \end{array}\!\!\begin{array}{cccc} |x)_A & |y)_A & |t')_A & |t)_A \end{array}$$

$$H_o = \begin{pmatrix} J_L & 0 & i\bar{\mu}k & 0 \\ 0 & J & 0 & -i\bar{\mu}k \\ -i\bar{\mu}k & 0 & 0 & 0 \\ 0 & i\bar{\mu}k & 0 & 0 \end{pmatrix} + C \, .$$

Defining

$$C = \omega_o + \frac{\hbar k^2}{2M} - \frac{i\gamma}{2} - \Delta_{st}$$

$$J = \Delta_{st}$$

$$J_L = \Delta_{LT} + \Delta_{st}$$

$$\bar{\mu} = e$$

we obtain $H_0 = [h_{ij}(\mathbf{k})]$ as follows

$$H_0 = \hbar \begin{array}{c} \\ \\ \\ \\ \\ \end{array} \begin{array}{cccc} |x)_A & |t')_A & |y)_A & |t)_A \\ \left(\begin{array}{c} \omega_0+\Delta_{LT}+\frac{\hbar k^2}{2M}-\frac{i\gamma}{2} \\ -iek \\ 0 \\ 0 \end{array}\right. & \begin{array}{c} iek \\ \omega_0-\Delta_{st}+\frac{\hbar k^2}{2M}-\frac{i\gamma}{2} \\ 0 \\ 0 \end{array} & \begin{array}{c} 0 \\ 0 \\ \omega_0+\frac{\hbar k^2}{2M}-\frac{i\gamma}{2} \\ iek \end{array} & \left.\begin{array}{c} 0 \\ 0 \\ -iek \\ \omega_0-\Delta_{st}+\frac{\hbar k^2}{2M}-\frac{i\gamma}{2} \end{array}\right) \end{array} . \tag{2.33}$$

Since $|y)_A$ is the only optically active exciton state and $|t)_A$ is the only state which mixes with $|y)_A$ under the considered perturbation, we can restrict ourselves to the subspace $|y)_A$ and $|t)_A$.

(2) Construct matrices S, T, and U according to Eqs. (2.24) to (2.27):

$$S = \begin{pmatrix} \hbar(\omega_0-i\gamma/2-\omega) & 0 & (\alpha_0\hbar\omega_0/2)^{1/2} \\ 0 & \hbar(\omega_0-\Delta_{st}-i\gamma/2-\omega) & 0 \\ (\alpha_0\hbar\omega_0/2)^{1/2} & 0 & -\varepsilon_b'/(4\pi) \end{pmatrix} \tag{2.34}$$

$$T = \begin{pmatrix} 0 & -ie\hbar k & 0 \\ ie\hbar k & 0 & 0 \\ 0 & 0 & 0 \end{pmatrix} \tag{2.35}$$

$$U = \begin{pmatrix} \frac{\hbar^2}{2M} & 0 & 0 \\ 0 & \frac{\hbar^2}{2M} & 0 \\ 0 & 0 & \frac{c^2}{4\pi\omega^2} \end{pmatrix}, \tag{2.36}$$

and

$$U^{-1} = \begin{bmatrix} \frac{2M}{\hbar^2} & 0 & 0 \\ 0 & \frac{2M}{\hbar^2} & 0 \\ 0 & 0 & \frac{4\pi\omega^2}{c^2} \end{bmatrix} . \qquad (2.37)$$

(3) Construct matrix A according to Eq. (2.32), and calculate the eigenvalues for $k(\omega)$ of the matrix A for each given ω. The negatives of the eigenvalues are what we need.

In this example we treat both the k-linear interaction between states $|y)_A$, $|t)_A$ and the electric dipole interaction between $|y)_A$ and the photon mode simultaneously (in one step). Alternatively we may also obtain polariton dispersion in two steps: First we could diagonalize the k-linear interaction and obtain the energy levels and oscillator strengths of two new exciton states $|Y)_A$, $|T)_A$; then carry out the eigenvalue method for $|Y)_A$, $|T)_A$ to obtain the polariton dispersion. As long as both interactions are small perturbations, those two methods should give the same result. Computer calculation showed this to be true.

Table 2.1. Simple Examples of Perturbation Ξ in C_{6v} Symmetry

		Time-Reversal Antisymmetric		Time-Reversal Symmetric			
Γ_1	S	K_z		$K_x^2+K_y^2$	$H_x^2+H_y^2$	$E_x^2+E_y^2$	$\varepsilon_{xx}+\varepsilon_{yy}$
					H_z^2	E_z	ε_{zz}
Γ_2	T		H_z				
Γ_3	V						
Γ_4	U						
Γ_5	X	K_x	H_y	K_xK_z	H_xH_z	E_x, E_xE_z	ε_{xz}
	Y	K_y	$-H_x$	K_yK_z	H_yH_z	E_y, E_yE_z	ε_{yz}
Γ_6	W			$K_x^2-K_y^2$	$H_x^2-H_y^2$	$E_x^2-E_y^2$	$\varepsilon_{xx}-\varepsilon_{yy}$
	Z			$2K_xK_y$	$2H_xH_y$	$2E_xE_y$	$2\varepsilon_{xy}$

Table 2.2. Multiplication Table of Product Perturbation $\Xi\Xi'$ in the C_{6v} Symmetry

Γ_1	S	SS'	TT'	UU'	VV'	XX'+YY'	WW'+ZZ'
Γ_2	T	ST'		UV'		XY'-YX'	WZ'-ZW'
Γ_3	V	SV'	TU'			YZ'-XW'	
Γ_4	U	SU'	TV'			XZ'+YW'	
Γ_5	X	SX'	TY'	UZ'	-VW'	XZ'-YW'	
	Y	SY'	-TX'	UW'	VZ'	YZ'+XW'	
Γ_6	W	SW'	TZ'	-UX'	-VX'	XX'-YY'	ZZ'-WW'
	Z	SZ'	-TW'	UY'	VY'	XY'+YX'	WZ'+ZW'

Table 2.3. Matrix Representation for the Exchange Interaction in C_{6v} Symmetry

$$
\begin{array}{ccccccccc}
 & |x)_A & |y)_A & |t')_A & |t)_A & |x)_B & |y)_B & |z)_B & |t)_B \\
|x)_A & 3j(\xi) & 9j_1\xi\eta & 0 & 0 & 3\gamma j(\xi) & 9\gamma j_1\xi\eta & 9\sqrt{2}\delta j_1\xi\zeta & 0 \\
|y)_A & & 3j(\eta) & 0 & 0 & 9\gamma j_1\xi\eta & 3\gamma j(\eta) & 9\sqrt{2}\delta j_1\eta\zeta & 0 \\
|t')_A & & & 0 & 0 & 0 & 0 & 0 & 0 \\
|t)_A & & & & 0 & 0 & 0 & 0 & 0 \\
|x)_B & & & & & 3\gamma^2 j(\xi) & 9\gamma^2 j_1\xi\eta & 9\sqrt{2}\delta\gamma j_1\xi\zeta & 0 \\
|y)_B & & & & & & 3\gamma^2 j(\eta) & 9\sqrt{2}\delta\gamma j_1\eta\zeta & 0 \\
|z)_B & & & \text{H.C.} & & & & 6\delta^2 j(\zeta) & 0 \\
|t)_B & & & & & & & & 0
\end{array}
$$

Note:

$$j(u) = j_0 + j_1(3u^2 - 1) \ .$$

Table 2.4. Matrix Representation for $H_S^{(c)} + H_S^{(v)}$ in C_{6v} Symmetry

	$\|x)_A$	$\|y)_A$	$\|t')_A$	$\|t)_A$	$\|x)_B$	$\|y)_B$	$\|z)_B$	$\|t)_B$
$\|x)_A$	$\alpha_2 S$	0	0	0	$-\eta_1 W$	$-\eta_1 Z$	$-\varepsilon_1 X$	$-\varepsilon_1 Y$
$\|y)_A$		$\alpha_2 S$	0	0	$-\eta_1 Z$	$\eta_1 W$	$-\varepsilon_1 Y$	$\varepsilon_1 X$
$\|t')_A$			$\alpha_2 S$	0	$-\varepsilon_1 X$	$\varepsilon_1 Y$	$\eta_1 W$	$-\eta_1 Z$
$\|t)_A$				$\alpha_2 S$	$\varepsilon_1 Y$	$\varepsilon_1 X$	$-\eta_1 Z$	$-\eta_1 W$
$\|x)_B$					$\alpha_1 S$	0	0	0
$\|y)_B$						$\alpha_1 S$	0	0
$\|z)_B$		H.C.					$\alpha_1 S$	0
$\|t)_B$								$\alpha_1 S$

Table 2.5. Matrix Representation

for $H_{as}^{(c)} + H_{as}^{(v)}$ in C_{6v} Symmetry

	$\|x)_A$	$\|y)_A$	$\|t')_A$	$\|t)_A$	$\|x)_B$	$\|y)_B$	$\|z)_B$	$\|t)_B$
$\|x)_A$	0	$-i\bar{\beta}_1T$	$-i\bar{d}_1V$	$i\bar{c}_1U$	$i\eta_1W$	$i\eta_1Z$	$i\bar{\varepsilon}_1X$	$i\bar{\varepsilon}_1Y$
$\|y)_A$	$-i\bar{\lambda}T$	0	$i\bar{c}_1U$	$-i\bar{d}_1V$	$i\eta_1Z$	$-i\eta_1W$	$i\bar{\varepsilon}_1Y$	$-i\bar{\varepsilon}_1X$
$\|t')_A$	$-i\bar{\mu}X$	$i\bar{\mu}Y$	0	$i\bar{\beta}_1T$	$i\bar{\varepsilon}_1X$	$-i\bar{\varepsilon}_1Y$	$-i\bar{\eta}_1W$	$i\bar{\eta}_1Z$
$\|t)_A$	$i\bar{\mu}Y$	$i\bar{\mu}X$	$-i\bar{\lambda}T$	0	$-i\bar{\varepsilon}_1Y$	$-i\bar{\varepsilon}_1X$	$i\bar{\eta}_1Z$	$i\bar{\eta}_1W$
$\|x)_B$					0	$-i\bar{\beta}_2T$	$-i\bar{\varepsilon}_3X$	$i\bar{\varepsilon}_3Y$
$\|y)_B$					$i\bar{\lambda}T$	0	$-i\bar{\varepsilon}_3Y$	$-i\bar{\varepsilon}_3X$
$\|z)_B$					$i\bar{\mu}X$	$i\bar{\mu}Y$	0	$i\bar{\beta}_2T$
$\|t)_B$					$i\bar{\mu}Y$	$-i\bar{\mu}X$	$i\bar{\lambda}T$	0

Note: the complete matrix should be obtained by adding complex conjugate of all the elements to their opposite corners.

References

1. K. Cho, Phys. Rev. B14, 4463 (1976).

2. K. Cho, in: Excitons edited by K. Cho (Springer-Verlag, New York, 1979).

3. K. Cho, Solid State Commun. 27, 305 (1978).

Chapter 3. Experiment

In this chapter we describe the arrangement, apparatus and procedure used in the experiments described in Chapters 4, 5, 6, and 7. Specialized techniques will be presented in the individual chapters.

3.1. The experimental arrangement

The experimental arrangement used for RBS studies is shown in block form in Fig. 3.1. A Krypton ion laser was used to pump a cw dye laser in order to obtain tunable single mode output radiation. The dye laser output was monitored via a pair of beam-splitters in order to (1) maintain a constant dye output power through the use of a dye laser light stabilizer, and (2) monitor the mode spectrum of the output radiation using an optical spectrum analyzer and an oscilloscope, and focused onto the sample via lens L_1.

The samples used were vapor-grown single crystal CdS platelets generously provided by Dr. D. M. Roessler of the General Motors Research Laboratory. The crystal, with the crystallographic c-axis in the plane of the sample, had typical surface area dimensions of 3mm x 5mm with thickness ~ 10^{-2} cm. The sample was attached to a cold-finger in a LT-3-110 Heli-Tran Liquid Helium Transfer Refrigerator (Cryo-tip), as in the most of our RBS experiments, or a copper mount in a SUPER VARITEMP liquid helium dewar, as in our RBS experiments at superfluid helium temperatures via a mixture of Cryo-con grease and N-grease (1:1).

Backward light scattering was used with both the incident wavevactor and the polarization of the dye laser light perpendicular to the crystal c-axis which is parallel to the crystal surface. The use of a backscattering geometry is necessary because of strong absorption of both incident and scattered light in a medium near an exciton resonance region. A Light scattered by the sample was collected and focused onto a pinhole P_1 by a lens L_2. A Nikon lens L_3 then collimated the light passing through the pinhole P_1 which acted as a point source. The parallel light so obtained was reflected from a system of two mirrors which served the purpose, along with the Nikon collimating lens L_3, of aligning the collected light with the optical axis of the triple-pass Fabry-Perot interferometer. The light emerging from the ramped Fabry-Perot was then focused onto the vertical spectrometer slit which, along with a brass horizontal slit, formed a second pinhole P_2. The f-numbers of the lenses used were chosen to match that of the spectrometer. Light leaving the spectrometer was focused onto the cathode of a photomultiplier tube whose output was processed with photon counting electronics and recorded on a strip chart recorder, or occasionally multiscaled into a PDP-8E minicomputer.

The focal lengths of the sample focusing lens L_1, pinhole focusing lens L_2, Fabry-Perot colimating lens L_3, and spectrometer focusing lens L_4 (immediately followed by a polarization scrambler) are 16, 10, 5.5, and 18.7 cm, respectively. The diameters of the pinholes

P_1 and P_2 are 200 and 150 microns, respectively.

3.2. Apparatus

A summary of the apparatus used in the RBS experiments is given in Table 3.1. Brief descriptions of the main components are given below.

1. Krypton Laser

A SPECTRA PHYSICS model 171 krypton ion laser with deep-blue mirrors was used as the pump laser. The output was between 1.3 and 1.8 Watts for all lines in the deep blue region (4067 ~ 4226 Å). The output was TEM_{00} mode and vertically polarized. This laser was operated in the light-control mode whereby its power supply current constantly adjusted by an external dye laser light stabilizer (see below).

2. Dye Laser[1]

The output of the krypton laser was used to pump a COHERENT RADIATION model 590 dye laser to provide a source of quasi-continuously tunable coherent single mode light. The dye medium was a methanol-ethylene glycol solution of the dye coumarin 102 (made by EXCI-

TON CHEMICAL CO. INC.) which absorbs in the band 4000 to 4200 Å and emits at longer wavelengths 4700 to 5150 Å through fluorescence. The dye solution was made by uniformely mixing 0.667 grams of the coumarin 102 powder with 200 ml of high quality methanol and 800 ml of ethylene glycol. Selection of nearly monochromatic radiation from the broad dye fluorescence bandwidth was achieved through the use of a quartz birefringent filter consisting of three quartz plates of different thicknesses placed in the cavity at Brewster's angle. A double etalon system consisting of a thick (10 mm) coated etalon and a thin (0.5 mm) coated etalon was used to obtain single mode monochromatic output with a frequency width of less than 100 MHz (0.003 cm^{-1}).

Tuning of the output frequency was accomplished as follows: frequency changes on the order of a thin etalon mode hop (6 ~ 7 cm^{-1}) were obtained by rotating the birefringent filter about its surface normal. Small frequency changes were made by tilting the thin etalon with respect to the cavity beam enabling the laser frequency to hop between thick etalon modes (0.3 cm^{-1} separations). The thick etalon could be adjusted slightly in order to compromise between high power (or low current in case of light mode) and mode stability whenever necessary.

Certain instabilities in the output frequency spectrum of the dye laser complicated the RBS experiments, the most important of which was fluctuation of the output power which introduced thin etalon mode hopping. This problem was partially alleviated by incorporating a light stabilizer into the experimental setup. However, mode hops still occurred on the average of every five minutes. Thus, the output mode spectrum of the dye laser had to be continuously monitored by a spectrum analyzer (see below) so that undesirable modes could be eliminated through the tilting of the thin etalon.

3. Dye Laser Stabilizer

The dye laser output power was maintained at 8 mW by the dye laser light stabilizer (SPECTRA PHYSICS, model 373). This consisted of a detector head and a control unit. The detector head contains a beamsplitter which reflects 3.5 % of the laser light onto a photocell detector. The signal created by the photocell (0.75 μA/mW) is amplified and compared with a DC reference signal specified by the level control (located on the front of the control unit) which sets the desired operating power level of the light stabilizer. The amplified difference of the two signals produces a current that is returned to the krypton ion laser control circuitry which then compensates for the dye laser power variations by changing the pump laser output power. The output power of the dye laser could be stabilized to within ± 0.5 % per hour for a fixed wavelength. In addition, the light stabilizer also acted as a power meter with its meter accurate to within ± 10 %.

4. Spectrum Analyzer

The spectrum of the dye laser light was observed with an optical spectrum analyzer (COHERENT OPTICS, model 760) in conjunction with a dual-beam oscilloscope (TEKTRONIX, model 556) and an amplifier (KEITHLEY INSTRUMENTS, model 102C). The oscilloscope was used to both ramp the spectrum analyzer and display its amplified output. The free spectral range (FSR) of the spectrum analyzer was 8 GHz (≈ 0.27 cm^{-1}).

5. Cryogenic Systems

The samples were vertically attached to a cold-finger copper sample holder in the Cryo-tip via a conductive vacuum grease mix consisting of Cryo-con and N-grease (1:1). Optical access to the sample was provided by fused quartz windows on the Cryo-tip. Cooling of the sample was achieved by continuous flow of liquid helium through the tip flow capilary and the sample holder. Temperature was measured using a gold-chromel thermocouple which was in thermal contact with the sample holder. Most of the experiments were performed at 4.2 K nominal temperature, although sample temperatures were usually somewhat higher due to absorption heating. The schematic representation of the Cryo-tip system is given in Fig. 3.2.

When performing RBS experiments at superfluid-helium-temperatures with samples immersed in liquid helium ($T < 2.17$ K), we used a liquid-helium dewar (JANIS SUPER VARITEMP, model DT) equipped with a carbon-glass temperature sensor (LAKE SHORE, model CGR-1-1000, working current 10 μA, calibration temperature range 1.4 - 20 K). In order to obtain superfluid-helium-temperatures, a mechanical pump (WELCH, model 1397, pumping speed 425 liters/min.) was used to evacuate the sample tube of the dewar with the needle valve of the dewar slightly opened to let liquid helium continuously flow into the sample tube from the helium reservoir.

6. Electromagnet

The cold finger of the Cryo-tip system was placed in the center of an electromagnet (MAGNION, model L-128A-12 inch) of pole face diameter 8 $\frac{3}{8}$ inches and gap width 3 $\frac{3}{16}$ inches. The magnet required a power of 130 VDC and 65 Amperes maximum, and cooling water 2 gpm minimum.

The magnet power supply (MAGNION, model HS-1365B/FFC-4) was a field regulated one which required a 3-phase AC power of 208 V, 35 Amperes.

7. Fabry-Perot Interferometer[2]

A triple-pass Fabry-Perot interferometer (BURLEIGH INSTRUMENTS, model RC-110) was used for high-resolution spactral analysis of the scattered light. This Fabry-Perot used two $\lambda/200$ plane mirrors which were coated for 93 % reflectivity in the spectral region 4500 - 5500 Å. Piezoelectric ceramic transducers (PZT) were used to scan and align one of the plane mirrors with respect to the other mirror which remained fixed. The ramp voltage (0 to 1000 volts, sawtooth in time) applied in the scanning mode to each of the PZT elements was supplied by a ramp generator (BURLEIGH, model RC-44). Two corner-cube retro-reflectors were utilized to obtain triple-pass operation. Several free spectral ranges (FSR) ranging from 1 to 14 cm^{-1} were used. The finesse of the interferometer varied between 50 and 70 with a working contrast of ~ 1×10^6.

8. Double-Grating Spectrometer

After passing the interferometer the scattered light also traversed a 3/4 meter (focal length of the first mirror) SPEX model 1401 Czerny-Turner double grating spectrometer whose f-number was ~ 6.3. The spectrometer served two purposes: (1) it determined the incident dye laser frequency by scanning the scattered Rayleigh light, and (2) it acted as a tunable laser filter allowing only Rayleigh and desired Brillouin components to pass during the Fabry-Perot scan.

9. Photomultiplier Tube

The light leaving the spectrometer was focused onto the cathode of an ITT FW130 photomultiplier tube. The tube was maintained at - 20 C by a model TE-104 thermoelectric refrigeration unit manufactured by PRODUCTS FOR RESEARCH. The dark count of the cooled tube was about 3 counts/second. A POWER DISIGNS, INC. model 2K-20 power supply provided 1750 volts to the photomultiplier tube. Two screws near the output slit of the SPEX 1401 adjust the final lens position to focus on the photomultiplier tube.

10. Photon-counting Electronics

The photon-counting electronics comprised a "PAD" (CANBERRA, model 813) which combines a preamplifier, amplifier and discriminator in a single Nim bin module. The output of the discriminator was fed to a ratemeter (ORTEC, model 880) and recorded on a strip chart recorder (HONEYWELL, model 194).

3.3. The Experimental Procedure

Our RBS experiments utilized a backscattering geometry ($x[y\ y]\bar{x}$) with both the wavevector and polarization of the incident light perpendicular to the c-axis of the crystal ($\mathbf{k} \perp \mathbf{c}$, $E \perp \mathbf{c}$). The incident power was maintained at 8 mW by the dye laser light stabilizer discussed earlier.

The experimental procedure will be described. The dye laser was first tuned to some frequency in the vicinity of the A-exciton in CdS (~ 20588.8 cm^{-1}). During this time, the output of the 8 GHz spectrum analizer was carefully viewed on the oscilloscope in order to verify that the dye laser output consisted of a single frequency.

The laser frequency was determined by allowing the Fabry-Perot interferometer to quickly ramp through its FSR with a ramp duration of 20 ms. Since the elastic Rayleigh component is dominent in the output of the Fabry-Perot, the laser frequency can be obtained by slowly scanning the grating spectrometer with narrow slit width (100-50-50 microns) over this elastic component. The slow scan (37.5 cm^{-1}/min) allowed the experimenter to mark the strip chart record in 1 cm^{-1} intervals by visual comparison with the spectrometer wavenumber indicator. Subsequent interpolation between the 1 cm^{-1} marks allowed the laser frequency to be determined to the nearest 0.1 cm^{-1}. Measurements made in this way were reproducible to about 0.2 cm^{-1}.

After the laser frequency was determined, we positioned the central frequency of the grating spectrometer and opened its slits (100-500-500 microns) to select the desired Stokes (or anti-Stokes) components as well as the Rayleigh line. Then we adjusted the scan range of the Fabry-Perot to contain two adjacent orders of the Rayleigh component by viewing the photomultiplier output and Fabry-Perot ramp voltage on the oscilloscope.

We then stopped the Fabry-Perot scan at the middle point of its FSR, and optimized the signal intensity by adjusting the spectrometer focusing lens and the three ramp bias voltages of the Fabry-Perot interferometer and viewing the photomultiplier output on the ratemeter.

Then the Fabry-Perot was scanned through its FSR in ~ 100 seconds and the output of the combined Fabry-Perot-grating spectrometer system was recorded on a strip chart recorder. The frequency of the dye laser was then changed by tilting the thin etalon as previously described. The above procedure was then repeated. The end results were then a series of Stokes (Anti-Stokes) Brillouin spectra for a range of dye laser frequencies spanning the A-exciton resonance region. The effective resolution of this combined system was about 0.1 cm^{-1} for a FSR of 6.5 cm^{-1}, or 0.015 cm^{-1} for a FSR of 1.0 cm^{-1}.

Since the finesse f of the Fabry-Perot was approximately a constant for different FSR, the resolution R is proportional to the FSR (R = FSR/f), i.e. the smaller the FSR, the higher the resolution one could obtain. However, too small a FSR makes the spectra of different Fabry-Perot orders overlap and identification of Brillouin components difficult. We should choose the best FSR by considering both effects.

The FSR of the Fabry-Perot was usually measured by deliberately allowing two thin etalon modes to be present in the dye laser output. This light was then scattered off a piece of teflon located within the helium dewar. The separation between these two modes was obtained by scanning the grating spectrometer over the scattered light. This turned out to be approximately 6.7 cm^{-1}. The spectrometer was then positioned midway between the two modes while its slits were opened to pass both of them. The Fabry-Perot then scanned the modes, the spectrum of which was recorded on the strip chart recorder. Since the separation between the modes was known, the FSR could be calculated from the strip chart record. A second method was to use a standard mercury or sodium doublet (e.g. for Hg: 5789.66 and 5790.66 Å whose separation is 2.98 cm^{-1}; for Na: 5889.95 and 5895.92 Å whose separation is 17.20 cm^{-1}) instead of two adjacent thin etalon modes from the dye laser.

Table 3.1. List of Apparatus

Apparatus	Manufacturer	Model
Krypton laser	Spectra-Physics	171
Krypton laser power supply	Spectra-Physics	270
Dye laser	Coherent Radiation	590
Dye laser stabilizer	Spectra Physics	373
Spectrum analyzer	Coherent Optics	760
Amplifier	Keithley Instruments	102C
Dual beam oscilloscope	Tektronics	556
Helium dewar	Janis	DT
Heli-tran liquid helium transfer refrigerator	Air Products and Chemicals, Inc.	LT-3-110
Electromagnet	Magnion	L-128A-12 inch
Magnet power supply	Magnion	HS-1365B/ FFC-4
Fabry-Perot interferometer	Burleigh Instruments	RC-110
Ramp generator	Burleigh Instruments	RC-44
Double-grating spectrometer	Spex	1401
Photomultiplier tube	ITT	FW130
PM Refrigeration unit	Products for Research	TE-104
Photomultiplier power supply	Power Designs, Inc	2K-20
Portanim (Nim bin module)	Berkeley Nucleonics, Corp.	AP-1
Preamplifier, amplifier, discriminator	Canberra	813
Ratemeter	Ortec	880
Strip chart recorder	Honeywell	194

References

1. A. Dienes, in: Laser applications to Optics and Spectroscopy edited by S. F. Jacobs, M. Sargent III, J. F. Scott and M. O. Scully (Addison, Massachusetts, 1975).

2. J. R. Sandercock, in: Proceedings of the Second International Conference on Light Scattering in Solids edited by M. Balkanski (Flammarion, Paris, 1971) p.9.

Chapter 4 . Frequency-Dependent Polariton Damping and RBS Linewidth in CdS

In Chapters 4 to 7 we present the experimental investigations of RBS in CdS which form the core of this thesis. In Chapter 4 we investigate the dependence of RBS linewidths on laser frequency and propose a frequency-dependent polariton damping model. In Chapter 5 we discuss our experiments in a weak magnetic field which gave the first evidence for a k-linear interaction through the dependence of linewidths on magnetic field. In Chapter 6 we present our most recent studies of RBS at superfluid helium temperatures in which splitting of RBS components due to three-branch polariton behavior was observed directly for the first time. In Chapter 7 we explore the effect of the ABC on RBS intensity and attempt to establish the correct ABC by comparison with our experimental data.

RBS linewidth measurements were reported by Weisbuch and Ulbrich[1] for GaAs, by Hermann and Yu[2] for CdSe and by Wicksted et al for CdS.[3,4] In these experiments significant disagreement with the predictions of the BZB theory with a frequency-independent damping term were noted. On the other hand, the bottleneck[5] effect of exciton-polaritons observed in luminescence spectra indicates that the lifetime of polaritons changes considerably in the region of the resonance frequency.[6,7] Also, it was proposed by Yu that the damping constant should be proportional to k^2 where k is the polariton wavevector.[8] Before the present work, however, no systematic investigations of RBS linewidths had been reported, primarily because of the difficulty of the experiments.

The intensity of RBS has been studied fairly extensively because it is sensitive to the ABC problem. The intensity, however, depends not only on the ABC, but also on other factors such as the dead layer thickness.[9] Recent numerical calculations by Matsushita et al have shown that even in the absence of a dead layer, the RBS intensity depends strongly on the damping constant γ.[10] Therefore, it is crucial to know the frequency-dependence of γ before one attempts to use RBS intensity data to resolve the ABC problem.

In this chapter, We report the measurements and analysis of the linewidth of RBS components from the lower branch (branch 2) A-exciton polaritons in CdS. We discuss different forms for $\gamma(\omega)$ and propose a new line-broadening mechanism - the decay of Γ_{5T} polaritons into dipole-forbidden Γ_6 excitons via the k-linear interaction.[11]

4.1. Experiment

The general features of the experiment was already given in chapter 3. The sample used in this experiment was numbered CdS 21E-2. The solid angle of the collected scattered light outside the crystal was about $10^{-2}\pi$ Str, and the refractive index in the resonance region $n \approx 7.5$, so the range of internal scattering angles was about

$179.2^\circ \pm 0.8^\circ$. Therefore, line broadening effect due to finite collection angle was less than 5×10^{-5} of the Brillouin shift and can be ignored.

Above the resonance frequency a slight local heating effect was observed as an increase of Brillouin shift with increasing laser power. We chose 8 mW laser power as a compromise between reduction of local heating and maintaining suitable signal intensity.

The diameter of the first pinhole was ~ 200 μm which defined the scattering volume. We kept the laser power constant and reduced the pinhole diameter from 200 μm to 10 μm; no change in linewidth was observed. Thus we confirmed that the local heating effect did not cause significant inhomogeneous line broadening for 8 mW laser power and 200 μm pinhole diameter.

However, the local heating effect could still raise the sample temperature and lower the exciton resonance frequency ω_0 (i.e. ω_T). Thus the laser frequency should be rescaled before one obtains experimental linewidths (or any other quantities) vs. incident laser frequency curves. The laser frequency correction due to the local heating effect could be obtained by comparison of the experimental Brillouin shift data to the theoretical one at liquid helium temperature. We noticed that this correction, ranging from 0 to 5 cm^{-1} (corresponding to temerature correction 0 to 5 K), would vary from time to time depending on the thermal conduction between the crystal and the sample holder and the tip flow strength in the Cryo-tip system during the experiment.

The FSR used in most of the present work was from 8 to 14 cm^{-1} giving an instrumental linewidths of about 0.2 cm^{-1}. Below the resonance region where the linewidth were very narrow, a smaller FSR (1 ~ 4 cm^{-1}) was used to measure linewidths.

We have concentrated on LA 2-2' scattering rather than TA 2-2' scattering studied in Ref. 3 because the LA 2-2' component has the largest Brillouin shift and can be studied over the largest range of laser frequencies. Moreover, the LA linewidth is approximately twice as large as the TA linewidth and therefore allows more accurate linewidth determination.

The full width at half maximum of each Brillouin component was obtained by subtracting the average Rayleigh linewidth from the observed Brillouin linewidth, assuming that both lines are Lorentzian which is approximately true for $\omega < \omega_L$. Deconvolution of the lineshape was not performed.

Fig. 4.1 shows the raw spectra of the Stokes LA 2-2' Brillouin component as the incident laser frequency was varied from below ω_T to above ω_L. The observed Brillouin shifts agreed well with our previous data,[3] and in the following analysis we used the parameters given in Table 1.2.

The experimentally observed linewidths (after subtraction of the instrumental linewidth) are shown by the solid dots in Fig. 4.2 (a) - (c), while the solid lines are calculated linewidths based on three different models for $\gamma(\omega)$, to be discussed below. For laser frequencies well below ω_T, the linewidth is small and close to the limit of resolution when the FSR of the Fabry-Perot is large (8 to 14 cm^{-1}).

However, these linewidths were also measured with high resolution (FSR ≈ 1.2 to 4 cm^{-1}) and found to be independent of the FSR used in the measurement, in contrast to the results of Flynn and Geschwind.[12]

The observed linewidth increases from 0.03 cm^{-1} to about 0.3 cm^{-1} within a narrow range of laser frequencies between 20,585 and 20,595 cm^{-1} and remains approximately constant for higher frequencies. Although the data at high laser frequencies exhibit considerable fluctuation, a slight decrease in linewidth around 20,598 cm^{-1} was observed repeatedly in several series of experiments and is believed to be a real effect. For higher frequencies, a rapid decrease in the RBS intensity as well as increasingly serious local heating (even with 8 mW of laser power) made accurate measurement of the linewidth very difficult.

The linewidths of the anti-Stokes LA 2-2' Brillouin component were also measured and are shown by the solid dots in Fig. 4.4. The sharp increase and the slight decrease in linewidth occured approximately 5 cm^{-1} lower in frequency than for the Stokes LA 2-2' component since for anti-Stokes scattering the scattered polaritons have higher frequency than the Stokes scattering.

4.2. Theory

1. Physical Origin of the k-Linear Interaction[13]

The k-linear term in the exciton energy originates from the k-linear terms in the conduction electron and valence hole energies. Group theory shows that energy bands of Γ_7 symmetry should be of the form[14]

$$E = A(k_x^2 + k_y^2) + Bk_z^2 \pm C(k_x^2 + k_y^2)^{1/2}. \qquad (4.1)$$

The third term, linear in k, represents the splitting of the two spin states by an amount $2C(k_x^2 + k_y^2)^{1/2}$ for wavevectors perpendicular to the c-axis ($\mathbf{k} \perp \mathbf{c}$). It can be derived from the spin-orbit interaction as follows.

Effective mass theory gives the Bloch band electron energy in a uniaxial crystal as:

$$\begin{aligned} H_0 &= \frac{\hbar^2}{2m_\perp}(k_x^2 + k_y^2) + \frac{\hbar^2}{2m_{/\!/}}k_z^2 \\ &= A(k_x^2 + k_y^2) + Bk_z^2. \end{aligned}$$

In uniaxial crystals, a crystal field $\mathbf{E_z}$ may exist along the z-direction ($\mathbf{z} \,||\, \mathbf{c}$, where $\mathbf{c}$ is the crystal axis) which is seen by an electron moving in the x-y plane ($\mathbf{k} \perp \mathbf{c}$) as an effective magnetic field. Using the Lorentz transformation, the fields ($\mathbf{E'}$, $\mathbf{B'}$) seen by the electron moving with a velocity $\mathbf{v}$ in the absence of external magnetic fields will be:

$$\mathbf{E'}_{||} = \mathbf{E}_{||} = 0$$

$$\mathbf{E'}_\perp = \gamma_v(\mathbf{E}_\perp + \mathbf{v} \times \mathbf{B}) = \gamma_v \mathbf{E_z} \qquad (4.2)$$

$$\mathbf{B'}_{||} = \mathbf{B}_{||} = 0$$

$$\mathbf{B'}_\perp = \gamma_v(\mathbf{B}_\perp - \frac{\mathbf{v}}{c^2} \times \mathbf{E}) = -\frac{\gamma_v}{c^2}\, \mathbf{v} \times \mathbf{E_z} \,,$$

where the subscript || represents the field components along the direction of electronic motion, $\perp$ represents that along the direction perpendicular to the electronic motion, and

$$\gamma_v = (1-v^2/c^2)^{-1/2}.$$

The coupling between electron spin $\vec{\sigma}$ and $B'_\perp$ produces a perturbation to H_0:

$$H' \sim \vec{\sigma}\cdot\mathbf{B'}_\perp \propto \vec{\sigma}\cdot\mathbf{E}_z \times \mathbf{v}$$

i.e.

$$H' = C(k_x\sigma_y - k_y\sigma_x) .$$

Using Pauli matrices for σ_x and σ_y, the total Hamiltonian $H = H_0 + H'$ will be

$$H = \begin{bmatrix} A(k_x^2 + k_y^2) + Bk_z^2 & -iC(k_x - ik_y) \\ iC(k_x + ik_y) & A(k_x^2 + k_y^2) + Bk_z^2 \end{bmatrix} . \qquad (4.3)$$

The electronic energy is obtained by solving

$$H\Psi = \varepsilon\Psi ,$$

thus

$$\varepsilon_\pm = A(k_x^2 + k_y^2) + Bk_z^2 \pm C(k_x^2 + k_y^2)^{1/2}.$$

The last term in this equation is called the k-linear or finite slope band crossing term which comes from the spin-orbit interaction of Bloch states. The k-linear term for excitons comes from the combined k-linear terms of the conduction electron and the valence hole. The k-linear coefficient ϕ of excitons is related to those of conduction and valence bands by[15]

$$\phi = (C_h m_{h\perp} - Ce\, m_{e\perp})/(m_{h\perp} + m_{e\perp}) . \qquad (4.4)$$

The existence of the k-linear term in the second valence band Γ_7 has been used to explain the anomalous structure (shoulder) near ω_T of the 1s B-exciton in the reflectivity spectra in CdS.[16] It is also responsible for the three-branch polariton behavior in RBS near the B-exciton resonance with $\mathbf{E} \perp \mathbf{c}$, $\mathbf{k} \perp \mathbf{c}$ due to the mixing of the dipole allowed Γ_5 state and forbidden Γ_2 state.[15] However, no evidence for the k-linear effect in the 1s A-exciton has been reported before the present work.

2. Theoretical Models for the Polariton Damping $\gamma(\omega)$

We have considered three contributions to γ corresponding to different decay mechanisms of polaritons in attempting to determine $\gamma(\omega)$ from the measured linewidths. These are (i) a frequency-independent damping constant γ_0, (ii) a decay via elastic scattering, and (iii) damping due to the decay of the $\Gamma_{5T}(A)$ polaritons to $\Gamma_6(A)$ excitons via a linear wavevector-induced mixing of states which is significant only in the resonance region.

After making a theoretical model for $\gamma(\omega)$, the complex wavevector of polaritons $\mathbf{k} = \mathbf{k}' + i\mathbf{k}''$ can be calculated from the polariton dispersion relation Eq. (1.13) while the RBS linewidth can be calculated from Eq. (1.29) and compared with our experimental data.

Model I, consisting of the frequency-independent γ_0 alone, is the simplest approximation. γ_0 can represent both radiative recombination and nonradiative decay (impurity trapping etc.) because such interactions can scatter a polariton regardless of its wavevector or energy. The solid curve in Fig. 4.2(a) is the calculated best fit to model I, with

$$\tilde{\gamma}_0 = (0.63 \pm 0.05)\ \mathrm{cm}^{-1}. \tag{4.5}$$

Obviously, the steep increase of the linewidth just above ω_T cannot be explained by γ_0 alone.

Decay of polaritons via intrabranch elastic scattering by impurities and scattering by acoustic phonons can be taken into account by including term (ii) since the transition probability for such scattering is roughly proportional to the density of states at energy ω if the detailed ω and/or $\mathbf{q}$ ($\mathbf{q} = \mathbf{k}_I - \mathbf{k}_S$) dependence of the interaction is neglected. Assuming that the energy difference between the initial and final states in a scattering event is small enough (i.e., elastic scattering or scattering by acoustic phonons is dominant), and also neglecting the anisotropy of the CdS wurtzite structure, the density of states is proportional to $k'(\omega)^2/|V_G(\omega)|$. In model II we have included both terms (i) and (ii) with a total $\gamma(\omega)$ given by

$$\gamma(\omega) = \gamma_0 + \gamma_1 \left[\frac{k'(\omega)}{k_0}\right]^2 \left[\frac{V_{G0}}{V_G(\omega)}\right] \tag{4.6}$$

where $k_0 = (\omega_T \varepsilon_b^{1/2}/c)$ and $V_{G0} = V_G(\omega_T)$ have been introduced for normalization purposes. Since the density of states for the lower polariton branch is a monotonically increasing function of ω, the damping constant $\gamma(\omega)$ and the Brillouin linewidth will therefore increase with increasing frequency. Fig. 4.2(b) shows the best fit to model II with the constants

$$\tilde{\gamma}_0 = (0.12 \pm 0.01)\ \mathrm{cm}^{-1}$$

$$\tilde{\gamma}_1 = (0.35 \pm 0.03)\ \mathrm{cm}^{-1} \cdot \qquad (4.7)$$

The $\gamma(\omega)$ of Eq. (4.6) fits the observed linewidth better than γ_0 alone, but is still not satisfactory.

It should be noted that if the intrabranch decay of polaritons came primarily from acoustic phonon scattering which conserves energy and momentum, the second term of Eq. (4.6) would be[11]

$$\gamma_1(\omega) \propto \int |\Gamma_0(q)|^2\, \delta(\hbar\omega_I - \hbar\omega_S - \hbar c|\mathbf{q}|)\, d\mathbf{q} \quad \propto \quad k'(\omega)^2 \qquad (4.8)$$

instead of $k'(\omega)^2/|V_G(\omega)|$. However, since $k'(\omega)^2$ increases more slowly than $k'(\omega)^2/|V_G(\omega)|$, the linewidth calculated using Eq. (4.8) was found to give a worse fit to the data than that shown in Fig. 4.2(b).

Next, we consider the third term (iii) in $\gamma(\omega)$. From symmetry considerations, the k-linear interaction can exist in the 1s A-exciton states due to the Γ_7 conduction band which will mix $\Gamma_6(A)$ spin triplet and $\Gamma_{5T}(A)$ spin singlet exciton states. In the presence of this interaction, three modes must be included in the calculation: $\Gamma_{5T}(A)$ and $\Gamma_6(A)$ excitons, and photons. Instead of the two-branch dispersion curves given by Eq. (1.13), one then has three-branch dispersion curves. From Eqs. (2.23) and (2.33) the polariton dispersion is given by

$$\begin{array}{ccc} |\Gamma_{5T}(A)\rangle & |\Gamma_6(A)\rangle & |\text{photon}\rangle \\ & & \\ \omega_T+B_5k^2-i\gamma/2-\omega & -iek & (2\pi\alpha_0\,\omega_T)^{1/2} \\ iek & \omega_6+B_6k^2-i\gamma_6/2-\omega & 0 \\ (2\pi\alpha_0\,\omega_T)^{1/2} & 0 & -\varepsilon_b+k^2c^2/\omega^2 \end{array} = 0 . \qquad (4.9)$$

where $B_5 = \hbar/2M$, $B_6 = \hbar/2M_6$, $\omega_6 = \omega_T-\Delta st$, ω_6, M_6 and γ_6 are the resonance frequency, effective mass and damping constant of the $\Gamma_6(A)$ state, and we assume $M_6 = M$, $\gamma_6 = \gamma$, $\varepsilon'_b = \varepsilon_b$, Δst is the frequency difference between the singlet $\Gamma_{5T}(A)$ and triplet $\Gamma_6(A)$ exciton states at $\mathbf{k} = 0$, and $e = \phi_A/\hbar$, ϕ_A is the coefficient of the k-linear interaction. In the following calculation the values of the relavent parameters are taken from Table 1.2. Eq. (4.9) can be solved as a function of real frequency ω by reducing it to an eigenvalue problem with respect to the complex wavevector k as we described in Chapter 2. Fig. 4.3 shows the dispersion curves for the three branches Γ_α, Γ_β and Γ_γ, the last of which is almost the same as the usual upper polariton branch 1 in the two-branch model of Eq. (1.13). These curves for $k'(\omega)$ are insensitive to the damping constants $\tilde{\gamma}$, which has been taken as 0.5 cm^{-1} in the calculation leading to Fig. 4.3.

Since the $\Gamma_6(A)$ frequency $\tilde{\omega}_6$ at $\mathbf{k} = 0$ is 1.6 cm^{-1} below the $\Gamma_{5T}(A)$ exciton, the lower two branches would cross at $\tilde{\omega}_{cr} \approx 20594.0$ cm^{-1}, but the k-linear interaction converts this to an anticrossing. Most polaritons are created on the Γ_β branch for $\omega > \omega_{cr}$ and on the Γ_α branch for $\omega < \omega_{cr}$ because Γ_6 excitons do not couple to photons. To first approximation, we neglect the upper polariton branch Γ_γ and consider the mixing of Γ_6 excitons with lower-branch Γ_{5T} polaritons ($\Gamma_{5\ell}$). Since the exciton strength function $A_{22} \approx 1$ in the resonance region,[10] the k-linear interaction between these two branches is still iek. Thus in terms of the unperturbed wave functions $|\Gamma_{5\ell}(A)\rangle$ and $|\Gamma_6(A)\rangle$, the Schroedinger equation can be written

$$\begin{pmatrix} \omega_{5\ell}-\omega & -iek \\ iek & \omega_6-\omega \end{pmatrix} \begin{pmatrix} C_5 \\ C_6 \end{pmatrix} = 0. \tag{4.10}$$

which gives eigenvalues

$$\omega_\alpha = \frac{\omega_{5\ell}+\omega_6}{2} - \left[\frac{(\omega_{5\ell}-\omega_6)^2}{4} + (ek)^2\right]^{\frac{1}{2}}$$

$$\omega_\beta = \frac{\omega_{5\ell}+\omega_6}{2} + \left[\frac{(\omega_{5\ell}-\omega_6)^2}{4} +(ek)^2\right]^{\frac{1}{2}} \tag{4.11}$$

and eigenstates

$$|\Gamma_\alpha(A)\rangle = C_{\alpha 5}\, |\Gamma_{5\ell}(A)\rangle + C_{\alpha 6}\, |\Gamma_6(A)\rangle$$

$$|\Gamma_\beta(A)\rangle = C_{\beta 5}\, |\Gamma_{5\ell}(A)\rangle + C_{\beta 6}\, |\Gamma_6(A)\rangle \tag{4.12}$$

with

$$|C_{\alpha 6}|^2 = \frac{e^2k^2}{(\omega_6 - \omega_\alpha)^2 + e^2k^2}$$

$$|C_{\beta 6}|^2 = \frac{e^2k^2}{(\omega_\beta - \omega_6)^2 + e^2k^2} \tag{4.13}$$

giving the fraction of Γ_6 in the mixed Γ_α or Γ_β states. This Γ_6 part of the polariton can decay to other states on the Γ_6 exciton branch via successive interactions with acoustic phonons or defects. Thus, the wavevector-induced interaction can open an extra decay channel for the $\Gamma_{5\ell}$ polaritons with $\omega \approx \omega_{cr}$. In the present chapter, we consider the result of the mixing of Γ_{5T} polaritons and Γ_6 excitons to be an additional broadening of the Brillouin components. In Chapter 6 we will report on high resolution experiments at superfluid helium temperatures where the linewidths are considerably reduced. We will then show that the effect of the mixing is to split the components into two resolvable sub-components. In view of the simplified model adopted here, for $\omega < \omega_{cr}$ we approximate the energy difference $|\omega_6 - \omega_\alpha|$ by $\delta E = \omega_\beta - \omega_\alpha$ calculated at $k'(\omega)$ of the unperturbed lower-branch polariton $\Gamma_{5\ell}$ (see Fig. 4.3) and take $\gamma \propto |C_{\alpha 6}|^2$. For $\omega > \omega_{cr}$, we approximate the energy difference $|\omega_\beta - \omega_6|$ by δE and take $\gamma \propto |C_{\beta 6}|^2$. We then use the following form for the total damping constant $\gamma(\omega)$ (model III)

$$\gamma(\omega) = \gamma_0 + \gamma_1 \left[\frac{k'(\omega)}{k_0}\right]^2 \left[\frac{V_{G0}}{V_G(\omega)}\right] + \gamma_2 \frac{|ek(\omega)|^2}{\delta E(\omega)^2 + |ek(\omega)|^2} . \qquad (4.14)$$

The three terms on the right hand side in Eq. (4.14) correspond to the three decay mechanisms (i), (ii) and (iii) discussed earlier in this section. The solid line in Fig. 4.2(c) is the best fit to Eq. (4.14) with

$$\begin{aligned} \tilde{\gamma}_0 &= (0.24 \pm 0.02)\ \text{cm}^{-1} \\ \tilde{\gamma}_1 &= (0.09 \pm 0.01)\ \text{cm}^{-1} \qquad (4.15) \\ \tilde{\gamma}_2 &= (2.7 \pm 0.3)\ \text{cm}^{-1} \\ e &= (2.9 \pm 0.3) \times 10^4\ \text{cm/sec} . \end{aligned}$$

It is seen that the frequency-dependence of the Brillouin linewidth including the rapid increase near ω_{cr} is fitted well by the model III $\gamma(\omega)$ of Eq. (4.14). The two peaks which appear in both theoretical and experimental linewidths represent the increased damping when either the incident or scattered polariton frequency coincides with the frequency of the strongest mixing, ω_{cr}.

Using the parameters determined from the Stokes spectra [given in Eqs. (4.5), (4.7) and (4.15)], the anti-Stokes linewidth was calculated for the three models for $\gamma(\omega)$ discussed above. The calculated linewidths are shown by the solid curves in Figs. 4.4(a), (b) and (c). Again, the frequency independent damping constant γ_0 of model I [Eq.(4.5)] or the $\gamma(\omega)$ of model II [Eqs. (4.6) and (4.7)] give poor fits to the data while model III [Eqs. (4.14) and (4.15)] agrees reasonably well with the measured linewidth.

4.3. Discussion and Conclusions

1. Lifetime of Polaritons

The damping constants $\gamma(\omega)$ found from fitting the RBS linewidth data to models I, II and III are plotted in Fig. 4.5. Let us compare these results to polariton lifetimes obtained from luminescence experiments. In their luminescence experiment, Wiesner and Heim excited polaritons with a picosecond laser pulse at 457.9 nm (21,839 cm^{-1}) which was well above ω_T, and measured the exponential decay of the luminescence at various energies.[7] Their result, reproduced in Fig. 4.6(b), shows that in the vicinity of ω_T, τ_{lum} increases with decreasing frequency from almost zero (less than the experimental resolution of 0.3 ns) up to about 3 ns for observation frequencies below ω_T . This increase of τ_{lum} has been attributed to the onset of the bottleneck effect in polariton decay.

Sumi made a numerical evaluation of the polariton lifetime to explain the intensity ratio of zero-phonon and one-LO-phonon luminescence.[17] His result implies that $\tau \approx 10^{-9}$ to 10^{-10} seconds with a maximum of about 1 ns at frequencies several cm^{-1} below $\tilde{\omega}_T$.

In contrast to the long lifetimes measured by luminescence, $\tau(\omega) = 2/\gamma(\omega)$ determined from the present RBS experiments, as shown in Fig. 4.6(a), is about two orders of magnitude shorter.[18] The experimental linewidth of RBS in GaAs has been reported[1] to increase from about 0.02 cm^{-1} to 0.3 cm^{-1} which is similar to our results for CdS.

The difference between τ_{lum} and τ_{RBS} could be attributed in part to the fact that τ_{RBS} is the lifetime of a polariton created directly at a specific ω and **k**, while τ_{lum} is a <u>net</u> lifetime determined by the balance between polaritons entering and leaving a particular energy range. Thus, τ_{lum} includes the sum of the contributions of all decay paths which produce polaritons in states with a given ω. Another important difference between RBS and luminescence lifetimes is that a polariton that undergoes elastic scattering which changes the direction of **k** without changing ω can still contribute to luminescence, but <u>not</u> to RBS. In RBS, the initial and final states are specified and any polariton scattering processes, including elastic scattering from defects, internal stress etc., reduce the RBS lifetime.

Recently, Askary and Yu measured CdS luminescence by a method similar to that of Wiesner and Heim and found that there are two lifetimes, τ_{fast} and τ_{slow}.[19] However, their τ_{fast} is still several tenths of a nanosecond and is much longer than τ_{RBS} . When the elastic scattering rate [the second term in Eq. (4.14)] is dominant, i.e. when relaxation between states of the same energy occurs much faster than other relaxation processes, τ_{RBS} can be much shorter than τ_{lum}. However, our result [Eq. (4.15)] for $\gamma(\omega)$ indicates that processes other than elastic scattering also contribute significantly to τ_{RBS}. Therefore, the origin of the large difference between τ_{RBS} and τ_{lum} is not yet clear.

In spite of the difference in magnitude between the two lifetimes, τ_{RBS} also shows an increase of lifetime with decreasing ω near ω_T corresponding to the onset of the bottleneck effect for lower branch polaritons due to the rapid change in the density of states. It should be noted that in luminescence experiments the lifetime is too short to be measured for frequencies $\omega > \omega_T$, while RBS line broadening is measurable in the region between ω_T and ω_L , which is important for the ABC problem.

2. Linewidth Expression in RBS

So far we have assumed that the RBS linewidth is given by Eq. (1.29) with k determined by Eq. (1.13). Dervisch and Loudon have shown that if phonon reflection at the crystal surface is taken into account, the lineshape of RBS cannot be a simple Lorentzian and should be a skewed Lorentzian instead.[20] According to their result and its extension by Tilley to the case of RBS via exciton polaritons,[21] the linewidth is still given by Eq. (1.29) if the interference between scattering involving different polariton branches can be ignored. Since the LA 2-2' peak is well isolated from other components and no lineshape distortion was observed, we believe that the linewidth formula Eq. (1.29) can still be used for this case.

In Eq. (1.25), we have also neglected the frequency dependence of the transmissivity $T(\omega)$ when we calculate the linewidth. Actually, $T(\omega)$ changes considerably between ω_T and ω_L depending on the ABC. However, numerical evaluation[10] for different ABCs shows that a change of 50% in $T(\omega)$ occurs over a frequency range of at least 5 cm^{-1} which is much larger than the typical Brillouin linewidth (less than 0.5 cm^{-1}). Therefore the frequency-dependence of the transmissivity and the ABC which determines it have little effect on the RBS linewidth.

3. Wavevector-Induced Mixing of Exciton States

For $\mathbf{k}$ = (k, 0, 0), wavevector-induced mixing involving A and B-excitons in CdS can occur in the following cases:[22] (i) between A and B-excitons, $\Gamma_{5L}(A)$ and $\Gamma_1(B)$ (where L means longitudinal) as suggested by Hopfield and Thomas,[23] or $\Gamma_6(A)$ and $\Gamma_5(B)$; (ii) among different B-exciton states, $\Gamma_{5T}(B)$ and $\Gamma_2(B)$, or $\Gamma_{5L}(B)$ and $\Gamma_1(B)$ which was treated by Mahan and Hopfield;[16] (iii) among the A-exciton states, $\Gamma_{5T}(A)$ and $\Gamma_6(A)$, or $\Gamma_{5L}(A)$ and $\Gamma_6(A)$. The effect we have considered in section 4.2 corresponds to case (iii). Although this case was suggested as a possible explanation for magneto-luminescence observations in the configuration **E** ⊥ **c** and **H** || **c**,[24] no explicit evidence for k-linear interaction among the A-exciton states has been reported before the present work.

Our result for the k-linear coefficient of the A-exciton in CdS agrees reasonably well with the value determined from the literature. Recent spin-flip Raman scattering experiments by Romestain et al[25] gave the k-linear coefficient of the Γ_7 conduction band as C_e = 1.6×10^{-10} eV cm, while the Γ_9 symmetry of the valence band requires that its k-linear coefficient vanishes, i.e. $C_{hA} = 0$. Thus the k-linear coefficient of the A-exciton is given by [see Eq. (4.4)]

$$\phi_A = (C_{hA} m_{h\perp}^A - C_e m_{e\perp})/(m_{h\perp}^A + m_{e\perp}) \qquad (4.16)$$

Using $m_{e\perp} = 0.21\ m_0$, $m_{h\perp}^A = 0.70\ m_0$, we obtain

$$|\phi_A| = 3.6 \times 10^{-11} \text{ eV cm.} \qquad (4.17)$$

which agrees within a factor of two with our experimental result

$$|\phi_A| = \hbar e = (1.9 \pm 0.2) \times 10^{-11} \text{ eV cm.} \qquad (4.18)$$

It should be noted that the k-linear effect for the A-exciton is about 30 times weaker than that for the B-exciton[15] and corresponds to an effective magnetic field of only 3.6 kG. This is too small to cause any observable splitting of exciton levels or reflectivity anomalies under our present experimental conditions. However, it is big enough to cause significant line broadening of the Brillouin components in the vicinity of ω_{cr}.

In conclusion, we have shown that the RBS linewidth measurement implies that the phenomenological damping constant $\gamma(\omega)$ depends on frequency in a rather complicated way, as given in Eqs. (4.14) and (4.15). In order to explain the sharp increase of the linewidth above the exciton resonance frequency ω_T , the decay of $\Gamma_{5T}(A)$ polaritons to $\Gamma_6(A)$ exciton states via the wavevector-induced interaction has been proposed.

References

1. C. Weisbuch and R. G. Ulbrich, in: Proceedings of the International Conference on Lattice Dynamics, Paris 1977, edited by M. Balkanski (Flammarion, Paris, 1978) p.167.

2. C. Hermann and P. Y. Yu, Solid State Commun. **28**, 313 (1978).

3. J. Wicksted, M. Matsushita, H. Z. Cummins, T. Shigenari, and X. Z. Lu, Phys. Rev. B**29**, 3350 (1984).

4. J. Wicksted, M. Matsushita and H. Z. Cummins, Solid State Commun. **38**, 777 (1981).

5. Y. Toyozawa, Progr. Theor. Phys., Suppl. **12**, 111 (1959).

6. C. Benoit a la Guillaume, A. Bonnot and J. M. Deberer, Phys. Rev. Lett. **24**, 1235 (1970).

7. P. Wiesner and U. Heim, Phys. Rev. B**11**, 3071 (1975).

8. See the review artical by P. Y. Yu, in: Light Scattering in Solids, edited by J. L. Birman, H. Z. Cummins and K. K. Rabane (Plenum Press, New York, 1979).

9. J. J. Hopfield and D. G. Thomas, Phys. Rev. **132**, 563 (1963).

10. M. Matsushita, J. Wicksted and H. Z. Cummins, Phys. Rev. B**29**, 3362 (1984).

11. P. Y. Yu and Y. R. Shen, Phys. Rev. B**12**, 1377 (1975).

12. E. J. Flynn and S. Geschwind, Bull. Am. Phys. Soc. **26**, 488 (1981).

13. J. J. Hopfield, Journal of Applied Physics, suppl. to vol. **32**, 2277 (1961).

14. R. C. Casella, Phys. Rev. Lett. **5**, 371 (1960); Phys. Rev. **114**, 1514 (1959).

15. E. S. Koteles and G. Winterling, Phys. Rev. Lett. **44**, 948 (1980).

16. G. D. Mahan and J. J. Hopfield, Phys. Rev. **135**, A428 (1964).

17. H. Sumi, Solid State Commun. **17**, 701 (1975); J. Phys. Soc. Jpn. **41**, 526 (1976).

18. Generally speaking, the lifetime depends on the quality of the sample. However, Yu (in private communication) has measured the luminescence from a sample with the same origin as ours and found lifetime of a few ns, similar to the value of Wiesner and Heim (Ref. 7).

19. F. Askary and P. Y. Yu, Phys. Rev. B**28**, 6165 (1983).

20. A. Dervisch and R. Loudon, J. Phys. C: Solid State Phys. **9**, L669 (1976).

21. D. R. Tilley, J. Phys. C: Solid State Phys. **13**, 781 (1980).

22. K. Cho, Phys. Rev. B**14**, 4463 (1976).

23. J. J. Hopfield and D. G. Thomas, Phys. Rev. **122**, 35 (1961).

24. H. Venghaus, S. Suga and K. Cho, Phys. Rev. B**16**, 4419 (1977).

25. R. Romestain, S. Geschwind and G. E. Devlin, Phys. Rev. Lett. **39**, 1583 (1977).

Chapter 5. RBS Linewidth in a Weak Magnetic Field: Direct Evidence for the k-Linear Effect in the A-Exciton of CdS

The purpose of the experiment presented in this chapter was to further test our model for the frequency-dependent exciton-polariton damping given in Chapter 4 and to give direct evidence for the k-linear effect of the A-exciton in CdS.

5.1. Theory

1. Equivalence of k_x and B_y:

From Table 2.1, we see that the k-linear term for an electron (or exciton) moving along the x-direction is equivalent to a magnetic field along the y-direction. A simple perturbation derivation can reach the same conclusion. Consider an electron with **k** = (k,0,0), for example. We obtain its wavefunction by solving the Schröedinger Equation $H\Psi = E\Psi$ with H given by Eq. (4.3):

$$\Psi = 2^{-1/2} \left[|\alpha\rangle \pm (ik/|k|)\, |\beta\rangle \right] , \tag{5.1}$$

where $|\alpha\rangle$, $|\beta\rangle$ represent the spin-up and spin-down states, respectively. Suppose one applies an external magnetic field **B** = $(0,B_y,0)$

the energy shifts will be

$$\begin{aligned}\Delta\varepsilon_\pm &= \langle\psi_\pm|\ 2\mu_0(S\cdot B)/\hbar\ |\Psi_\pm\rangle \\ &= \mu_0 B_y \langle\Psi_\pm|\ \sigma_y\ |\Psi_\pm\rangle \\ &= \pm\,\mu_0 B_y k/|k|\ ,\end{aligned} \tag{5.2}$$

if we choose B_y to meet the condition

$$\Delta\varepsilon_\pm \pm C|k| = 0$$

i.e.

$$\mu_0 B_y = - Ck\ , \tag{5.3}$$

then the additional energy terms due to the k-linear interaction and the external magnetic field will cancel each other. Note that the former is the interaction between the electron spin and an effective magnetic field due to the crystal field seen by the moving electron, and the latter is the interaction between the electron spin and the external magnetic field.

2. RBS linewidth in a weak magnetic field

Suppose the wavevector of the incident polaritons is along the x-direction and that of scattered polaritons along the -x-direction, and an external magnetic field B_y is applied in the y-direction, as shown in Fig. 5.1(a). Based upon the equivalence between B_y and k_x, we may derive the polariton dispersion equation from Eq. (4.9) with (ek) replaced by $(ek + \mu B_y)$, i.e.

$$\begin{array}{c} \begin{array}{ccc} |\Gamma_{5T}(A)\rangle & |\Gamma_6(A)\rangle & |\text{photon}\rangle \end{array} \\ \left| \begin{array}{ccc} \omega_T + B_5 k^2 - i\gamma/2 - \omega & -i(ek+\mu B_y) & (2\pi\alpha_0\omega_T)^{1/2} \\ i(ek+\mu B_y) & \omega_6 + B_6 k^2 - i\gamma_6/2 - \omega & 0 \\ (2\pi\alpha_0\omega_T)^{1/2} & 0 & -\varepsilon_b + k^2c^2/\omega^2 \end{array} \right| = 0 \, . \end{array} \qquad (5.4)$$

It is clear that a positive B_y will enhance the k-linear mixing of incident polaritons ($k > 0$) and cancel that of scattered polaritons ($k < 0$), thus the polariton dispersion curve becomes <u>asymmetric</u>, as illustrated in Fig. 5.1(a) for $B_y = +\ 4.8$ kG. The calculated polariton dispersion curve for $B_y = -\ 4.8$ kG will be the mirror image of the curve in Fig. 5.1(a), as shown in Fig. 5.1(b). Following the same procedure as in Chapter 4, we obtain the exciton-polariton damping in the presence of a magnetic field:

$$\gamma = \gamma_0 + \gamma_1 \left[\frac{k'(\omega)}{k_0}\right]^2 \left[\frac{V_{G0}}{V_G(\omega)}\right] + \gamma_2 \frac{\left|ek(\omega) + \mu B_y\right|^2}{\delta E(\omega)^2 + \left|ek(\omega) + \mu B_y\right|^2} \, . \qquad (5.5)$$

Fig. 5.2(a), (b), and (c) show the calculated damping constants for incident polaritons (solid lines) and scattered polaritons (broken lines) vs. incident laser frequency for $B_y = +\ 4.8$ kG, $-\ 4.8$ kG and 0, respectively. Using Eqs. (5.5), (1.13), and (1.29) we can calculate the RBS linewidth in the presence of a magnetic field B_y. Fig. 5.3 shows the calculated Stokes LA 2-2' linewidths vs. incident laser frequency for $B_y = +\ 4.8$ kG (solid line), $B_y = -\ 4.8$ kG (broken line), and $B_y = 0$ (dotted line). The main new feature of Fig. 5.3 is the cut-off of the maximum of the linewidth at $\tilde{\omega}_{cr}$ (20594.0 cm^{-1}) for B_y = - 4.8 kG and at 20601 cm^{-1} for B_y = + 4.8 kG.

In the region of $\omega_I \approx \omega_{cr}$, the third term in Eq. (5.5) dominates and the damping constant depends critically on how far the frequency is from ω_{cr}. Since the scattered frequency $\tilde{\omega}_S$ is about 5 cm^{-1} below $\tilde{\omega}_{cr}$ in the Stokes LA 2-2' scattering events, the main contribution to the RBS linewidth will come from the incident polariton damping γ_I which is greatly reduced in the case of B_y = - 4.8 kG. We should be able to observe line narrowing for B_y = - 4.8 kG (compared to the case of B_y = 0) at $\omega_I \approx \omega_{cr}$.

5.2. Experiment

The experimental configuration was the same as that shown in Fig. 3.1 except for the additional use of a magnet. The Kr-laser-pumped single-mode cw dye laser (Coumarin 102 dye) provided the incident light of 8mW power with both **E** and **k** perpendicular to the crystal c-axis. Backscattered light was collected and analyzed by the triple-pass Fabry-Perot interferometer followed by the double grating spectrometer. The free spectral ranges (FSR) used were 6.5 cm^{-1} and 4.0 cm^{-1} which gave resolutions of about 0.1 cm^{-1} and 0.06 cm^{-1}, respectively.

The sample used in this experiment was numbered CdS 21J. We found that sample quality was quite different for samples even from the same source. The crystals which gave weaker and broader RBS signals and/or stronger luminescence were considered of poorer quality. Good quality samples also deteriorate after long-term laser illumination and/or many temperature cycles. Contamination of the sample surface also affects RBS linewidth and intensity. Thus selection of a good quality sample and thorough cleaning of the sample surface were critical for our experiment. Our crystals were immersed in Toluene and placed in an ultrasonic cleaner which gave reproducible RBS linewidth data. In the absence of magnetic fields, our crystal CdS 21J showed RBS linewidth behavior similar to the crystal CdS 21E-2 in Chapter 4 for both geometries shown in Fig. 5.4(a) and (c).

The sample was attached to the cold finger of the Cryotip liquid-helium cryostat (AIR PRODUCT AND CHEMICALS, model LT-3-110) which gives T ~ 12 K. The Cryotip was mounted in the center of a 13 kG electromagnet (MAGNION, model L-128A, 12 inch). To avoid mechanical drift due to the magnetic field, it was crucial to eliminate magnetic materials inside the cryostat system. To obtain the scattering geometry with $B_y < 0$, we turned the crystal upside down as shown in Fig. 5.4, instead of reversing the direction of the magnetic field which is technically difficult.

We have measured Stokes LA 2-2' linewidths for $B_y = 0, \pm 4.8$ kG, and ± 9.6 kG. The observed Brillouin shifts were independent of the applied magnetic fields and agreed well with our previous data,[1] no Zeeman shifts being observed due to the relative weakness of the magnetic field. However, Brillouin linewidths for different magnetic fields showed very different behaviors in the region around ω_{cr}.

Fig. 5.5(a), (b) show zero-field Stokes LA 2-2' linewidths vs. incident laser frequency for two different geometries as shown in Fig. 5.4(a) and (c), respectively. Due to the symmetric structure of the polariton dispersion curves for $k > 0$ and $k < 0$, both geometries showed the same linewidth behavior, as expected.

Fig. 5.6(a), (b) show the observed Stokes LA 2-2' linewidths vs. incident laser frequency for $B_y = \pm 4.8$ kG, respectively. Significant differences in the region around ω_{cr} were observed clearly and repeatedly which agreed with our theoretical prediction. Both line narrowing for $B_y = - 4.8$ kG and broadening for $B_y = + 4.8$ kG were observed due to the cancellation or enhancement of the k-linear mixing by external magnetic fields as shown in Fig. 5.7 for $\tilde{\omega}_I = 20592.0$ cm^{-1}. At the higher frequencies $\tilde{\omega}_I > 20598$ cm^{-1}, the repeatability became poor and the data were severely scattered. Similar features were observed for Stokes TA 2-2' linewidths, as shown in Fig. 5.8(a) and (b), although not as clearly as with the LA-component.

Figs. 5.9(a) and (b) show the observed Stokes LA 2-2' linewidths for $B_y = \pm 9.6$ kG, respectively. When $\omega_I \approx \omega_{cr}$ and $B_y > 0$, the lower and middle branches of the incident polariton have comparable oscillator strengths. However, since the frequency of the scattered polaritons is about 5 cm^{-1} below $\tilde{\omega}_{cr}$ in the Stokes LA 2-2' scattering events, only the lower branch of the scattered polaritons has significant oscillator strength. Thus when B_y is sufficiently large to cause the separation between the lower and the middle branches of the incident polaritons to be resolvable, a double peak should be observed, one due to Stokes LA scattering from the incident middle branch to the scattered lower branch and the second from the incident lower to the scattered lower branch. We did observe this line splitting around ω_{cr} for B_y = + 9.6 kG, as shown in Fig. 5.10. As ω_I is increased through ω_{cr}, the relative oscillator strength of the lower branch to the middle branch of the incident polaritons will decrease, and correspondingly the intensity ratio of the peak at the lower frequency side to that at the higher frequency side should also decrease. Again this is what we observe, as shown in Fig. 5.10. When B_y = - 9.6 kG, once again, line narrowing was observed around ω_{cr} as seen by comparing Fig. 5.5(b) and Fig. 5.9(b).

5.3. Discussion and Conclusions

According to Eq. (5.5), it is the combined effect of the k-linear interaction and the external magnetic field which dominates the RBS linewidth in the region around ω_{cr} via the third term in Eq. (5.5). If the k-linear effect were absent, the RBS linewidth would show the same behavior for magnetic fields of the same magnitude and opposite directions; the existence of the k-linear interaction (as well as the crystal field in CdS) makes the ± c directions of the crystal inequivalent. The large differences between Fig. 5.6(a) and (b) clearly demonstrate the existence of the k-linear interaction in the A-exciton states in CdS.

To estimate the k-linear coefficient of the A-exciton in CdS from our present experiment, we notice that Fig. 5.6(b) (B_y = - 4.8 kG) and Fig. 5.9(b) (B_y = - 9.6 kG) show the same narrowed linewidths around ω_{cr}, i.e. the net mixing effect due to the cancellation of the k-linear interaction by the external magnetic fields have the same magnitude in both cases which suggests that a reasonable value for the effective magnetic field of the k-linear effect in the A-exciton of CdS is about 7.2 kG, from which we find

$$|\phi_A| \approx (3.8 \pm 0.4) \times 10^{-11} \text{ eV cm}. \qquad (5.6)$$

which is twice as large as the value we deduced from our analysis of the zero-field RBS linewidth [Eq. (4.18)].[2] A more accurate determination of ϕ_A will be presented in the next chapter.

The splitting of the Stokes LA 2-2' component around ω_{cr} in a magnetic field of B_y = + 9.6 kG further verified the k-linear effect of the A-exciton in CdS. This splitting ranges from 0.1 to 0.3 cm^{-1} when B_y = + 9.6 kG, which could be used to determine some important parameters of the A-exciton in CdS quantitatively.

In conclusion, we have shown that our model for the exciton-polariton damping constant in the A-exciton region of CdS, as given by Eqs. (4.14) and (4.15), can explain RBS linewidths for different magnetic fields quantitatively. In particular, we have given the first direct evidence for the existence of the k-linear interaction of the A-exciton in CdS. Our model is valid only for weak coupling cases as seen from the perturbation calculations we performed.

References

1. J. Wicksted, M. Matsushita, H. Z. Cummins, T. Shigenari, and X. Z. Lu, Phys. Rev. B29, 3350 (1984).

2. T. Shigenari, X. Z. Lu, and H. Z. Cummins, Phys. Rev. B30, 1962 (1984).

Chapter 6. RBS Experiment at Superfluid-Helium-Temperature: Direct Observation of Three-Branch Polariton Dispersion in the A-Exciton of CdS

All the RBS experiments in the 1s A-exciton of CdS reported so far were well interpreted using a two-branch exciton-polariton model. In Chapter 5, however, we gave direct evidence for the existence of the k-linear interaction among the 1s A-exciton states and showed that RBS line-splitting could be observed if this interaction was properly enhanced by an external magnetic field comparable to it in magnitude. This fact reveals the possibility of directly observing three-branch polariton behavior in the A-exciton of CdS by further improving the instrumental resolution in our RBS experiment.

On the other hand, the exciton-polariton lifetime deduced from our RBS linewidth measurement at liquid-helium-temperature in CdS was about two orders of magnitude shorter than that obtained from luminescence experiment at T = 1.6 K.[1] Moreover, in a preliminary RBS experiment in CdS, Flynn and Geschwind[2] reported that Brillouin linewidths were much narrower if the samples were immersed in a helium bath at T = 1.4 K. The discrepency between our result and Refs. 1 and 2 strongly suggested, besides the other possible reasons, significant temperature-dependence of exciton-polariton lifetime at low-temperatures. Performing RBS at superfluid-helium-temperatures may help to reduce RBS linewidth and resolve the expected three-branch polariton behavior in the A-exciton of CdS. The main motivation of the present research was to verify the temperature-dependence of polariton lifetime and directly observe three-branch polariton dispersion in the A-exciton of CdS.

6.1. Theory

Wannier excitons in semiconductors - mobile excitations formed from a conduction electron and a valence hole - are represented ideally by simple parabolic dispersion curves. In practice, however, their dispersion curves are much more complex due to interactions between excitons as well as between excitons and other excitations such as photons. In Fig. 6.1 these interactions are illustrated schematically for the A-exciton in CdS. In Fig. 6.1(a), the coupling of the dipole-allowed Γ_{5T} exciton and the photon produces a two-branch exciton-polariton. In Fig. 6.1(b), the k-linear interaction between the Γ_{5T} exciton and the dipole-forbidden Γ_6 spin-triplet exciton produces mixing and level shift. In Fig. 6.1(c), both interactions are included simultaneously, leading to a three-branch dispersion curve.

The A-exciton series in CdS is formed by the Coulomb-coupling of an electron in the lowest conduction band Γ_7 for which symmetry allows a k-linear term in the energy of the form $C_e k_{e\perp}$, and a hole in the top valence band Γ_9 for which a k-linear term is symmetry-forbidden. For **k** $\perp$ **c** and in the limit **k** = 0, the four 1s A-exciton states are characterized by the symmetries Γ_{5T}, Γ_{5L}, Γ_6, and Γ_6 in which only Γ_{5T} is dipole-active for **E** $\perp$ **c**. The k-linear term $C_e k_{e\perp}$ in the conduction band electron energy leads to the k-linear term $\phi_A k_\perp$ in the A-exciton energy via Eq. (4.16) with $C_{hA} = 0$ due to the Γ_9 symmetry of the top valence band in CdS.

From symmetry considerations[3] the k-linear interaction may mix Γ_{5T} and Γ_6 states at finite **k**. The oscillator strength will be transferred from the dipole-allowed state Γ_{5T} to the dipole-forbidden state Γ_6. The polariton dispersion resulting from the two hybrid dipole-active exciton states will be given by

$$\begin{array}{ccc} |\Gamma_{5T}(A)\rangle & |\Gamma_6(A)\rangle & |\mathrm{photon}\rangle \\ \left| \begin{array}{c} \omega_T + B_5 k^2 - i\gamma/2 - \omega \\ iek \\ (2\pi\alpha_0\omega_T)^{1/2} \end{array} \right. & \begin{array}{c} -iek \\ \omega_6 + B_6 k^2 - i\gamma_6/2 - \omega \\ 0 \end{array} & \left. \begin{array}{c} (2\pi\alpha_0\omega_T)^{1/2} \\ 0 \\ -\varepsilon_b + k^2c^2/\omega^2 \end{array} \right| \end{array} = 0 , \qquad (6.1)$$

where $e = \phi_A/\hbar$, $B_5 = \hbar/(2M)$, $B_6 = \hbar/(2M_6)$, $\omega_6 = \omega_T - \Delta_{st}$, M_6 and γ_6 are the exciton effective mass and damping constant of the Γ_6 state, Δ_{st} is the frequency difference between Γ_5 and Γ_6 states at **k** = 0. Fig. 6.1(c) shows the calculated three-branch polariton dispersion curves of the A-exciton in CdS at T = 1.9 k due to the k-linear mixing between Γ_{5T} and Γ_6 exciton states using $\tilde{\omega}_T$ = 20591.0 cm^{-1}, ϕ_A

$= 2.7 \times 10^{-11}$ eV cm, determined from the present experiment as described below. The remaining parameters were directly taken from our previous experiments, as given in Table 1.2. The resulting three-branch behavior, shown in Fig. 6.1(c), implies that an incident photon at a frequency above ω_L can create three propagating modes in the crystal with the same frequency but different wavevectors. Thus in place of a single Brillouin component (which becomes four components in the two-branch polariton picture of Fig. 6.1(a)), a maximum of nine Brillouin components can arise from all inter- and intra-branch scattering processes. In particular, a 2-2' Brillouin component in the two-branch picture of Fig. 6.1(a) can split into 4 components in the three-branch picture of Fig. 6.1(c).

Since the k-linear interaction in the A-exciton is relatively weak, we could approximate the content of Eq. (6.1) as coupling between the Γ_{5T} exciton and the photon producing the two-branch polariton shown in Fig. 6.1(a), followed by coupling between the Γ_6 exciton state (which is $\tilde{\Delta}_{st} = 1.6$ cm^{-1} below Γ_{5T} state) and the lower branch $\Gamma_{5\ell}$ of the Γ_{5T} polaritons producing the three-branch polariton of Fig. 6.1(c). The k-linear mixing, as well as the oscillator strength transfer, will only be significant in the vicinity of the crossing point ($\tilde{\omega}_{cr} = 20596.2$ cm^{-1} for T = 1.9 K) where these two excitations would be degenerate in the absence of the k-linear term. Most polaritons are created on the middle branch for $\omega > \omega_{cr}$ and on the lower branch for $\omega < \omega_{cr}$. Around ω_{cr}, both branches have comparable oscillator strengths. Thus, three-branch behavior will be most likely observed in RBS when ω_I and/or ω_S fall in the vicinity of ω_{cr}.

6.2. Experiment

The experimental configuration was the same as that shown in Fig. 3.1. A Kr-laser-pumped single-mode cw dye laser (coumarin 102 dye) provided the incident light of 8 mW power with both **E** and **k** perpendicular to the crystal c-axis. Backscattered light was collected and analyzed by a triple-pass Fabry-Perot interferometer followed by a double-grating spectrometer. The free spectral range (FSR) of the interferometer employed was only 1.0 cm^{-1} which gave a very high resolution of about 0.015 cm^{-1}.

The sample used in this experiment was a vapor-grown single-crystal platelet (numbered 21N) obtained from the same source (General Motors) and giving the similar RBS spectra at liquid-helium-temperature as those used in Chapters 4 and 5.

The sample was mounted in a liquid-helium dewar (JANIS, model DT) equipped with a carbon-glass temperature sensor (LAKE SHORE, model CGR-1-1000, working current 10 μA, temperature calibration range 1.4 - 20 K). In order to obtain superfluid-helium-temperatures (below T_λ = 2.17 K), we used a mechanical pump (WELCH, model 1397, pumping speed 425 liters/min.) to continuously evacuate the sample space of the dewar. We first opened the needle valve fully to let liquid helium flow into the sample space from the helium reservoir, then shut the needle valve partially to obtain the lowest superfluid temperature in our experiment (~ 1.75 K). The temperature in the sample space was then controlled by gradually opening up the needle valve. We chose our working temperature T = 1.9 K as a compromise between continuous operation without refilling the sample space and maintaining a stable superfluid state. The helium consumption was about 2 liters per hour, doubles that required for maintaining normal liquid-helium-temperature (4.2 K). When the superfluid-helium-temperatures were reached, the bubbles in the liquid would suddenly disappeared and the liquid-helium became completely transparent (refractive index n = 1) which allowed performance of light scattering with samples immersed in the helium bath. To reduce vibrations caused by the big pump, it was crucial to mechanically fix the entire dewar and pump system rigidly. An exhaust filter was needed to eliminate oil vapor produced by the pump operating continuously at high throughput.

The measured Brillouin shift of the Stokes LA and TA 2-2' components in the two-branch polariton model is shown by the solid dots in Fig. 6.2. The solid lines were calculated using the values given above. The excellent agreement between them shows that the exciton parameters ϵ_b, $4\pi\alpha_o$, and M are insensitive to temperature while $\tilde{\omega}_T$ is about 2.2 cm^{-1} higher than that at T = 4.2 K.

When ω_I was increased from below ω_T, both Stokes LA 2-2' and TA 2-2' components underwent resonant enhancement and line-broadening, as was previously observed at liquid-helium-temperature. However, as ω_I approached ω_{cr} , each Stokes 2-2' components split into two peaks ($LA \rightarrow L_\alpha + L_\beta$, $TA \rightarrow T_\alpha + T_\beta$), where L_α (or T_α) is due to Stokes scattering from lower branch to lower branch (3-3'), and L_β (or T_β) from middle branch to lower branch (2-3'). The spectra are shown in Fig. 6.3 while the splitting is shown schematically in the inset of Fig. 6.2. Note that the k-linear mixing occurs only near ω_{cr} and the Brillouin shift in this region is relatively large (greater than 2 cm^{-1} for Stokes LA and TA 2-2' components). Therefore ω_I and ω_S cannot fall in the region of significant mixing simultaneously, so we only observed double peaks rather than the quadruple peaks allowed by theory. This splitting is only observed in the narrow region of frequencies near ω_{cr} where both branches 2 and 3 have significant oscillator strength.

As ω_I is increased through ω_{cr}, the relative oscillator strength of the lower branch to the middle one of the incident polaritons decreases, and correspondingly the intensity ratio of the peak at the lower frequency side (L_α, T_α) to that at the high frequency side (L_β, T_β) should also decrease, as we see from Fig. 6.3.

The spectral splitting of the Brillouin components is very sensitive to the value of ϕ_A. Fits of the theoretically predicted splitting to our data yielded

$$\phi_A = (2.7 \pm 0.3) \times 10^{-11} \text{ eV cm} . \qquad (6.2)$$

Fig. 6.4 shows the observed Stokes LA and TA 2-2' spectral splitting (solid dots) and the best fit result (solid lines).

Fig. 6.5(a) shows the measured Stokes LA 2-2' linewidth vs. incident laser frequency at T = 1.9 K. The general features of the linewidth curve, including the line-broadening in the resonance region, are similar to those at liquid-helium-temperature reported in Chapter 4. However, the magnitude of the line-broadening is about 10 times smaller than the latter. We have previously proposed that the polariton damping constant $\gamma(\omega)$ should include three contributions: (1) a frequency-independent term γ_0, (2) a frequency-dependent term representing polariton decay via intrabranch elastic scattering, and (3) a term describing the apparent line broadening (unresolved three branch behavior) due to the k-linear interaction. Since we have now resolved the individual Brillouin components in three-branch picture, the third term is no longer necessary. We therefore fit the data in Fig. 5(a) to:

$$\gamma = \gamma_0 + \gamma_1 \left[\frac{k'(\omega)}{k_0}\right]^2 \left[\frac{V_{G0}}{V_G(\omega)}\right] . \qquad (6.3)$$

The best fit, indicated by the solid line, corresponds to:

$$\tilde{\gamma}_0 = (0.029 \pm 0.003)\ \mathrm{cm}^{-1}$$

$$\tilde{\gamma}_1 = (0.012 \pm 0.001)\ \mathrm{cm}^{-1} . \qquad (6.4)$$

The frequency-dependent polariton damping constant $\gamma(\omega)$ of Eqs. (6.3) and (6.4) is plotted in Fig. 6.5(b).

6.3. Discussion and Conclusions

The k-linear coefficient ϕ_A, as given in Eq. (6.2), is the first accurately measured value and agrees with our previous results [Eqs. (4.18) and (5.6)] within a factor of 2. Using $m_{e\perp} = 0.2\ m_0$ and $m^A_{h\perp} = 0.7\ m_0$ (see Table 1.2), with $C_{hA} = 0$ in Eq. (4.16), we find $C_e = 4.25\ \phi_A = (1.2 \pm 0.1) \times 10^{-10}$ eV cm, in good agreement with the value 1.6 x 10 $^{-10}$ eV cm found for the conduction band by Romestain et al.[4]

Since the k-linear coefficient of the A-exciton is about 20 times smaller than that of the B-exciton in CdS,[5] the three-branch behavior of the A-exciton-polaritons has the following features: (a) The spectral splitting in the 2-2' RBS events is relatively small (~ 0.1 cm^{-1} for Stokes LA and ~ 0.05 cm^{-1} for Stokes TA component). Three-branch behavior was never observed before due to the limited instrumental resolution available and/or line-broadening due to higher temperatures. (b) k-Linear mixing is significant only in the vicinity of ω_{cr}; double peaks rather than quarduple ones should result for 2-2' Brillouin components when ω_I or ω_S , but never both, falls in the region of significant mixing. The A-exciton-polaritons can essentially be described within the framework of a two-branch model except for a small region of ~ 2 cm^{-1} spectral range around $\tilde{\omega}_{cr}$ where both branches 2 and 3 have significant oscillator strength.

The exciton-polariton lifetime and the RBS linewidth are sensitive to temperature for $T < 20$ K. Difficulties in the RBS linewidth measurement at "liquid-helium-temperature" mainly arise from difficulties in determining the actual temperature of the sample, which may be considerably higher than 4.2 K due to the poor thermal conductivity between sample illuminated area and the temperature sensor, and/or spatial inhomogeneity due to local heating effects by the laser beams (the crystal is highly absorbing in the exciton resonance region!). The measured sample temperature, for instance, ranged from 6 ~ 12 K in our JANIS dewar used in Ref. 5, or from 10 ~ 18 K in our Cryotip used in Chapters 4 and 5. A reasonable estimate of the average temperature corresponding to our previous RBS linewidth data and polariton lifetime results would be ~ 12 K. In our superfluid-helium-temperature experiment with the sample immersed directly in the pumped liquid helium bath, the actual sample temperature was known as T = 1.9 K. Therefore we conclude that exciton-polariton lifetime in CdS increases by about a factor of 10 when the temperature is lowered from 12 K to 1.9 K. This partially explains the discrepency between the polariton lifetimes obtained in our RBS experiments and in Refs. 1 and 2. Other possible reasons may be sample-dependence of the polariton lifetime and inhomogeneous broadening due to laser heating etc. which need to be further clarified.

In conclusion, we have given the first direct evidence for three-branch polariton behavior originating from the k-linear interaction in the A-exciton of CdS, and deduced a value for the coefficient ϕ_A in good agreement with the results of Romestain et al for the coefficient C_e of the conduction band. We have also measured the frequency-dependent polariton damping at 1.9 K and shown that it depends strongly on temperature below 20 K.

References

1. P. Wiesner and U. Heim, Phys. Rev. B**11**, 3071 (1975).

2. E. J. Flynn and S. Geschwind, Bull. Am. Phys. Soc. **26**, 488 (1981).

3. K. Cho, Phys. Rev. B**14**, 4462 (1976).

4. R. Romestain, S. Geschwind and G. E. Delvin, Phys. Rev. Lett. **39**, 1583 (1977).

5. E. S. Koteles and G. Winterling, Phys. Rev. Lett. **44**, 948 (1980).

Chapter 7. Generalized ABC and RBS Intensity in CdS

7.1. Generalized ABC

Following the idea of Nakayama et al[1], we present a generalized version of the ABC including the surface potential (or dead layer) effect. The dead layer was defined as an exciton-free layer at the crystal surface by Hopfield and Thomas in 1963.[2]

1. ABC Imposed on the Asymptotic Excitonic Polarizations and the Scattering length a.

Let $P_e = \sum_i P_i$ represent the sum of the bulk (asymptotic) excitonic polarizations of the internal motion of excitons. The ABC imposed on P_e can be obtained from the scattering behavior of excitons at the crystal surface and written:

$$P_e + a\frac{dP_e}{dx} = 0 \qquad \text{at} \quad x = 0 \; , \tag{7.1}$$

where the parameter a is the scattering length of the asymptotic excitonic polarization at the surface and x is the coordinate whose axis is perpendicular to the surface.

Alternatively, we can rewrite Eq. (7.1) in terms of a complex scattering (or reflection) amplitude S. To do so we assume

$$\mathbf{P}_e \propto [\exp(-ik_{ex}x) + S\exp(ik_{ex}x)]\,\theta(x) \,, \qquad (7.2)$$

where k_{ex} is the x-component of the bare exciton wavevector. From Eq. (1.23) we have

$$k_{ex} = \left[k_e^2 - k_{e||}^2 \right]^{\frac{1}{2}}$$

$$= \left[\frac{\omega^2 - \omega_0^2 + i\omega\gamma}{\frac{\hbar\omega_0}{M}} - k_{||}^2 \right]^{\frac{1}{2}} \,, \qquad (7.3)$$

where $\mathbf{k}_{||}$ represents the components of the wavevectors of bare excitons, photons, or polaritons parallel to the surface at $x = 0$. They are all equivalent due to the phase matching requirement.

Substitution of Eq. (7.2) into Eq. (7.1) yields

$$1 + S - ik_{ex}a + iSk_{ex}a = 0 \,,$$

thus

$$S = \frac{ik_{ex}a - 1}{ik_{ex}a + 1} \qquad (7.4)$$

or

$$a = \frac{i}{k_{ex}} \frac{S + 1}{S - 1} \,. \qquad (7.5)$$

Note that generally both a and S are functions of ω .

2. Evanescent Excitonic Polarization Wave and the Decay Length b.

Due to the surface repulsive potential (intrinsic dead layer effect), exciton wavefunctions must be deformed near the surface. This influence can be approximated as an additional exponentially decaying evanescent polarization wave. Thus the total polarization will be

$$\mathbf{P} = \mathbf{P}_e + \mathbf{A} \exp(- \frac{z}{b}) .$$

Since the total polarization **P** should vanish at x = 0 which implies

$$\mathbf{A} = - P_e(0),$$

thus

$$\mathbf{P} = \mathbf{P}_e - P_e(0) \exp(- \frac{z}{b}) , \qquad (7.6)$$

where the parameter b is the decay length of the evanescent excitonic polarization. It can be considered as an effective dead layer thickness. Therefore the ABC imposed on the total polarization will be obtained from Eqs. (7.1) and (7.6):

$$\mathbf{P} + a \frac{d\mathbf{P}}{dx} = \mathbf{P}_e(0) \left(\frac{a}{b} - 1\right) \quad \text{at} \quad x = 0 . \qquad (7.7)$$

3. Generalized ABC

In order to use ABCs directly in calculations, one should find the corresponding conditions imposed on the electric fields associated with exciton polarizations. The Maxwell equations

$$\nabla \times \mathbf{E} = - \frac{1}{c} \frac{\partial \mathbf{B}}{\partial t}$$

$$\nabla \times \mathbf{H} = \frac{1}{c} \frac{\partial \mathbf{D}}{\partial t}$$

together with

$$\mathbf{D} = \varepsilon_b \mathbf{E} + 4\pi \mathbf{P}$$

$$\mathbf{B} = \mathbf{H}$$

give

$$\frac{\varepsilon_b}{c^2}\frac{\partial^2 \mathbf{E}}{\partial t^2} + \nabla \times (\nabla \times \mathbf{E}) + \frac{4\pi}{c^2}\frac{\partial^2 \mathbf{P}}{\partial t^2} = 0 \ . \tag{7.8}$$

If we neglect the common factor $\exp(i\mathbf{k}_{||}\cdot\mathbf{r}_{||} - i\omega t)$ for all the field quantities and show explicitly only the x-dependence, the constituent equation can be written:

$$\mathbf{P}(x) = \int_0^\infty dx' \, \chi_s(x,x') \, \mathbf{E}(x') \ , \tag{7.9}$$

where $\chi_s(x,x')$ is the excitonic susceptibility which can be derived from the surface behavior of excitonic polarization given by Eqs. (7.1), (7.5), and (7.6). Therefore Eqs. (7.8) and (7.9) can be solved for self-consistent solutions of **E** and **P** after some algebra:

$$\mathbf{E}(x) = \sum_{i=1,2,L} \mathbf{E}_i \exp(ik_{ix}x) + \mathbf{E}_{ev} \exp(-\frac{x}{b}) \tag{7.10}$$

$$\mathbf{P}(x) = \sum_{i=1,2,L} \chi_i \mathbf{E}_i \exp(ik_{ix}x) + \mathbf{P}_{ev} \exp(-\frac{x}{b}), \tag{7.11}$$

and the relation among $\mathbf{E}_i$ and $\mathbf{E}_{ev}$ are

$$\sum_{i=1,2,L} f(k_{ix}) \mathbf{E}_i + f(ib^{-1}) \mathbf{E}_{ev} = 0 \tag{7.12}$$

$$\frac{\varepsilon_b \omega^2}{c^2} \mathbf{E}_{ev} + \mathbf{k}_{ev} \times (\mathbf{k}_{ev} \times \mathbf{E}_{ev}) - \frac{4\pi\omega^2}{c^2} \sum_{i=1,2,L} \chi(\omega,k_i) \mathbf{E}_i = 0 \ . \tag{7.13}$$

Eqs. (7.12) and (7.13) serve as a generalized ABC, where i = 1, 2, and L for upper branch polariton, lower branch polariton, and longitudinal exciton modes respectively, $\mathbf{k}_i$ is the wavevector of the i'th mode, but for the evanescent wave

$$\mathbf{k}_{ev} = (\mathbf{k}_{||}, ib^{-1}), \tag{7.14}$$

and

$$\chi(\omega,k_i) = \frac{\alpha_0\omega_0^2}{\omega_0^2 + \frac{\hbar\omega_0}{M}k_i^2 - \omega^2 - i\omega\gamma}$$

$$= \frac{c^2k_i^2}{4\pi\omega^2} - \frac{\varepsilon_b}{4\pi}, \tag{7.15}$$

but for the longitudinal mode

$$\chi(\omega,k_L) = -\frac{\varepsilon_b}{4\pi} \tag{7.16}$$

and

$$f(q) = \alpha_0\omega_0^2\,\frac{M}{\hbar\omega_0}\left[\frac{1}{q^2 - k_{ex}^2} + \frac{1+S}{2k_{ex}}\left(\frac{1}{q+k_{ex}} - \frac{1}{q+ib^{-1}}\right)\right]. \tag{7.17}$$

4. Generalized ABC in Normal Incidence Case

In the normal incidence case, all **E**'s are parallel and assumed to be along the y-direction, all **k**'s are parallel and along the x-direction, and $\mathbf{E}_L = 0$. Thus Eqs. (7.12) and (7.13) are reduced to

$$f(k_1)E_1 + f(k_2)E_2 + f(ib^{-1})E_{ev} = 0 \tag{7.18}$$

$$-\frac{4\pi\omega^2}{c^2}\chi(\omega,k_1)\,E_1 - \frac{4\pi\omega^2}{c^2}\chi(\omega,k_2)\,E_2 + (\varepsilon_b\,\frac{\omega^2}{c^2} + b^{-2})E_{ev} = 0\,. \tag{7.19}$$

Eliminating E_{ev} from Eqs. (7.18) and (7.19), and using Eqs. (7.15) and

(7.17), we obtain

$$a_1E_1 + a_2E_2 = 0 \quad \text{at} \quad x = 0 \qquad (7.20)$$

with

$$a_i = \frac{\alpha_0\omega_0^2}{\frac{\hbar\omega_0}{M}} \left[\frac{1}{k_i^2 - k_e^2} + \frac{1+S}{2k_e}\left(\frac{1}{k_i + k_e} - \frac{1}{k_i + ib^{-1}}\right)\right]$$

$$+ \frac{\frac{4\pi\omega^2}{c^2}}{\varepsilon_b \frac{\omega^2}{c^2} + b^{-2}} \; \frac{\alpha_0\omega_0^2}{\frac{\hbar\omega_0}{M}} \; \frac{1}{k_i^2 - k_e^2} \times$$

$$\left[\frac{1}{(ib^{-1})^2 - k_e^2} + \frac{1+S}{2k_e}\left(\frac{1}{ib^{-1} + k_e} - \frac{1}{2ib^{-1}}\right)\right] . \qquad (7.21)$$

When b = 0 we have

$$a_i = \frac{\alpha_0\omega_0^2}{2k_e\left(\frac{\hbar\omega_0}{M}\right)} \left[\frac{1}{k_i - k_e} + \frac{S}{k_i + k_e}\right]$$

which is equivalent to the simpler generalized ABC proposed by Zeyher et al.[3] When $b = 0$ and $S = -1$, 1 or 0, (i.e. $a = 0$, ∞, or $-\frac{i}{k_{ex}}$), our generalized ABC will be reduced to ABC 1, 2, or 3 respectively. This can be seen easily if we rewrite the polariton dispersion relation as

$$n_i^2 - \varepsilon_b = \frac{4\pi\alpha_0\omega_0^2}{\frac{\hbar\omega_0}{M}(k_i^2 - k_e^2)} . \qquad (7.22)$$

7.2. RBS Intensity in CdS

1. Experiment

The general features of the experimental apparatus, procedures and conditions were already presented in Chapters 3 and 4. The intensity data presented in this chapter were all taken at liquid-helium-temperatures (T ~ 12 K).

First we will show that although deconvolution is necessary for obtaining real scattering profiles from raw spectra due to finite resolution of the frequency analyser, the integrated intensity is not affected by the analyser thus it could be measured directly from raw spectra.

Suppose the real power spectrum of the scattered signal is $f(\omega)$ and the resolution function (trasmission) of the analyser is $g(\omega,\omega')$, where ω' represents the central frequency of the transmmission of the analyser which is scanning in time. Since the value of $g(\omega,\omega')$ depends only on $\omega-\omega'$, we rewrite $g(\omega,\omega')$ as $g(\omega-\omega')$. The transmmitted intensity when the analyser is centered at ω' will be:

$$I(\omega') = \int_{-\infty}^{\infty} f(\omega)\ g(\omega-\omega')\ d\omega\ ,$$

and the total integrated intensity

$$I_t = \int_{-\infty}^{\infty} I(\omega')\ d\omega' = \int_{-\infty}^{\infty} d\omega' \int_{-\infty}^{\infty} d\omega\ f(\omega)\ g(\omega-\omega')$$

$$= \int_{-\infty}^{\infty} d\omega\ f(\omega) \int_{-\infty}^{\infty} d\omega'\ g(\omega-\omega').$$

Since

$$G = \int_{-\infty}^{\infty} g(\omega-\omega')\ d\omega' \qquad (7.23)$$

is an ω-independent instrumental constant we obtain

$$\int_{-\infty}^{\infty} I(\omega')\ d\omega' = G \int_{-\infty}^{\infty} f(\omega)\ d\omega\ , \qquad (7.24)$$

namely, the total area under the intensity curve in the raw spectrum is directly proportional to the real integrated intensity.

If a scattering component is well isolated from the others, (i.e. the frequency separations between it and its neighbours are bigger than the apparent linewidth which is approximately equal to the sum of the true linewidth and the width of the resolution function) we can derive a relation similar to Eq. (7.24) for this particular component. In our experiment the separation between LA 2-2' and TA 2-2' peaks is greater than 2 cm^{-1} while the apparent linewidths of Stokes LA and TA 2-2' are less than 1 cm^{-1}, therefore the area under each component in the raw spectra is indeed proportional to the real integrated intensity of the component.

We calculated the RBS intensity by

$$I_t = A\ \frac{FSR}{d}\ R\ , \qquad (7.25)$$

where A is the averaged area (in square inches) of a Brillouin component as measured several times with a planimeter, d is the physical distance (in inches) between two adjacent Rayleigh lines, R is the full scale of the ratemeter used during recording with respect to a standard value 1 x 10^4 counts/sec, and FSR is the free spectral range of the Fabry-Perot interferometer relative to a standard value 13.3 cm^{-1}.

Although the signal intensity was relatively reproducible during each continuous performance of a RBS experiment, it changed considerably from time to time due to thermal and/or mechanical instabilities of the apparatus. We matched intensity data obtained on different days by multiplying normalizing factors which were necessary for obtaining a complete set of RBS intensity data.

The integrated intensity vs. incident laser frequency for the Stokes LA 2-2' component is shown by the dots in Fig. 7.5. An intensity maximum occurs at $\tilde{\omega}_{1S}$ = 20586 cm^{-1} and a shoulder at $\tilde{\omega}_{2S}$ = 20596 cm^{-1}. When $\omega_I > \omega_{2S}$, the intensity rapidly decreases with increasing laser frequency. The anti-Stokes LA 2-2' intensity data shows a similar structure with a maximum at $\tilde{\omega}_{1as}$ = 20582 cm^{-1} and a shoulder at $\tilde{\omega}_{2as}$ = 20592 cm^{-1}, as seen in Fig. 7.8.

2. Theory

(1) Integrated Intensity

The integrated intensity of the Stokes LA 2-2' component is given by Eq. (1.30) with i = j = 2, namely:

$$\frac{d\sigma}{d\Omega} = \frac{\pi A}{(2\pi)^3\,(\hbar c)^2}\, T_2(\omega_{I_2})T_2(\omega_{S_2})\, \frac{\omega_{S_2}^{\ 2}\,\left|A_{22}(\mathbf{k}_{I_2},\mathbf{k}_{S_2})\right|^2 \left|\Gamma_0(\mathbf{k}'_{I_2}+\mathbf{k}'_{S_2})\right|^2}{V_{E_2}(\omega_{I_2})\,\left|V_{G_2}(\omega_{S_2})\right|}$$

$$\times\ \frac{1}{k''_{I_2} + k''_{S_2}} \times \left[1 + n_{\text{phonon}}(\omega_{I_2} - \omega_{S_2})\right] . \tag{7.26}$$

The anti-Stokes LA 2-2 intensity is obtained by replacing $\left[1 + n_{\text{phonon}}(\omega_{I_2} - \omega_{S_2})\right]$ by $n_{\text{phonon}}(\omega_{S_2} - \omega_{I_2})$ in Eq. (7.26). The explicit expressions for the relevant quantities in Eq. (7.26) are as follows:[4]

The Bose-Einstein distribution of phonons is

$$n_{\text{phonon}}(\omega) = \frac{1}{\exp(\frac{\hbar\omega}{k_B T}) - 1} . \tag{7.27}$$

The transmissivity of the branch-2 polaritons is

$$T_2(\omega) = \frac{n'_2\gamma}{\gamma - 2B\omega\, n'_2 n''_2}\left|\frac{2a_1}{a_2(1+n_1) - a_1(1+n_2)}\right|^2 , \tag{7.28}$$

where

$$n_2 = \frac{c}{\omega}\,k_2\ ,\quad n'_2 = \frac{c}{\omega}\,k'_2\ ,\quad n''_2 = \frac{c}{\omega}\,k''_2\ , \tag{7.29}$$

$$B = \frac{\hbar\omega_0}{Mc^2} . \tag{7.30}$$

The exciton strength function is

$$A_{22}(k_{I_2},k_{S_2}) = \frac{1}{2}\,A_2(k_{I_2})^{\frac{1}{2}}\left[1 + \frac{\omega_e(k_{I_2})\,\omega_e(k_{S_2})}{\omega_I\omega_S}\right] A_2(k_{S_2})^{\frac{1}{2}} , \tag{7.31}$$

where

$$A_2(k_2) = \frac{2n''_2\omega_e(k_2)}{\gamma - 2B\omega\, n'_2 n''_2}\left[n'_2 + \frac{2\omega\, n''_2(1 + Bn''^2_2)}{\gamma - 2B\omega\, n'_2 n''_2}\right]^{-1} , \tag{7.32}$$

and $\omega_e(k_2)$ is a root of the equation

$$\omega_o^2 - \omega_e^2 + \frac{\hbar\omega_0}{M} k_2^2 - i\omega_e\gamma = 0 .$$

The exciton-LA phonon interaction kernel is

$$\Gamma_0(q) = \left[\frac{\hbar}{2\rho c_{LA}}\right]^{-\frac{1}{2}} (D_e + D_h) q^{\frac{1}{2}} . \qquad (7.33)$$

The energy velocity of the branch-2 polaritons is

$$V_{E_2}(\omega) = c\left[n_2' + \frac{2\omega}{\gamma} n_2'' + \frac{2B\omega\, n_2''}{\gamma} (n_2''^2 - n_2'^2)\right]^{-1} , \qquad (7.34)$$

and the group velocity of the branch-2 polariton is

$$V_{G_2} = \left[\frac{dk_2'}{d\omega}\right]^{-1} . \qquad (7.35)$$

(2) Affect of $\gamma(\omega)$ on RBS Intensity

Detailed numerical calculations using Eqs. (7.26) ~ (7.35) show that the exciton strength function A_{22}, energy velocity V_{E_2} and group velocity V_{G_2} are insensitive to $\gamma(\omega)$, but $k''(\omega)$ and $T(\omega)$ depend strongly on $\gamma(\omega)$ in the exciton resonance region. Therefore the integrated intensity critically depends on not only the ABC, but also $\gamma(\omega)$.

Fig. 7.1 shows the calculated Stokes LA 2-2' intensity vs. incident laser frequency using the same ABC 1 but different $\gamma(\omega)$. The solid line corresponds to $\gamma(\omega)$ given by Eqs. (4.14) and (4.15) (model III) while the broken line corresponds to a constant $\tilde{\gamma}$ = 0.63 cm^{-1} (model I). The two curves are different not only quantitatively, but also qualitatively. Therefore, without knowing the correct ω-dependence of the polariton damping, one could not solve the ABC problem through the analysis of RBS intensity data.

(3) Necessity of a Generalized ABC

Fig. 7.2 shows the calculated Stokes LA 2-2' integrated intensity vs. incident laser frequency using $\gamma(\omega)$ given by Eqs. (4.14), (4.15) (model III) and the three commonly used ABCs discussed in Chapter 1. None of them agree well with the experimental data (solid dots) which suggests that a generalized ABC with some adjustable parameters is necessary to reproduce the observed intensity behavior.

(4) The Fit Result

Using the generalized ABC with adjustable parameters $S = |S| \exp(i\phi)$ (restrited to $|S| \leq 1.0$) and b and different models for $\gamma(\omega)$, we fitted theoretical curves to our measured intensity data and obtained the fit results as shown in Figs. (7.3), (7.4), and (7.5) for $\gamma(\omega)$ of our model I, II and III, respectively. Again $\gamma(\omega)$ of model III gave the best fit. The ABC parameters determined by this best fit were

$$S = (1.0 \pm 0.1)\, e^{i(1.8 \pm 0.2)\pi} \tag{7.36}$$

$$b = (0.23 \pm 0.02)\ \text{Å} . \tag{7.37}$$

This result indicates that the dead layer effect is negligible in the

A-exciton in CdS. The phase angle $\phi \approx - \pi/6$ which shows that the proper choice of ABC falls between ABC 1 and ABC 2 (both having $|S| = 1.0$), but close to ABC 2.

Using resultant fit parameters for S and b, and $\gamma(\omega)$ of model I, II, III, we calculated anti-Stokes LA 2-2' intensity vs. incident laser frequency, as shown in Figs. 7.6, 7.7, and 7.8 respectively. Once more $\gamma(\omega)$ of model III gave the best agreement with the experimental data (solid dots).

3. Discussion and Conclusions

(1) Effect of the dead layer thickness b

The effective dead layer thickness critically affects the RBS intensity in the region $\omega_I > \omega_T$. This can be seen from Fig. 7.9, in which the calculated intensity curves come from the same $\gamma(\omega)$ given by Eqs. (4.14), (4.15) and the same S given by Eq. (7.36), but with different dead layer thicknesses b. As b increases the intensity drops more quickly with increasing laser frequency at $\omega_I > \omega_T$. When b > 20 Å , the intensity curves start to exhibit some peculiar structure which obviously disagrees with experiment. The most probable value seemed to be $b \approx 0$, implying that dead layer effects do not play an important role in RBS experiments in CdS.

(2) Effect of the Scattering Amplitude S

The effect of $|S|$ on RBS intensity can be seen from Fig. 7.10 which shows the calculated Stokes LA 2-2' intensity vs. incident laser frequency using same $\gamma(\omega)$ given by Eqs. (4.14), (4.15) and $b = 0$, $\phi = 1.8\pi$ but for different $|S|$. For smaller $|S|$, a second intensity peak appears at ω_L which was never observed experimentally. The correct choice shoud be $|S| = 1.0$.

The effect of the phase angle ϕ of S can be seen from Fig. 7.11 for $0 \leqq \phi < \pi$, and Fig. 7.12 for $-\pi \leqq \phi < 0$ using $|S| = 1.0$, $b = 0$ and $\gamma(\omega)$ given by Eqs. (4.14) and (4.15). The positive ϕ's are clearly inappropriate since they give very strange intensity behavior over the entire resonance region. Fig. 7.12 shows that RBS intensity is very sensitive to ϕ and the most probable value is $\phi \approx - \pi/6$.

In conclusion, RBS intensity measurements could be a good method to resolve the long controversial ABC problem if the polariton damping $\gamma(\omega)$ is well understood. None of the three commonly used ABCs can explain the observed RBS intensity behavior. A generalized ABC with 3 parameters $|S|$, ϕ and b, as given in Eqs. (7.36) and (7.37) can fit our RBS intensity data very well. RBS intensity behavior is very sensitive to $|S|$, ϕ and b for $\omega_I > \omega_T$. The dead layer effect is negligible in the A-exciton in CdS and the proper choice of ABC falls between ABC 1 and ABC 2, but close to ABC 2.

References

1. Y. Segawa, Y. Aoyagi, S. Komuro, S. Namba, S. Inoue and M. Nakayama, (unpublished); M. Nakayama et al, (unpublished).

2. J. J. Hopfield and D. G. Thomas, Phys. Rev. **132**, 563 (1963).

3. R. Zeyher, J. L. Birman, and W. Brenig, Phys. Rev. B**6**, 4613 (1972).

4. M. Matsushita, J. Wicksted, and H. Z. Cummins, Phys. Rev. B29, 3362 (1984).

Chapter 8. Summary

High resolution RBS experiments were performed in the vicinity of the A-exciton resonance in CdS using a single-mode tunable dye laser and a Fabry-Perot interferometer in series with a double-grating spectrometer. Experiments were performed at liquid-helium and superfluid-helium-temperatures, and compared with BZB theory. The kinematic predictions of the theory, i.e. the Brillouin shifts vs. incident laser frequency, including the Brillouin octet structure in RBS, agreed with our experimental data very well which demonstrates the significance of the polariton picture in the analysis of RBS. However, the simple constant polariton damping model adopted by BZB failed to explain the sharp increase in the observed Brillouin linewidth data above ω_T. Also, the theoretically predicted RBS intensity behavior using either of the three commonly used ABCs deviated considerably from the experiment results.

We were facing two major problems, i.e. frequency-dependent polariton damping in the exciton resonance region and the ABC problem. We started our investigation with the RBS linewidth since it was only related to one of them (the former). As the first attempt to deduce exciton-polariton damping from RBS linewidth analysis, we considered all of the possible polariton decay channels other than RBS itself and found that it was necessary to include a k-linear mixing between the Γ_6 exciton and lower branch of the Γ_{5T} polariton state in order to explain the observed RBS linewidth data. A fit of our theoretical model for polariton damping yielded an estimate of the value for the k-linear coefficient ϕ_A in the A-exciton in CdS, as given in Eq. (4.18) which was about 30 times smaller than that of the B-exciton in CdS.

To further verify our frequency-dependent polariton damping model given by Eqs. (4.14) and (4.15), and to give direct evidence for the existence of the k-linear interaction in the A-exciton in CdS, we investigated RBS linewidths in a weak magnetic field comparable to the k-linear interaction in magnitude. From symmetry considerations, a properly choosed magnetic field can enhance or cancel the assumed k-linear interaction in the A-exciton states and considerably change the RBS linewidth behavior, as shown in Eq. (5.5). We did observe this change around ω_{cr} by comparison of the measured RBS linewidth curves for external magnetic fields of same magnitude but opposite directions, which agreed with theoretical predictions based on our frequency-dependent polariton damping model. In addition, RBS line-splitting was observed clearly around ω_{cr} for B_y = + 9.6 kG. This fact suggested the possibility of directly observing three-branch polariton behavior in the A-exciton in CdS due to the above-mentioned k-linear mixing by further raising instrumental resolution and/or reducing RBS linewidth by lowering the temperature.

We performed RBS experiments at superfluid-helium temperature T = 1.9 K using a very small FSR of 1.0 cm^{-1}. We successfully observed RBS line-splitting (double peaks) around ω_{cr} for both Stokes LA 2-2' and TA 2-2' components, and obtained a direct and accurate determination of the k-linear coefficient ϕ_A in the A-exciton in CdS for the first time, as given in Eq. (6.2). We also found that the RBS linewidth, as well as the polariton damping were greatly reduced at superfluid-helium-temperature.

RBS intensity is a more complicated topic since it is related to not only the long-controversial ABC problem (including the surface effects of crystals), but also the frequency-dependence of the polariton damping. None of the three commonly used ABCs agreed with the observed RBS intensity data. A fit of the theoretical intensity curves using a generalized ABC with our frequency-dependent polariton damping model to the experimental data showed that the dead layer effect in CdS can be neglected and the right choice of ABC falled between ABC 1 and ABC 2, but close to ABC 2.

APPENDIX

Computer Programs

The following programs were used to compute the theoretical results presented in Chapters 4 to 7 of this thesis. They are all stored in the Light Scattering Group Library on the Science Division VAX 780 computer at the City College of the City University of New York.

1. Polariton dispersion

elk4v.f	(3-branch due to k_x at T = 4.2 K)
phykx1.f	(3-branch due to k_x and B_y at T = 4.2 K)
phykx2.f	(3-branch due to k_x and B_y at T = 1.9 K)

2. Brillouin shift

epbs8v.f	(2-branch at T = 4.2 K)
shykx1.f	(3-branch due to k_x and B_y at T = 4.2 K)
shykx2.f	(3-branch due to k_x and B_y at T = 1.9 K)

3. RBS linewidth

epbs8v.f	(for constant damping at T = 4.2 K)
22lwqlv.f	(for damping of model III at T = 4.2 K)
whykxlv.f	(for damping of model III at T = 4.2 K in B_y)

4. RBS intensity

22sli1v.f	(Stokes LA 2-2' intensity, using generalized ABC and frequency-dependent polariton damping at T = 4.2 K)
22ali1v.f	(anti-Stokes LA 2-2' intensity, using generalized ABC and frequency-dependent polariton damping at T = 4.2 K)

5. Nonlinear least square fit

curft2v.f	(main program)
nllsqv.f	(subroutine)

6. Eigenvalue and eigenvector

eigccv.f	(subroutine)

FIGURE CAPTIONS

Fig. 1.1. Schematic diagram of photon and A-exciton dispersion curves in CdS at T = 4.2 K. Broken lines represent the uncoupled exciton and photon propagating in the medium. Solid lines show the exciton-polariton modes, $\omega_1(\mathbf{k})$ and $\omega_2(\mathbf{k})$. The parameter values used are given in Table 1.2 with $\tilde{\gamma} = 1.0\ \mathrm{cm}^{-1}$.

Fig. 1.2. Schematic representation of a backward RBS process involving a semi-infinite spatially dispersive medium. Wavy, solid and broken lines denote photons, polaritons and acoustic phonons, respectively. The rectangle numbered 2 represents the polariton-phonon interaction.

Fig. 1.3. Primitive unit cell of CdS which consists of 2 cadmium atoms located at (0,0,0) and (a/3,2a/3,c/2), and 2 sulfur atoms located at (0,0,u) and (a/3,2a/3,c/2+u), respectively. Structure: Wurtzite. Space group: C_{6v}^{4} . Site symmetry of 4 atoms: C_{3v}. Conventional hexagonal unit vectors: $\mathbf{a}_1 = a\mathbf{x}$, $\mathbf{a}_2 = (-a/2)\mathbf{x} + (\sqrt{3}a/2)\mathbf{y}$, $\mathbf{a}_3 = c\mathbf{z}$. Lattice parameters: a = 4.16 Å , c = 6.75 Å , u = 2.53 Å , θ = 120°.

Fig. 1.4. Energy band structure in CdS at $\mathbf{k} = 0$ and T = 4.2 K.

Fig. 1.5. 1s A-exciton states in CdS at **k** = 0 and T = 4.2 K.

Fig. 3.1. RBS experimental arrangement.

Fig. 3.2. Schematic representation of the Cryo-tip system.

Fig. 4.1. Brillouin scattering spectra of CdS showing Stokes LA 2-2' components for various incident laser frequencies. The free spectral range is 13.3 cm^{-1}. The elastic scattering peak indicates the instrumental linewidth. Note that the true intensity for the lowest four spectra is twice as large as shown in the figure.

Fig. 4.2. Stokes LA 2-2' Brillouin linewidth vs. incident laser frequency. The solid dots are the corrected experimental data. The solid line in (a) is the best fit to model (I) with $\tilde{\gamma}_0 = 0.63\ cm^{-1}$. The solid line in (b) is the best fit to model (II) using Eqs. (4.6) with $\tilde{\gamma}_0 = 0.12\ cm^{-1}$ and $\tilde{\gamma}_1 = 0.35\ cm^{-1}$. The solid line in (c) is the best fit to model (III) using Eq. (4.14) with $\tilde{\gamma}_0 = 0.24\ cm^{-1}$, $\tilde{\gamma}_1 = 0.09\ cm^{-1}$, $\tilde{\gamma}_2 = 2.7\ cm^{-1}$ and e = 0.06 .

Fig. 4.3. Calculated dispersion curves of $\Gamma_{5T}(A)$ exciton-polaritons and $\Gamma_6(A)$ excitons including the k-linear interaction between them. Inset: Schematic representation of the dispersion curves near the crossing frequency ω_{cr}. The broken lines show the lower branch

of the $\Gamma_{5T}(A)$ polariton and $\Gamma_6(A)$ exciton without the k-linear interaction.

Fig. 4.4. Anti-Stokes LA 2-2' Brillouin linewidths vs. incident laser frequency. The solid dots are the experimental data. The solid lines are calculated linewidths using the parameters found from the Stokes LA 2-2' fits based on $\gamma(\omega)$ of model I, II, and III respectively.

Fig. 4.5. Frequency dependence of the polariton damping $\gamma(\omega)$ found from the Brillouin linewidth data with model I [Eq. (4.5)], model II [Eqs. (4.6) and (4.7)] and model III [Eqs. (4.14) and (4.15)].

Fig. 4.6. **(a)** Lifetime of polaritons corresponding to the $\gamma(\omega)$ obtained from the best fit of the RBS linewidth data to model III. **(b)** Polariton lifetime measured by Wiesner and Heim with time-resolved luminescence spectroscopy.

Fig. 5.1. Calculated dispersion curves of $\Gamma_{5T}(A)$ exciton-polaritons and $\Gamma_6(A)$ excitons including the k-linear interaction between them in the presence of a magnetic field **(a)** $B_y = + 4.8$ kG ; **(b)** $B_y = - 4.8$ kG.

Fig. 5.2. Calculated damping constants of incident (solid lines) and scattered exciton-polaritons (broken lines) for **(a)** $B_y = + 4.8$

kG ; **(b)** $B_y = - 4.8$ kG ; and **(c)** $B_y = 0$.

Fig. 5.3. Calculated Stokes LA 2-2' Brillouin linewidths vs incident laser frequency. The solid line is for $B_y = + 4.8$ kG, the broken line for $B_y = - 4.8$ kG, and the dotted line for $B_y = 0$.

Fig. 5.4. RBS geometries: **(a)** Backscattered RBS geometry with $B_y > 0$. **(b)** Backscattered RBS geometry with $B_y < 0$ obtained from (a) by reversing the direction of the magnetic field. **(c)** Backscattered RBS geometry with $B_y < 0$ obtained from (a) by turning the crystal upside down.

Fig. 5.5. Observed Stokes LA 2-2' linewidths vs incident laser frequency for $B_y = 0$ with **(a)** the scattering geometry shown in Fig. 5.4(a); **(b)** the scattering geometry shown in Fig. 5.4(c).

Fig. 5.6. Observed Stokes LA 2-2' linewidths vs incident laser frequency for **(a)** $B_y = + 4.8$ kG; **(b)** $B_y = - 4.8$ kG. Solid dots represent the experimental data, and solid lines are theoretical predictions.

Fig. 5.7. Observed Stokes LA 2-2' profiles at $\tilde{\omega} = 20592.0$ cm^{-1} for $B_y = - 4.8$ kG, 0, and + 4.8 kG. Frequency increases from left to right in each spectrum.

Fig. 5.8. Observed Stokes TA 2-2' linewidths vs incident laser frequency for (a) B_y = + 4.8 kG; and (b) B_y = - 4.8 kG.

Fig. 5.9. Observed Stokes LA 2-2' linewidths vs incident laser frequency for (a) B_y = + 9.6 kG ; (b) B_y = - 9.6 kG.

Fig. 5.10. Observed Stokes LA 2-2' profiles for B_y = + 9.6 kG at different laser frequencies. Frequency increases from left to right in each spectrum.

Fig. 6.1. Effects of mixing on the A-exciton in CdS. **(a)** The optically-active Γ_{5T} exciton interacts with the photon producing the two-branch polariton. The lower polariton branch 2 crosses the optically-forbidden Γ_6 exciton at ω_{cr}. **(b)** The Γ_{5T} and Γ_6 excitons are mixed by the k-linear interaction producing two hybridized exciton states. Note that there is no displacement of the energy minima in this case due to the relative weakness of the coupling in contrast to Fig. 1(b) in Ref. 5 of Chapter 6 for the B-exciton in CdS. **(c)** Three-branch exciton-polariton dispersion curves resulting from the simultaneous interactions in (a) and (b). The curves shown here resulted from Eq. (6.1) using parameter values discussed in the text. Polariton branches 2 and 3 both have significant oscillator strength only in the vicinity of ω_{cr}. Note that (c) is drawn to scale, while (a) and (b) are schematic.

Fig. 6.2. Stokes LA and TA 2-2' Brillouin shifts (dots) and theoretical curves (lines) computed using the parameters given in the text. The inset shows an enlarged section of the LA curves near ω_{cr} where splitting is observed. The gradation of the dots illustrates schematically the relative intensity of the L_α and L_β components.

Fig. 6.3. Brillouin spectra showing Stokes LA and TA 2-2' components at three different laser frequencies near ω_{cr}. The relative positions of LA and TA components in (b) and (c) are distorted by the effect of overlapping orders inherent to the Fabry-Perot output. The real positions of LA and TA peaks should be read on separate scales.

Fig. 6.4. Measured and calculated spectral splitting of Stokes LA and TA 2-2' Brillouin components. The solid lines are the best fit results with $\phi_A = 2.7 \times 10^{-11}$ eV cm.

Fig. 6.5. **(a)** Measured (dots) and calculated (lines) Stokes LA 2-2' Brillouin linewidth vs incident laser frequency. The crosses represent the measured average linewidth of split components L_α and L_β near ω_{cr}. **(b)** Resulting polariton damping constant $\gamma(\omega)$ at 1.9 K as given in Eq. (6.3) and (6.4).

Fig. 7.1. Calculated Stokes LA 2-2' integral intensities vs incident laser frequency using ABC 1 and two different $\gamma(\omega)$. The broken line corresponds to $\tilde{\gamma} = 0.63$ cm^{-1} (model I). The solid line corres-

ponds to $\gamma(\omega)$ given by Eqs. (4.14) and (4.15) (model III).

Fig. 7.2. Calculated Stokes LA 2-2' integral intensities vs incident laser frequency using $\gamma(\omega)$ given by Eqs. (4.14) and (4.15) (model III) and ABC 1, 2, and 3 respectively. The solid dots are experimental data.

Fig. 7.3. The best fit result (solid line) for Stokes LA 2-2' integrated intensity vs incident laser frequency using a generalized ABC and a constant $\tilde{\gamma} = 0.63$ cm^{-1} (model I). The resultant parameters are $S = 1.0 \exp(i1.9\pi)$, $b = 0.0003$ Å. The solid dots are experimental data.

Fig. 7.4. The best fit result (solid line) for Stokes LA 2-2' integrated intensity vs incident laser frequency using a generalized ABC and $\gamma(\omega)$ given by Eqs. (4.6) and (4.7) (model II). The resultant parameters are $S = 1.0 \exp(i1.8\pi)$, $b = 0.24$ Å. The solid dots are experimental data.

Fig. 7.5. The best fit result (solid line) for Stokes LA 2-2' integrated intensity vs incident laser frequency using a generalized ABC and $\gamma(\omega)$ given by Eqs. (4.14) and (4.15) (model III). The resultant parameters are $S = 1.0 \exp(i1.8\pi)$, $b = 0.23$ Å. The solid dots are experimental data.

Fig. 7.6. Calculated (solid line) anti-Stokes LA 2-2' integral intensity vs incident laser frequency using a generalized ABC with S = 1.0 exp(i1.9π), b = 0.0003 Å, and a constant γ = 0.63 cm^{-1} (model I). The solid dots are experimental data.

Fig. 7.7. Calculated (solid line) anti-Stokes LA 2-2' integral intensity vs incident laser frequency using a generalized ABC with S = 1.0 exp(i1.8π), b = 0.24 Å, and $\gamma(\omega)$ given by Eqs. (4.6) and (4.7) (model II). The solid dots are experimental data.

Fig. 7.8. Calculated (solid line) anti-Stokes LA 2-2' integral intensity vs incident laser frequency using a generalized ABC with S = 1.0 exp(i1.8π), b = 0.23 Å, and $\gamma(\omega)$ given by Eqs. (4.14) and (4.15) (model III). The solid dots are experimental data.

Fig. 7.9. Calculated (solid line) Stokes LA 2-2' integral intensities vs incident laser frequency using $\gamma(\omega)$ given by Eqs. (4.14) and (4.15) (modal III) and a generalized ABC with S = 1.0 exp(i1.8π), but different b. The solid dots are experimental data.

Fig. 7.10. Calculated (solid line) Stokes LA 2-2' integral intensities vs incident laser frequency using $\gamma(\omega)$ given by Eqs. (4.14) and (4.15) (model III) and a generalized ABC with ϕ = 1.84π, b = 0, but different |S|. The solid dots are experimental data.

Fig. 7.11. Calculated (solid line) Stokes LA 2-2' integral intensities vs incident laser frequency using $\gamma(\omega)$ given by Eqs. (4.14) and (4.15) (model III) and a generalized ABC with S = 1.0, b = 0, but different ϕ ranging from 0 to π. The solid dots are experimental data.

Fig. 7.12. Calculated (solid line) Stokes LA 2-2' integral intensities vs incident laser frequency using $\gamma(\omega)$ given by Eqs. (4.14) and (4.15) (model III) and a generalized ABC with S = 1.0, b = 0, but different ϕ ranging from $-\pi$ to 0. The solid dots are experimental data.

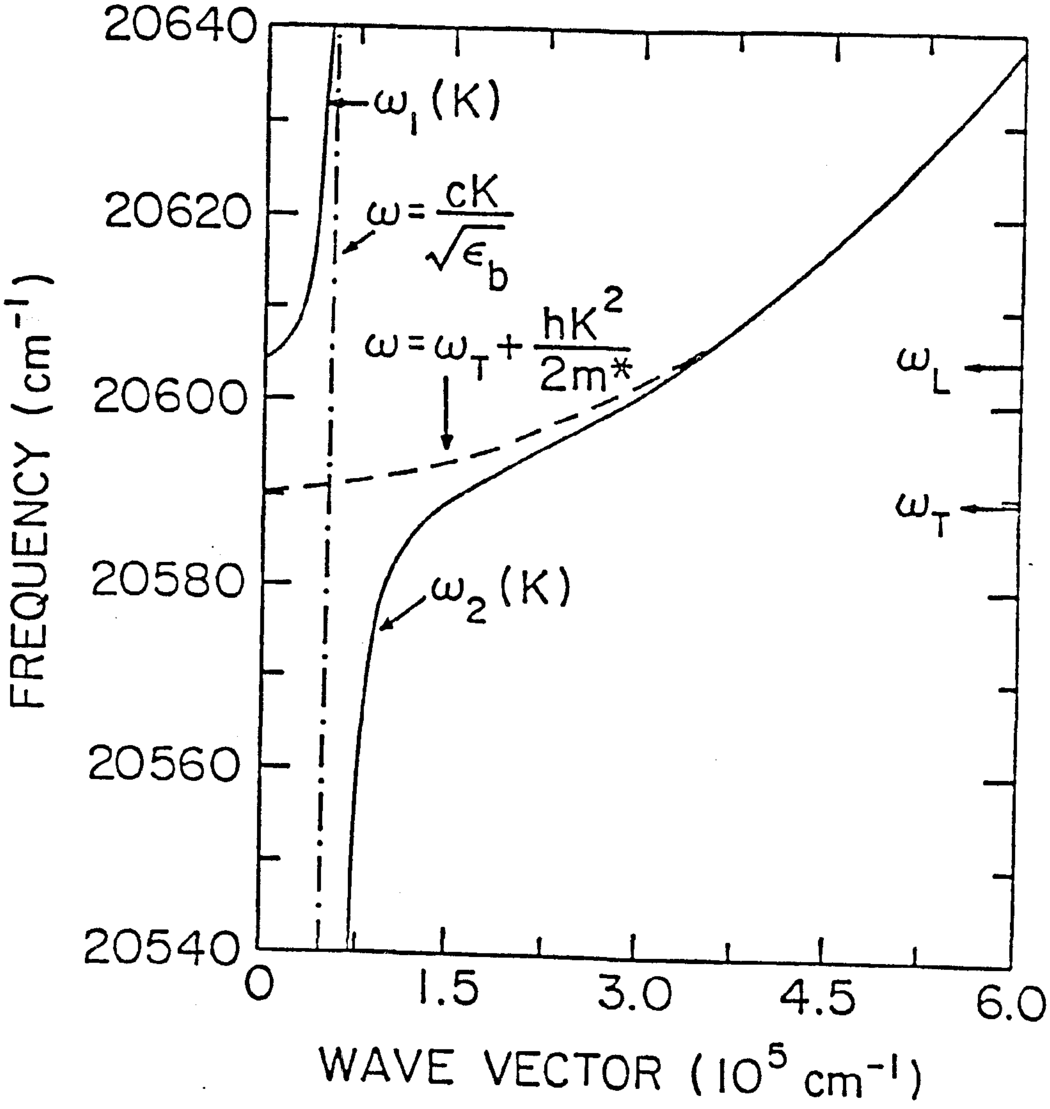
20640
20620
20600
20580
20560
20540
FREQUENCY (cm^{-1})
0
1.5
3.0
4.5
6.0
WAVE VECTOR (10^5 cm^{-1})
$\omega_1(K)$
$\omega = \frac{cK}{\sqrt{\epsilon_b}}$
$\omega = \omega_T + \frac{hK^2}{2m^*}$
$\omega_2(K)$
ω_L
ω_T

FIG.1.1

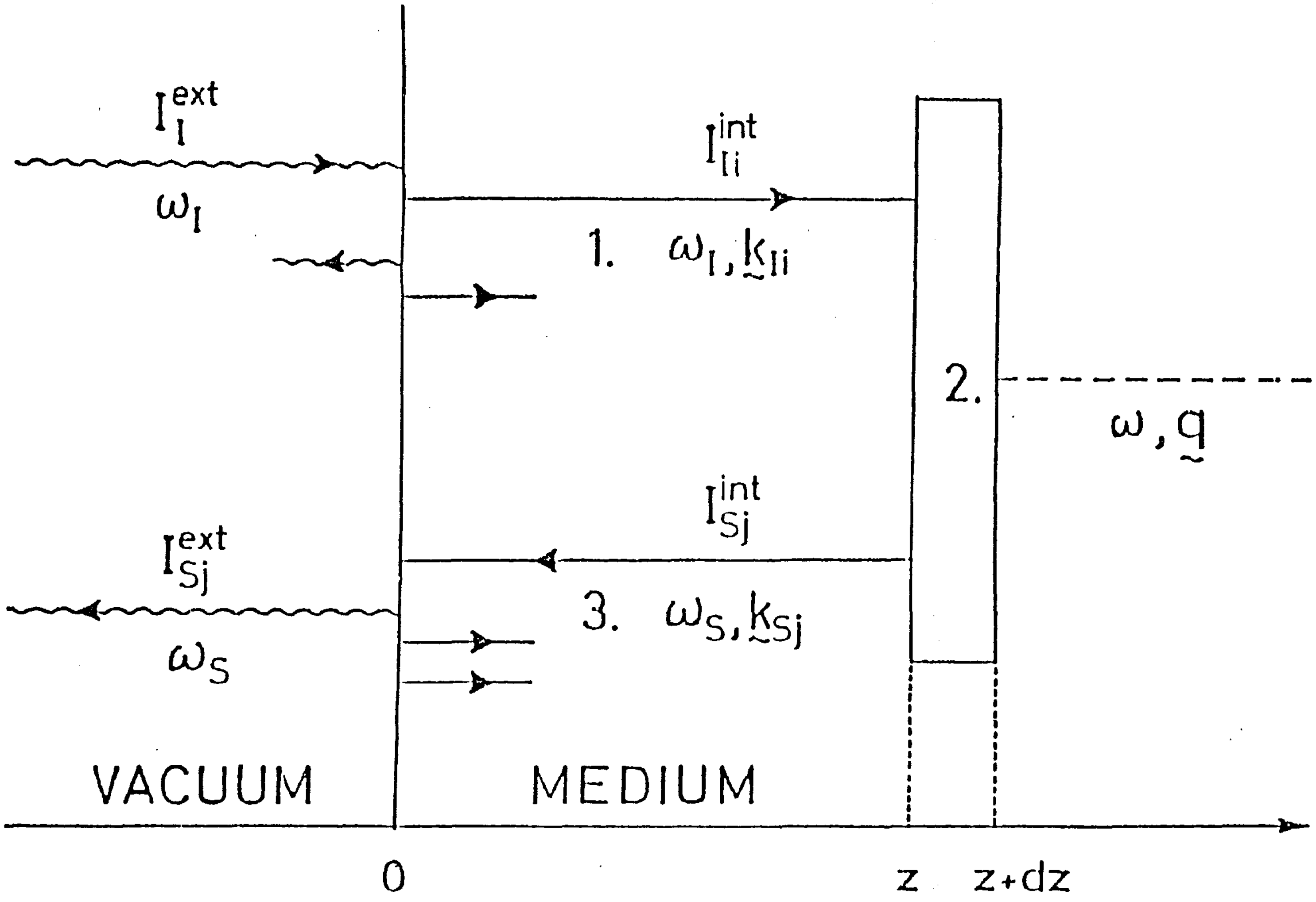
I_I^{ext}
ω_I
I_{Ii}^{int}
1. $\omega_I, \underset{\sim}{k}_{Ii}$
2.
$\omega, \underset{\sim}{q}$
I_{Sj}^{int}
I_{Sj}^{ext}
3. $\omega_S, \underset{\sim}{k}_{Sj}$
ω_S
VACUUM
MEDIUM
0
z
z+dz

FIG.1.2

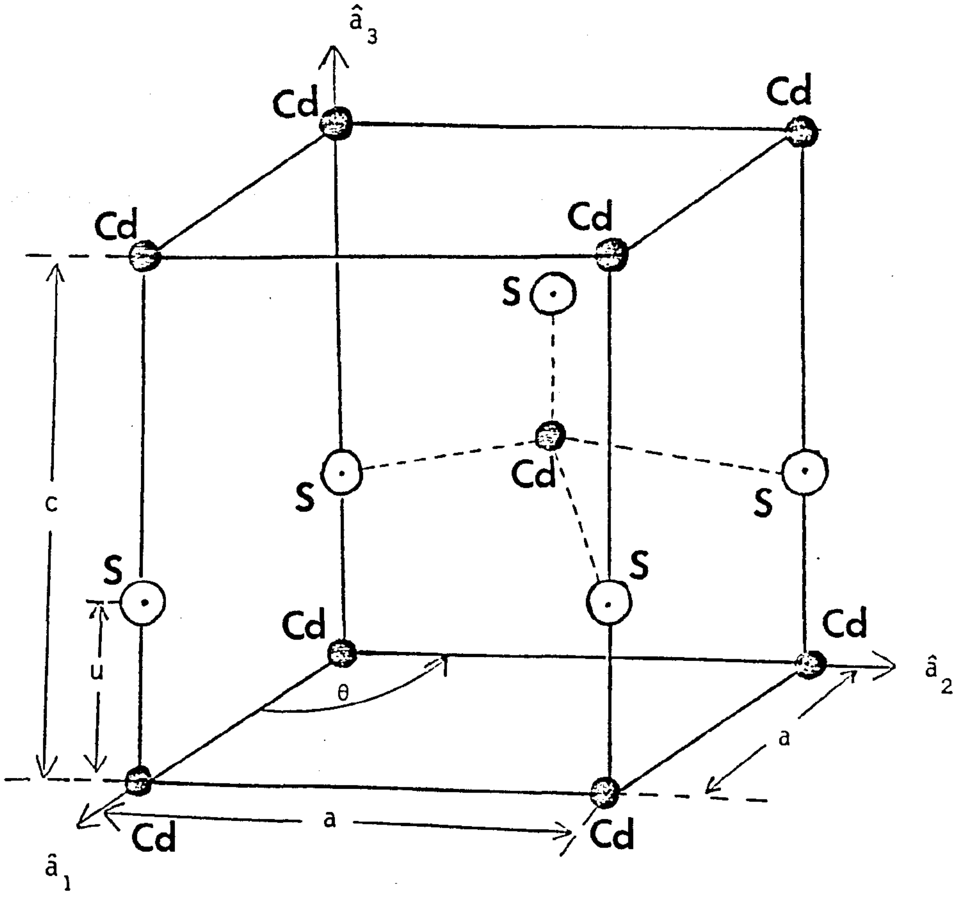

FIG.1.3

The Band Structure of CdS at k=0

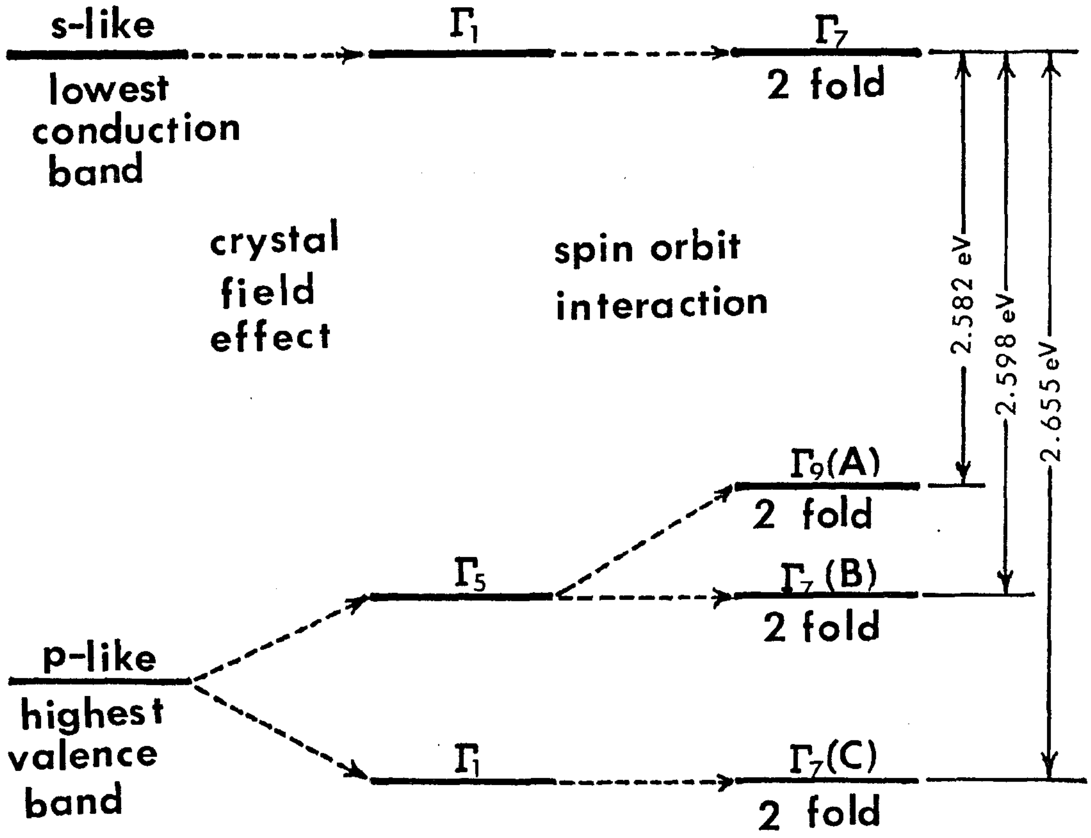

FIG.1.4

1S A-Exciton Levels in CdS at k=0

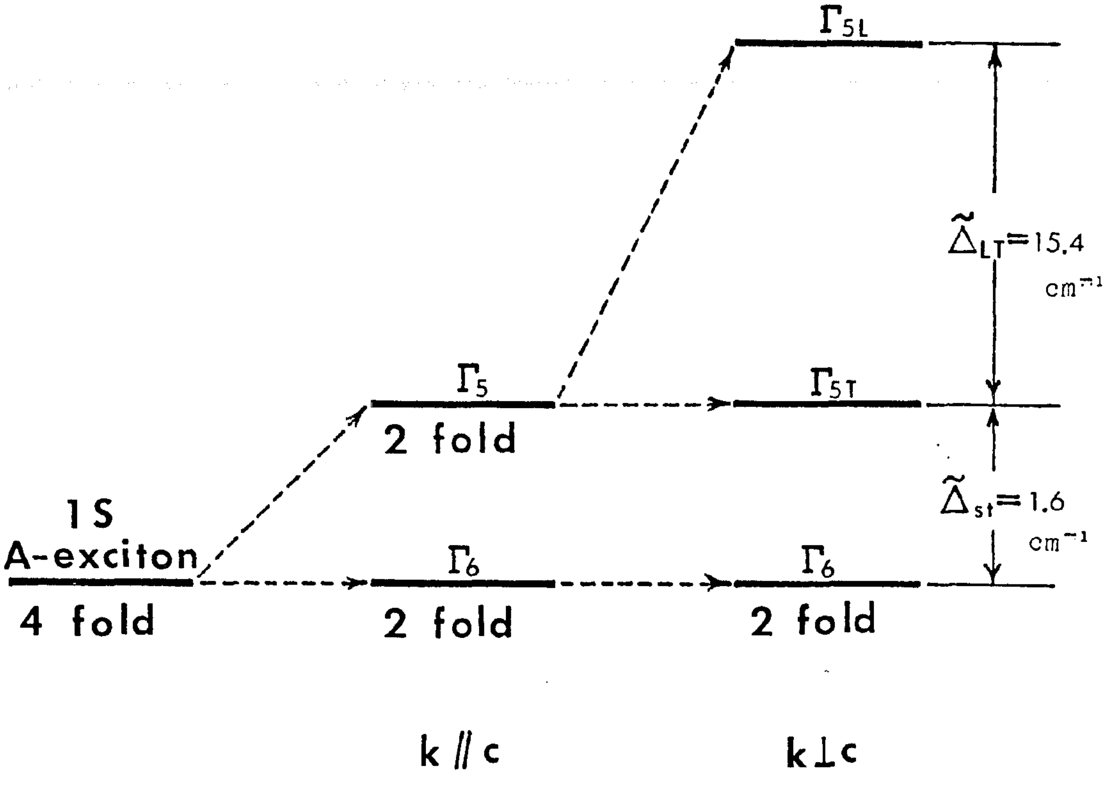

short range
exchange
interaction

long range
exchange
interaction

FIG. 1.5

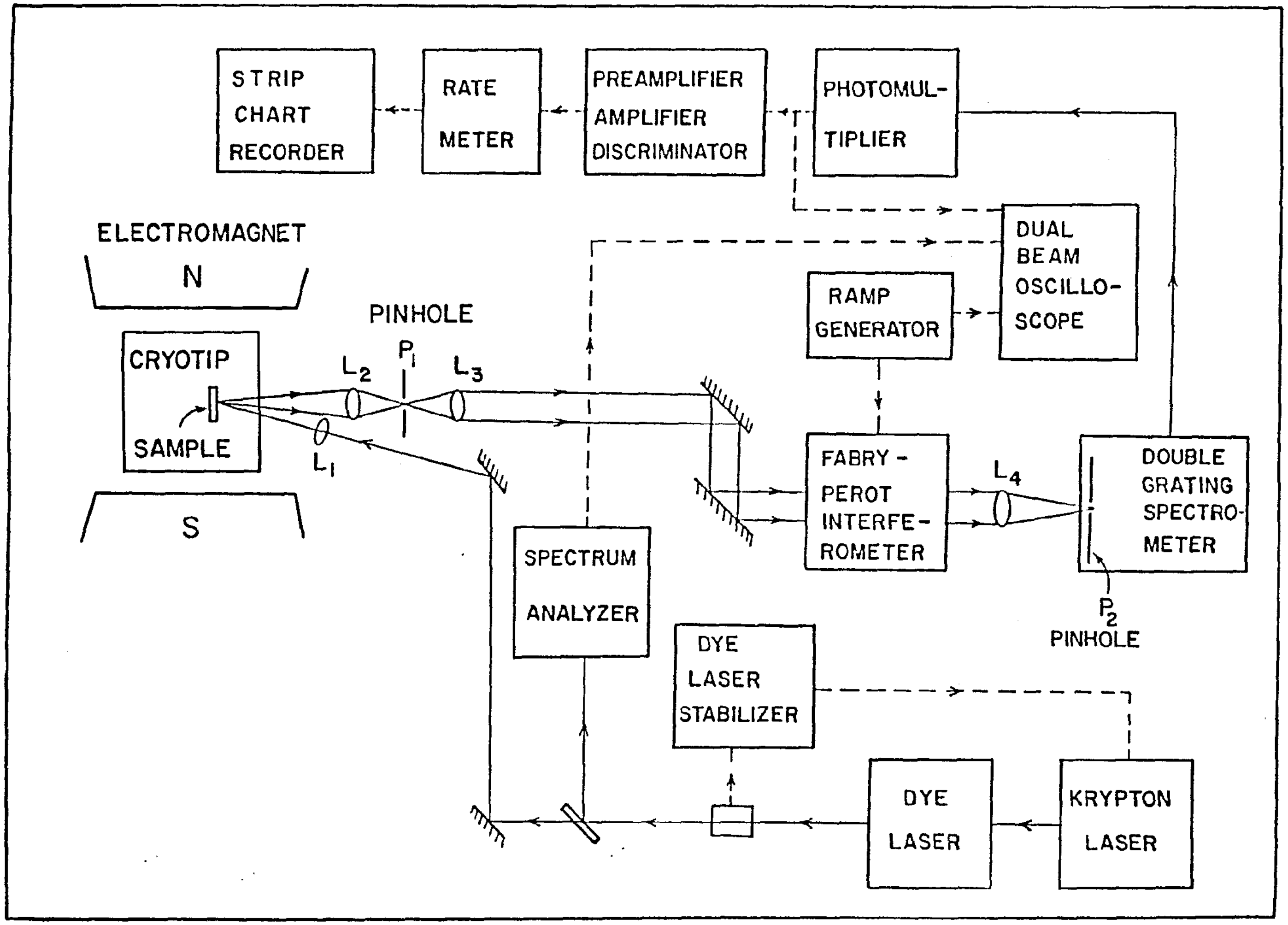
STRIP CHART RECORDER
RATE METER
PREAMPLIFIER AMPLIFIER DISCRIMINATOR
PHOTOMULTIPLIER
ELECTROMAGNET
N
S
CRYOTIP
SAMPLE
PINHOLE
P_1
L_1
L_2
L_3
DUAL BEAM OSCILLOSCOPE
RAMP GENERATOR
FABRY-PEROT INTERFEROMETER
L_4
DOUBLE GRATING SPECTROMETER
P_2
PINHOLE
SPECTRUM ANALYZER
DYE LASER STABILIZER
DYE LASER
KRYPTON LASER

FIG.3.1

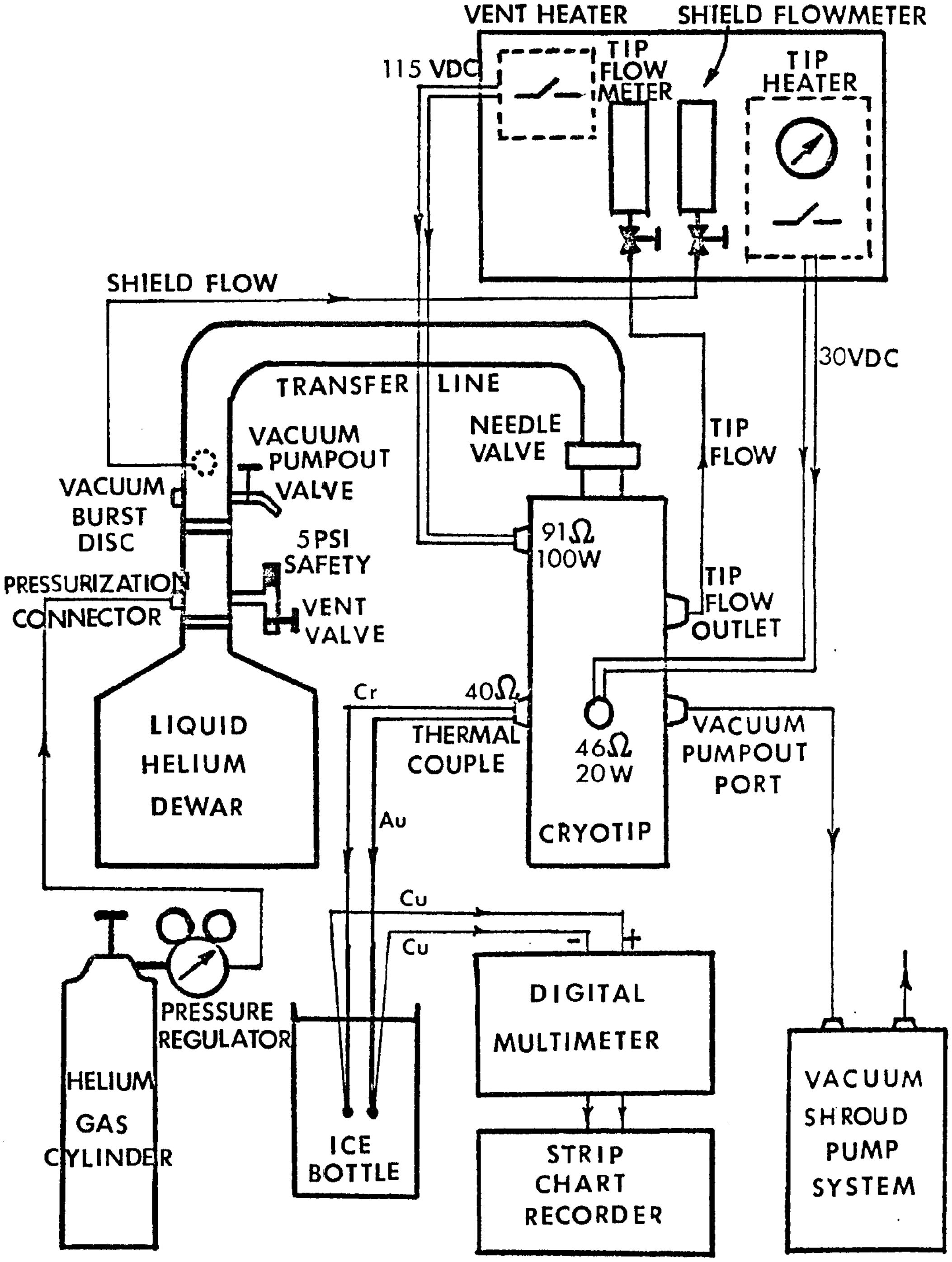
VENT HEATER
SHIELD FLOWMETER
115 VDC
TIP FLOW METER
TIP HEATER
SHIELD FLOW
30VDC
TRANSFER LINE
NEEDLE VALVE
VACUUM PUMPOUT VALVE
TIP FLOW
VACUUM BURST DISC
5PSI SAFETY
91Ω 100W
PRESSURIZATION CONNECTOR
VENT VALVE
TIP FLOW OUTLET
Cr
40Ω
THERMAL COUPLE
46Ω 20W
VACUUM PUMPOUT PORT
LIQUID HELIUM DEWAR
Au
CRYOTIP
Cu
Cu
-
+
DIGITAL MULTIMETER
PRESSURE REGULATOR
HELIUM GAS CYLINDER
ICE BOTTLE
STRIP CHART RECORDER
VACUUM SHROUD PUMP SYSTEM

FIG.3.2

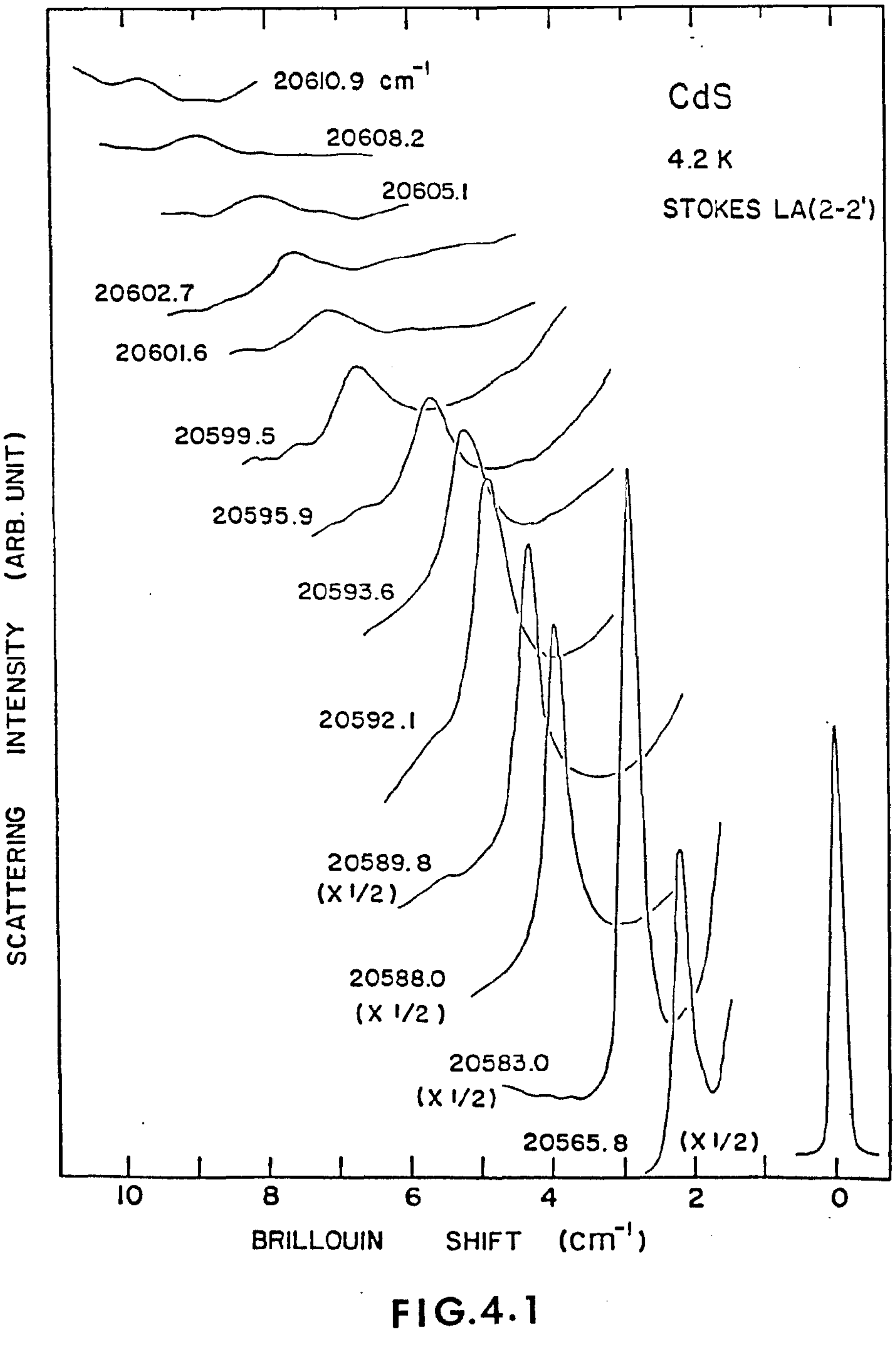
20610.9 cm^{-1}
20608.2
20605.1
20602.7
20601.6
20599.5
20595.9
20593.6
20592.1
20589.8
(X 1/2)
20588.0
(X 1/2)
20583.0
(X 1/2)
20565.8
(X 1/2)
CdS
4.2 K
STOKES LA(2-2')
SCATTERING INTENSITY (ARB. UNIT)
10
8
6
4
2
0
BRILLOUIN SHIFT (cm^{-1})

FIG.4.1

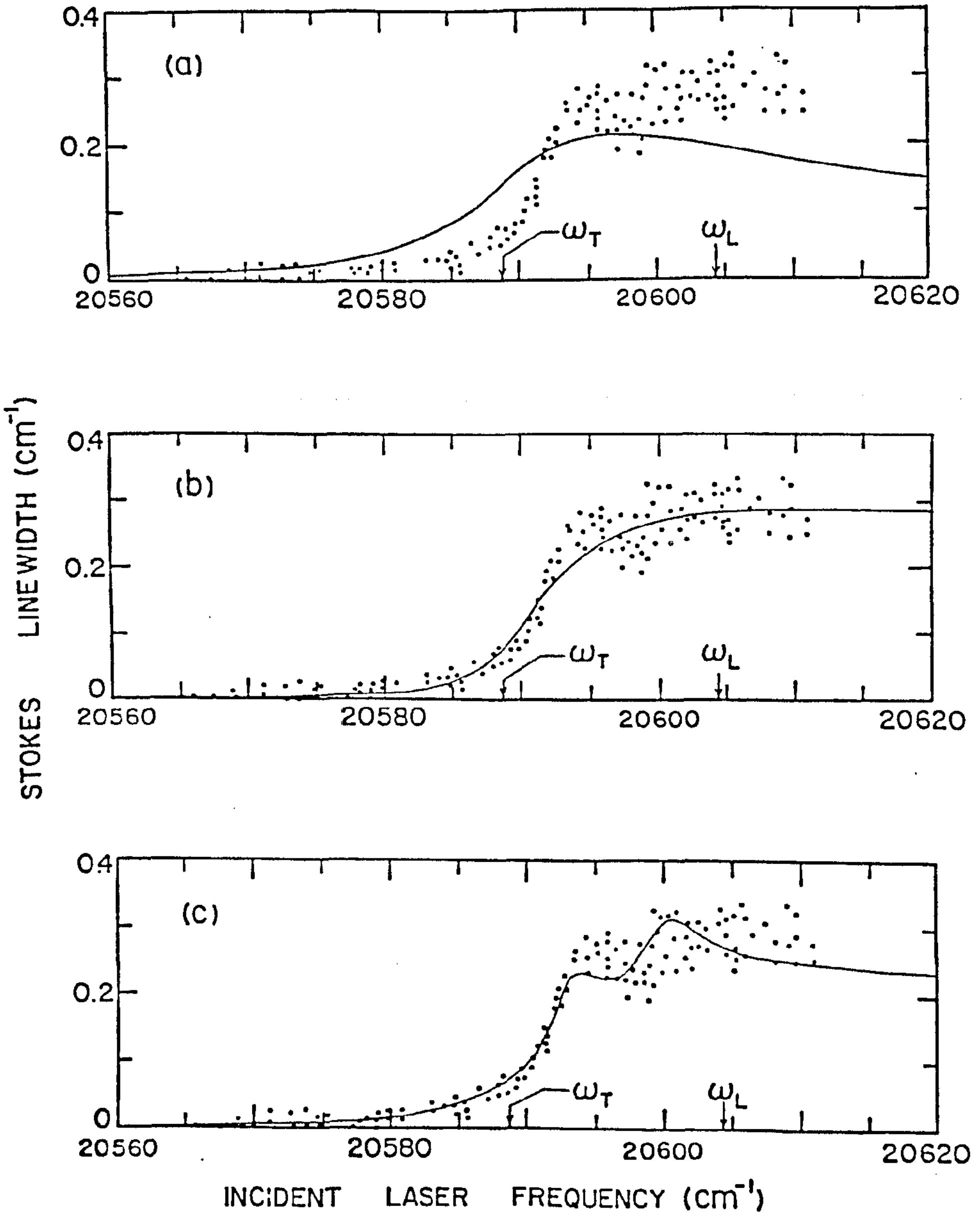
(a)
(b)
(c)
0.4
0.2
0
20560
20580
20600
20620
ω_T
ω_L
STOKES LINEWIDTH (cm^{-1})
INCIDENT LASER FREQUENCY (cm^{-1})

FIG.4.2

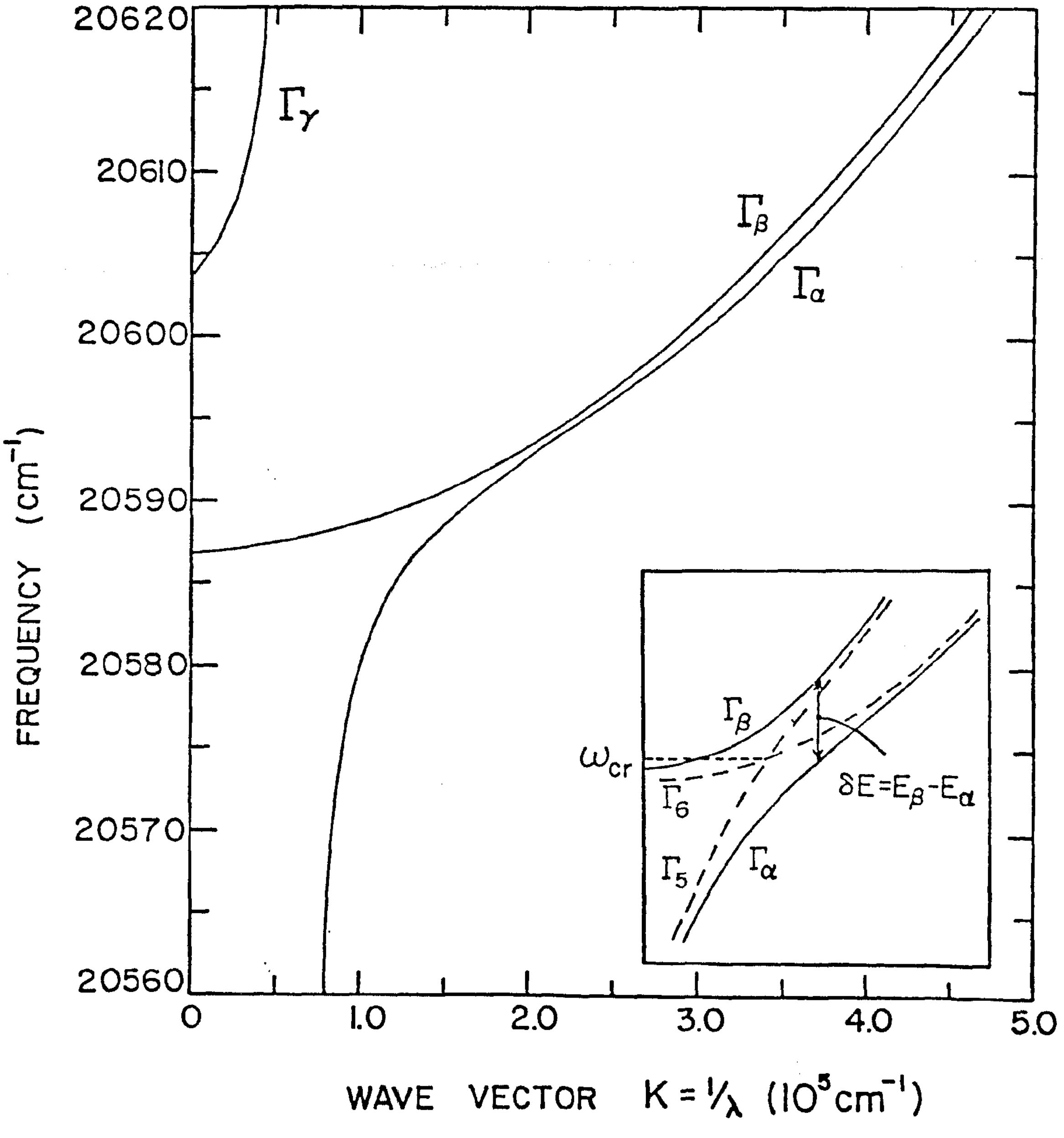
20620
20610
20600
20590
20580
20570
20560
FREQUENCY (cm⁻¹)
0
1.0
2.0
3.0
4.0
5.0
WAVE VECTOR K = 1/λ (10⁵cm⁻¹)
Γγ
Γβ
Γα
ωcr
Γβ
Γ6
Γ5
Γα
δE=Eβ-Eα

FIG.4.3

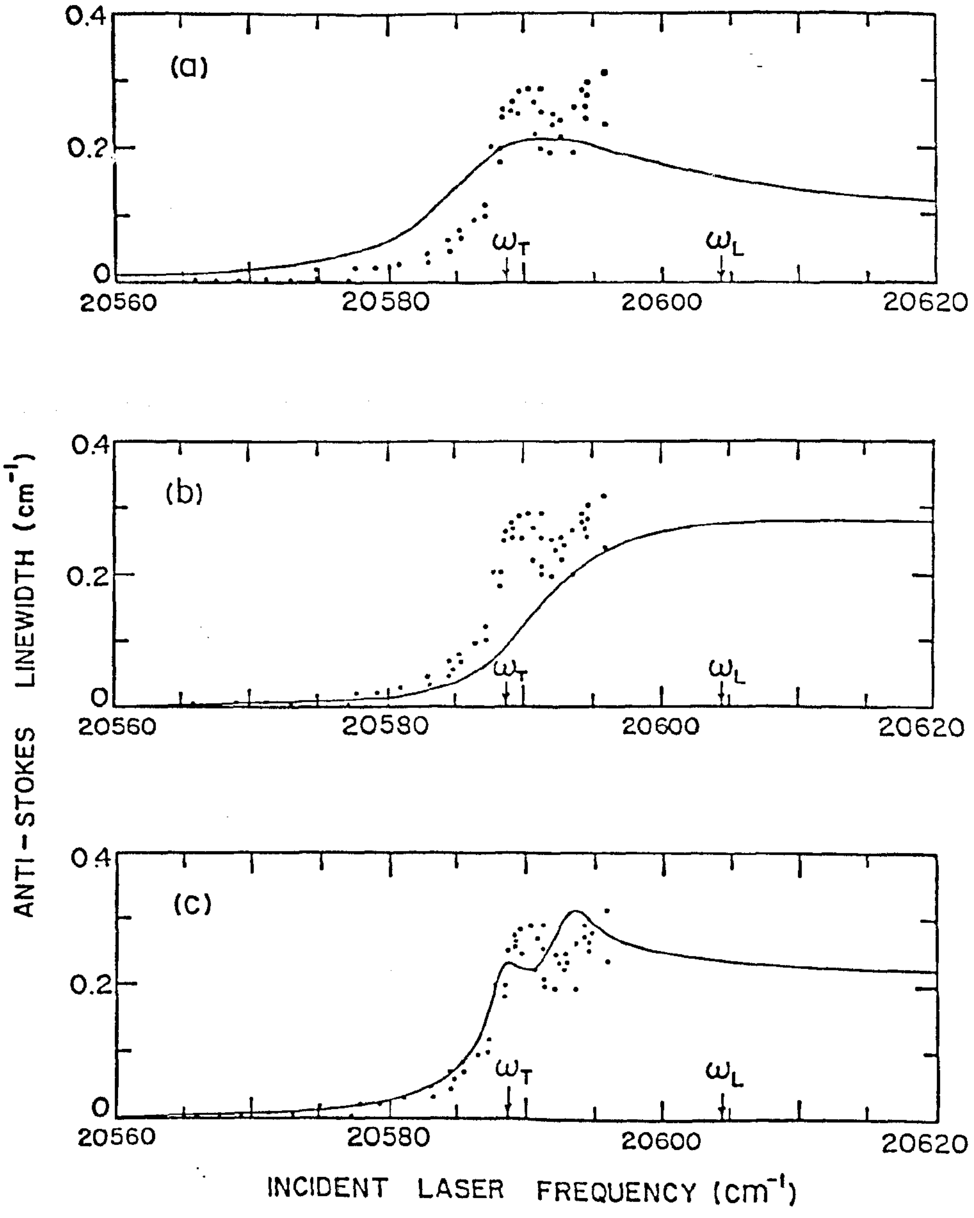
(a)
(b)
(c)
0.4
0.2
0
ω_T
ω_L
20560
20580
20600
20620
ANTI - STOKES LINEWIDTH (cm^{-1})
INCIDENT LASER FREQUENCY (cm^{-1})

FIG.4.4

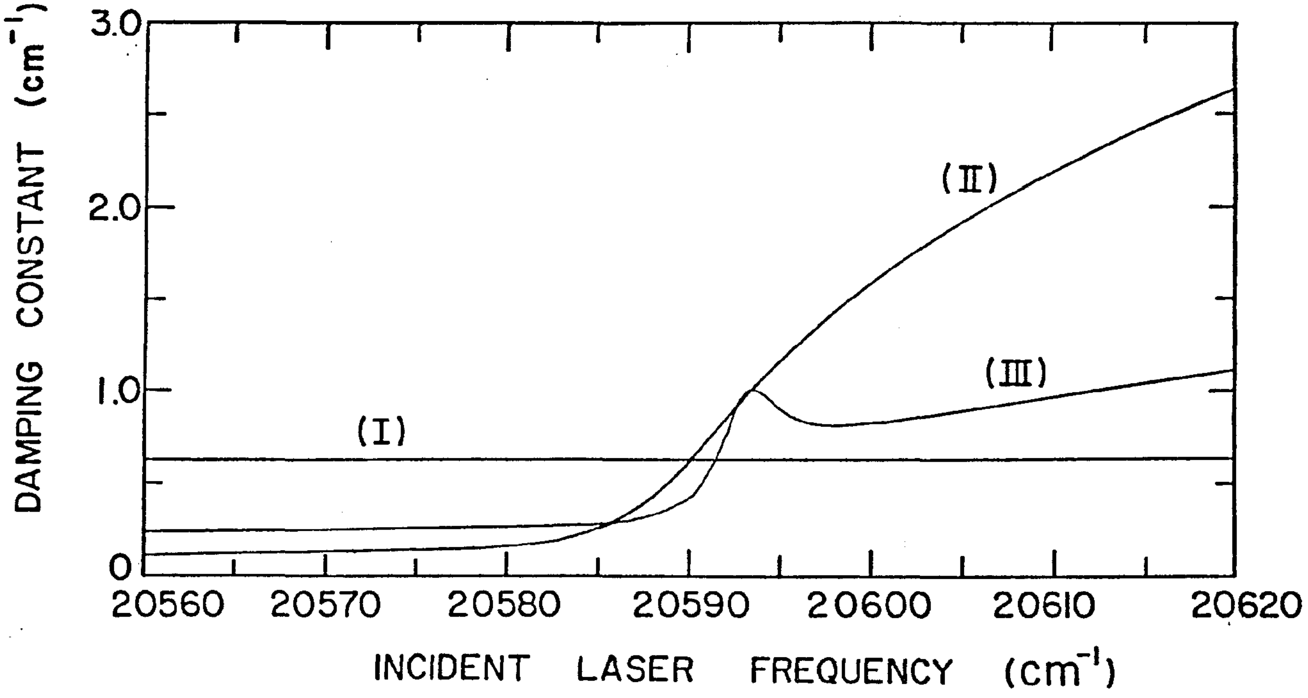
DAMPING CONSTANT (cm^{-1})
3.0
2.0
1.0
0
(I)
(II)
(III)
20560
20570
20580
20590
20600
20610
20620
INCIDENT LASER FREQUENCY (cm^{-1})

FIG.4.5

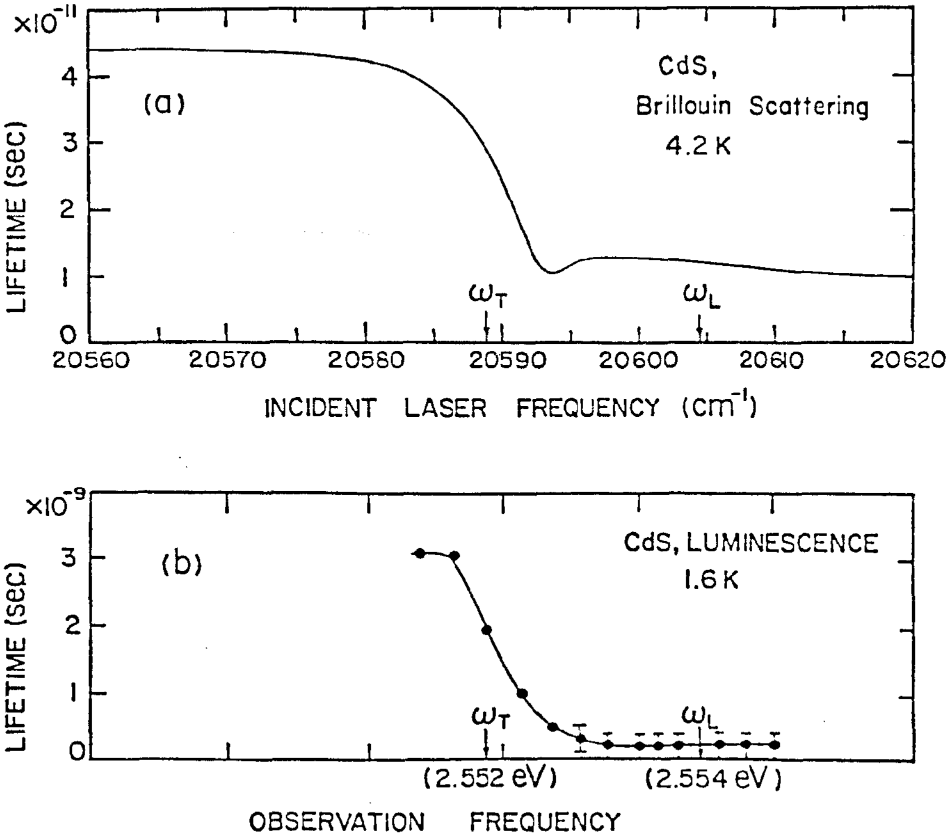
×10⁻¹¹
4
3
2
1
0
(a)
CdS,
Brillouin Scattering
4.2 K
LIFETIME (sec)
ωT
ωL
20560
20570
20580
20590
20600
20610
20620
INCIDENT LASER FREQUENCY (cm⁻¹)
×10⁻⁹
3
2
1
0
(b)
CdS, LUMINESCENCE
1.6 K
LIFETIME (sec)
ωT
ωL
(2.552 eV)
(2.554 eV)
OBSERVATION FREQUENCY

FIG.4.6

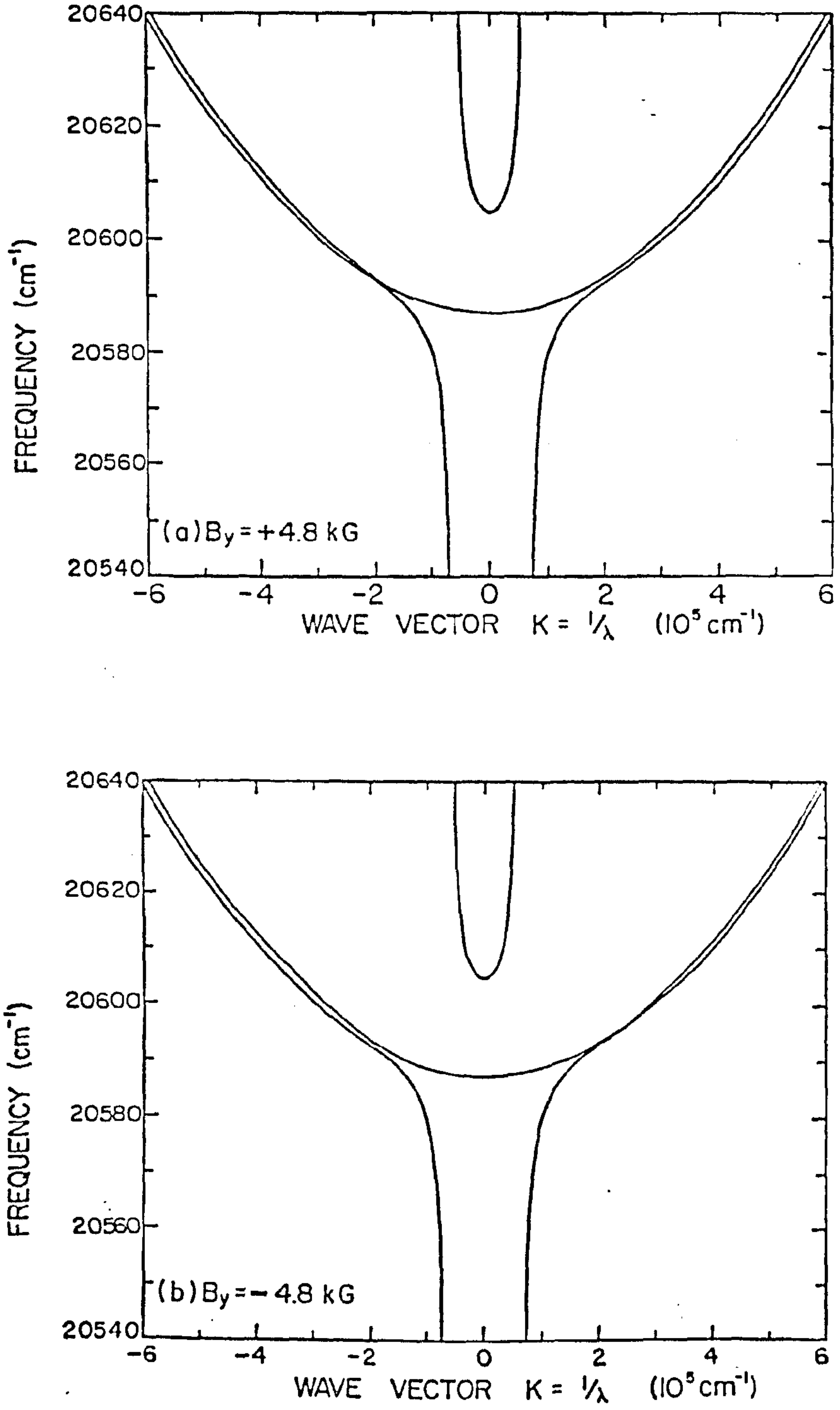
20640
20620
20600
20580
20560
20540
FREQUENCY (cm^{-1})
(a) B_y = +4.8 kG
-6
-4
-2
0
2
4
6
WAVE VECTOR K = 1/λ (10^5 cm^{-1})
20640
20620
20600
20580
20560
20540
FREQUENCY (cm^{-1})
(b) B_y = − 4.8 kG
-6
-4
-2
0
2
4
6
WAVE VECTOR K = 1/λ (10^5 cm^{-1})

FIG.5.1

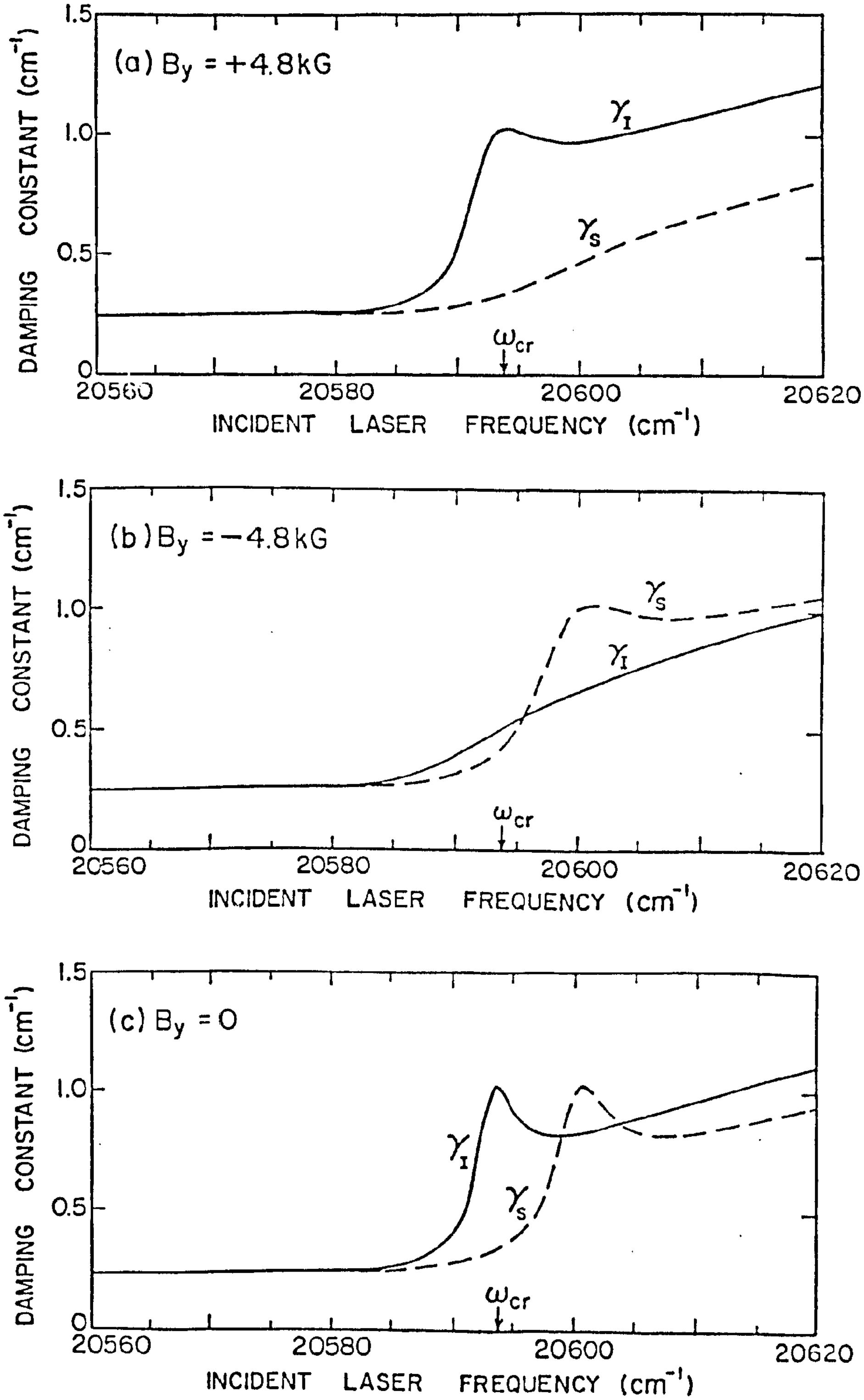
(a) B_y = +4.8kG
γ_I
γ_s
ω_{cr}
(b) B_y = −4.8kG
γ_s
γ_I
ω_{cr}
(c) B_y = 0
γ_I
γ_s
ω_{cr}
DAMPING CONSTANT (cm^{-1})
0
0.5
1.0
1.5
20560
20580
20600
20620
INCIDENT LASER FREQUENCY (cm^{-1})

FIG.5.2

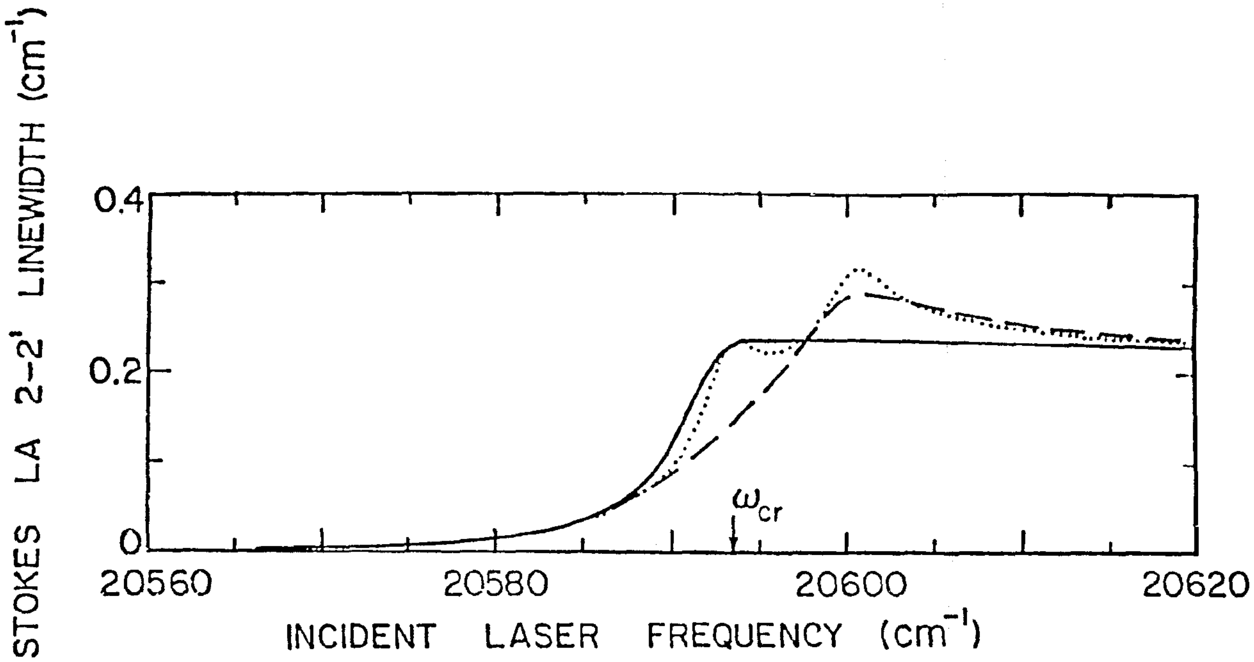
STOKES LA 2-2' LINEWIDTH (cm^{-1})
0.4
0.2
0
ω_{cr}
20560
20580
20600
20620
INCIDENT LASER FREQUENCY (cm^{-1})

FIG.5.3

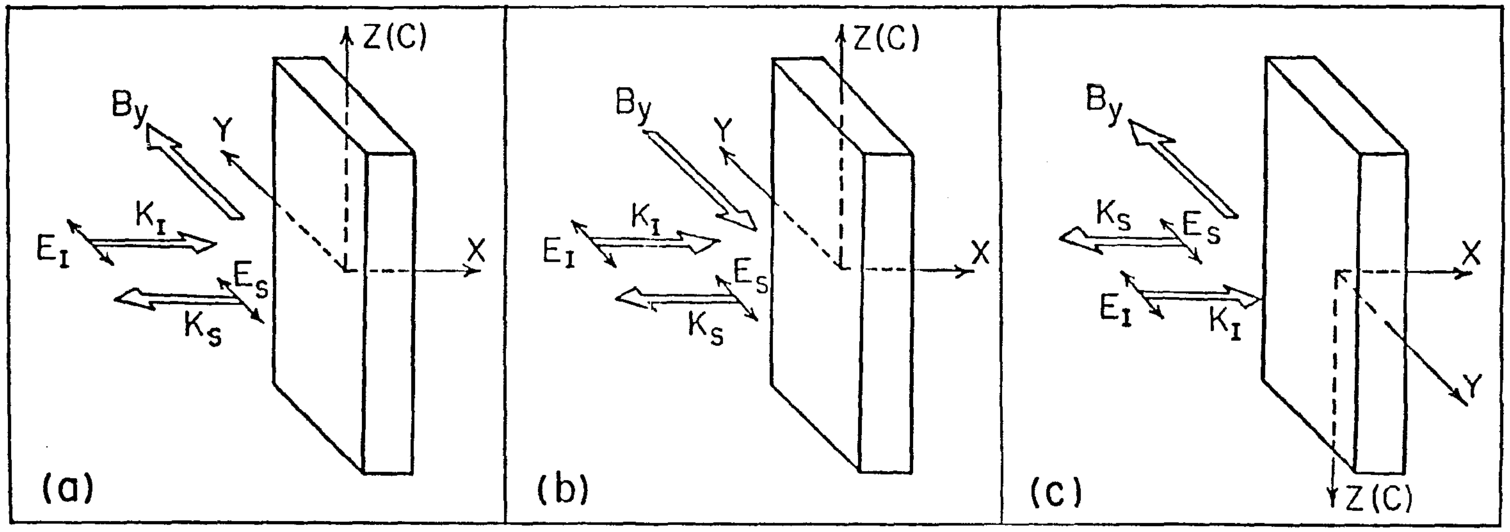

FIG. 5.4

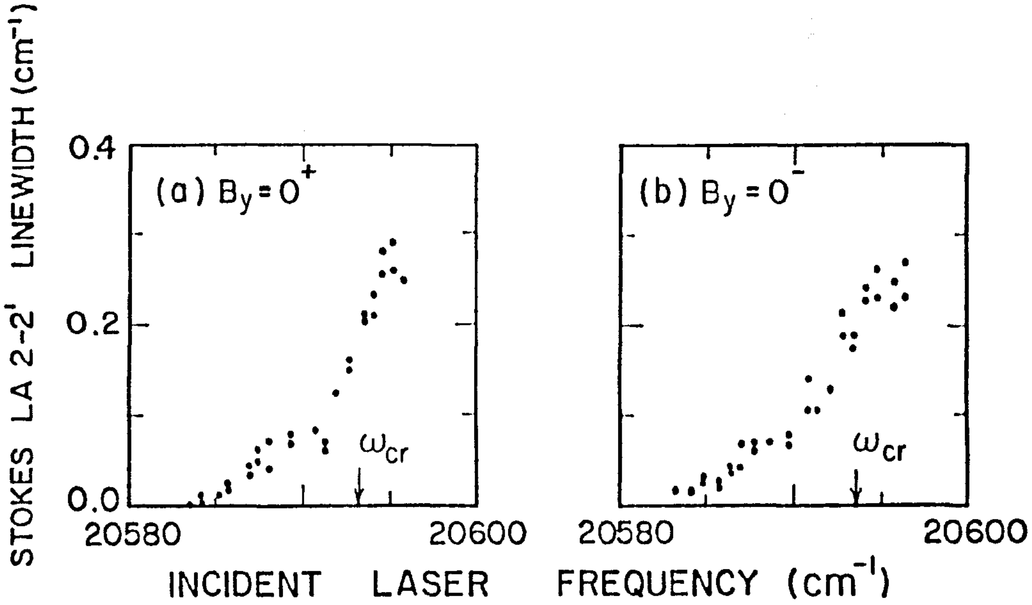
STOKES LA 2-2' LINEWIDTH (cm⁻¹)
0.4
0.2
0.0
(a) B_y = 0⁺
ω_cr
(b) B_y = 0⁻
ω_cr
20580
20600
20580
20600
INCIDENT LASER FREQUENCY (cm⁻¹)

FIG. 5.5

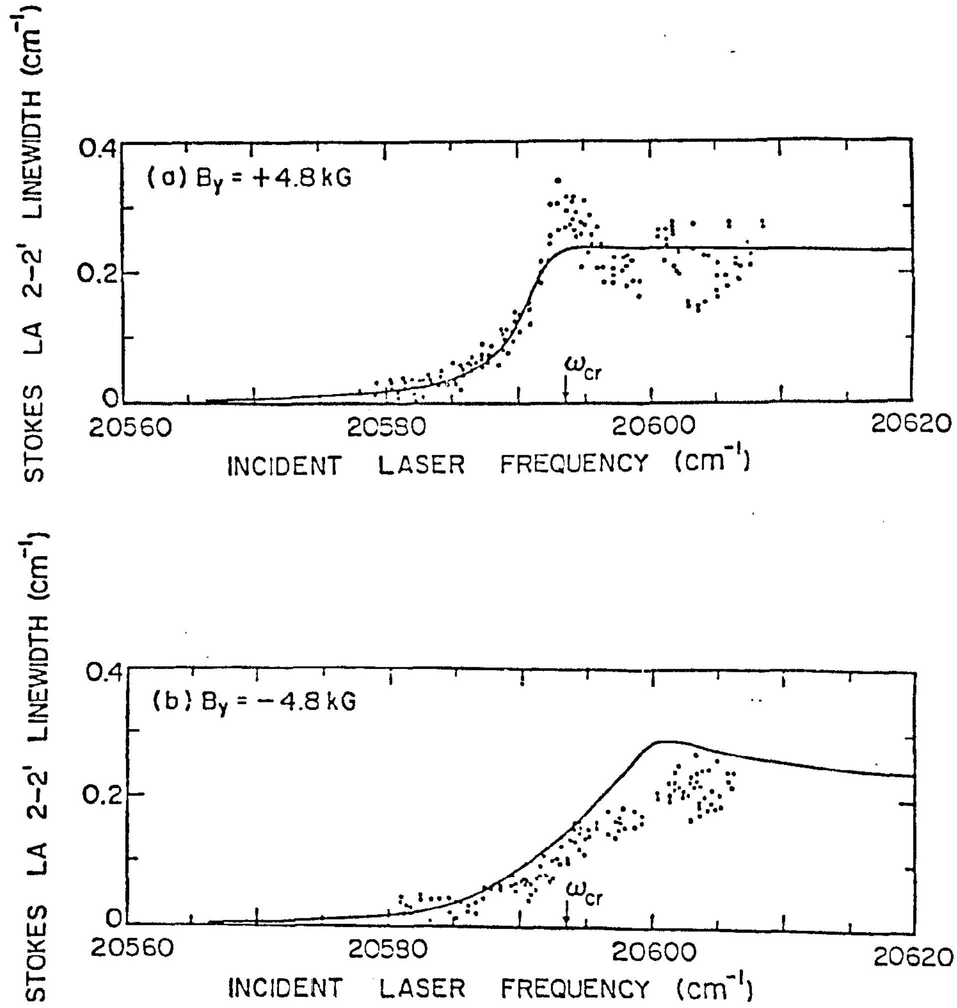
STOKES LA 2-2' LINEWIDTH (cm^{-1})
0.4
0.2
0
(a) B_y = +4.8 kG
ω_{cr}
20560
20580
20600
20620
INCIDENT LASER FREQUENCY (cm^{-1})
STOKES LA 2-2' LINEWIDTH (cm^{-1})
0.4
0.2
0
(b) B_y = −4.8 kG
ω_{cr}
20560
20580
20600
20620
INCIDENT LASER FREQUENCY (cm^{-1})

FIG. 5.6

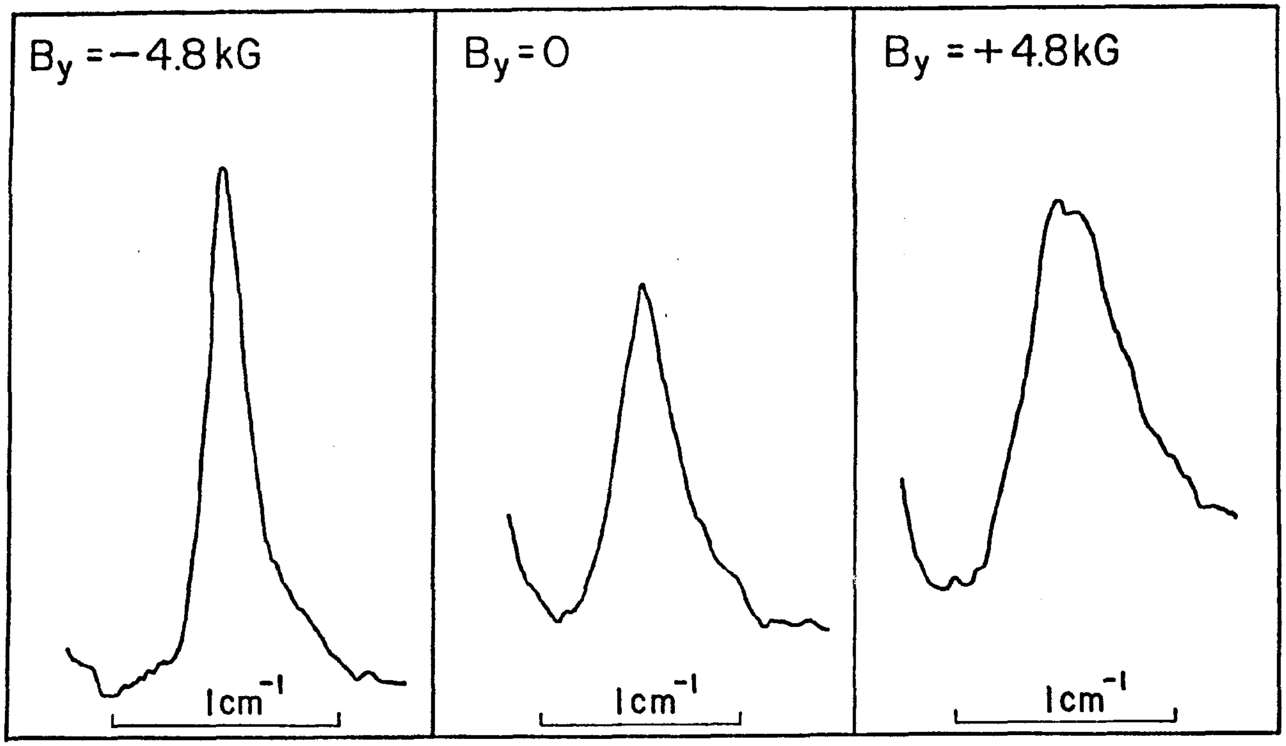

FIG. 5.7

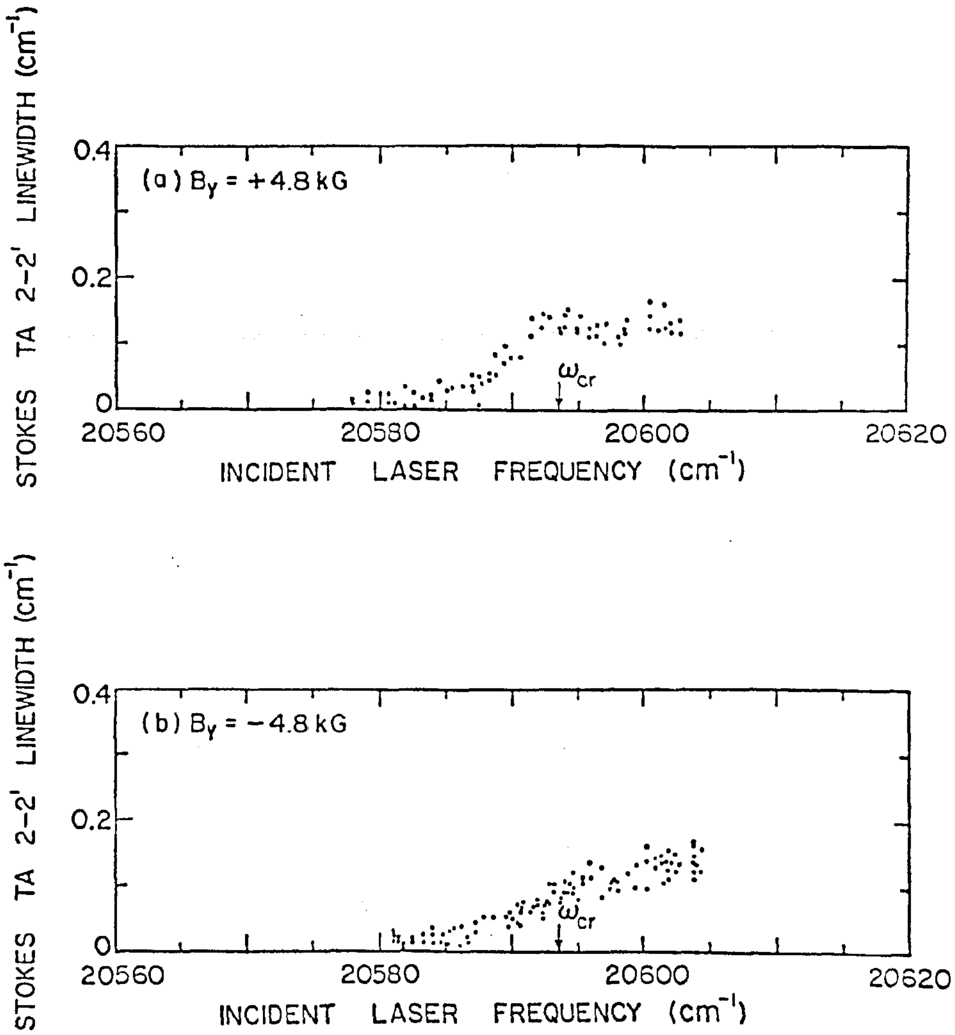
STOKES TA 2-2' LINEWIDTH (cm^{-1})
0.4
0.2
0
(a) B_y = +4.8 kG
ω_{cr}
20560
20580
20600
20620
INCIDENT LASER FREQUENCY (cm^{-1})
STOKES TA 2-2' LINEWIDTH (cm^{-1})
0.4
0.2
0
(b) B_y = −4.8 kG
ω_{cr}
20560
20580
20600
20620
INCIDENT LASER FREQUENCY (cm^{-1})

FIG.5.8

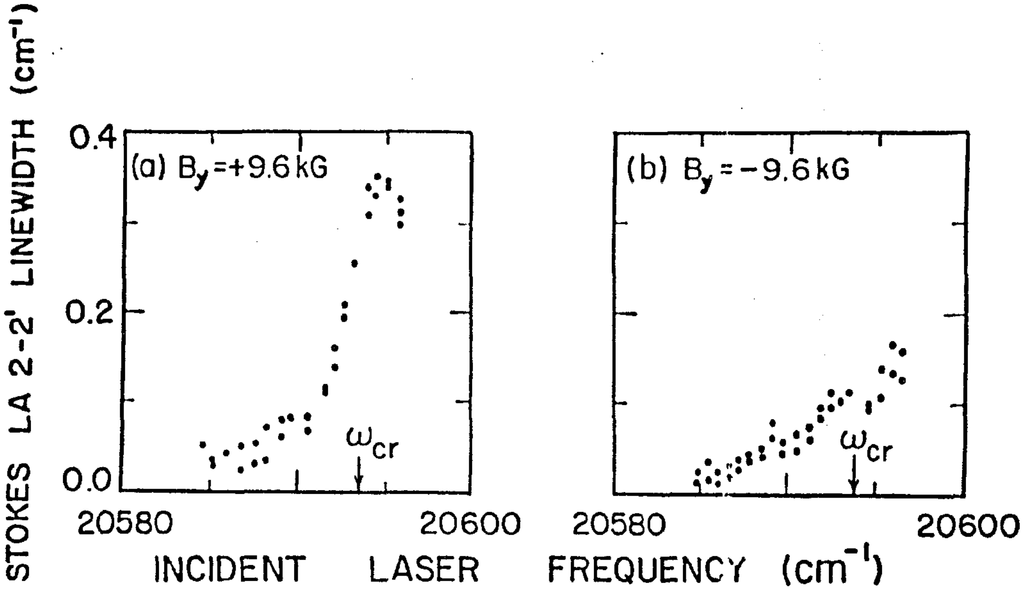
STOKES LA 2-2' LINEWIDTH (cm^{-1})
0.4
0.2
0.0
(a) B_y=+9.6 kG
(b) B_y=−9.6 kG
ω_{cr}
ω_{cr}
20580
20600
20580
20600
INCIDENT LASER FREQUENCY (cm^{-1})

FIG. 5.9

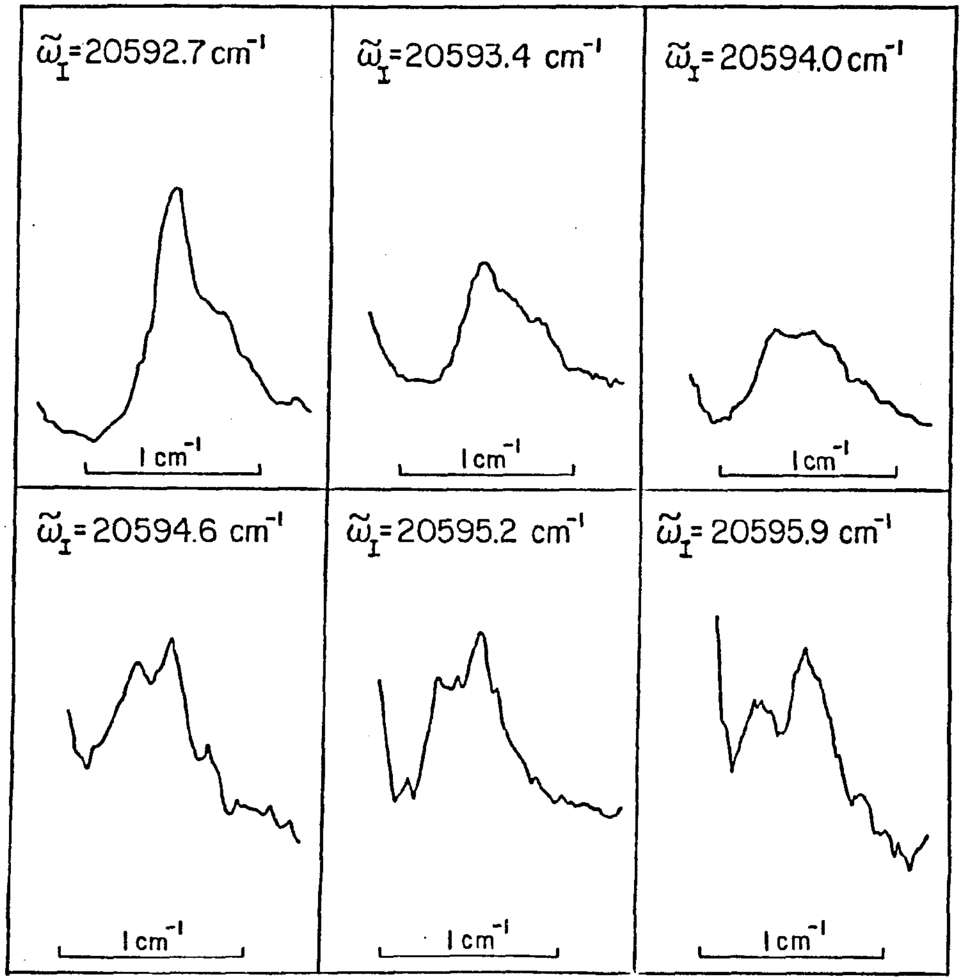
$\tilde{\omega}_I$=20592.7 cm^{-1}
1 cm^{-1}
$\tilde{\omega}_I$=20593.4 cm^{-1}
1 cm^{-1}
$\tilde{\omega}_I$=20594.0 cm^{-1}
1 cm^{-1}
$\tilde{\omega}_I$=20594.6 cm^{-1}
1 cm^{-1}
$\tilde{\omega}_I$=20595.2 cm^{-1}
1 cm^{-1}
$\tilde{\omega}_I$=20595.9 cm^{-1}
1 cm^{-1}

FIG.5.10

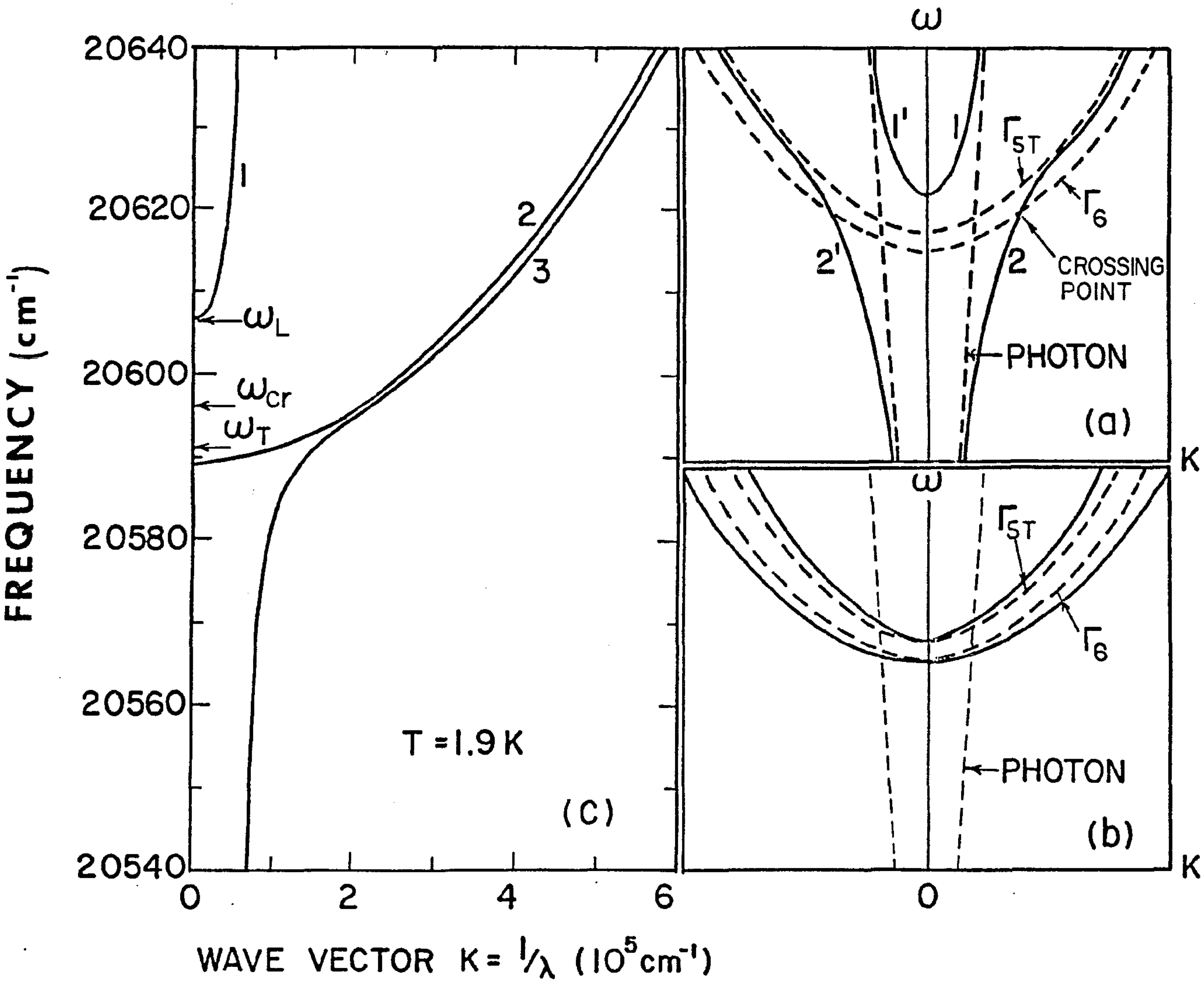

FREQUENCY (cm^{-1})
20640
20620
20600
20580
20560
20540
1
2
3
ω_L
ω_{cr}
ω_T
T = 1.9 K
(c)
0
2
4
6
WAVE VECTOR K = 1/λ (10^{5}cm^{-1})
ω
1'
1
Γ_{5T}
Γ_6
2'
2
CROSSING POINT
PHOTON
(a)
K
ω
Γ_{5T}
Γ_6
PHOTON
(b)
0
K

FIG. 6.1

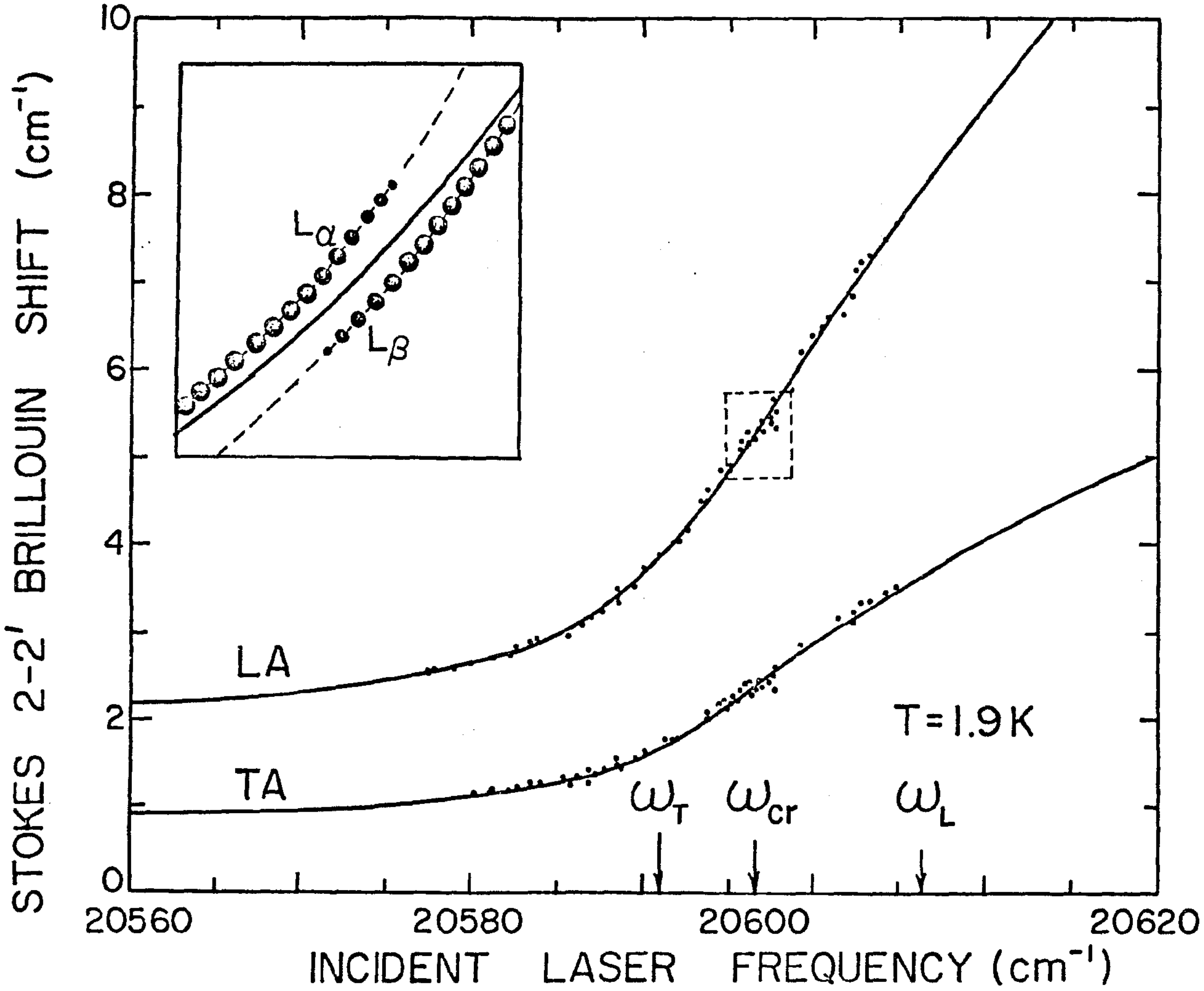
STOKES 2-2' BRILLOUIN SHIFT (cm^{-1})
INCIDENT LASER FREQUENCY (cm^{-1})
0
2
4
6
8
10
20560
20580
20600
20620
LA
TA
T=1.9K
ω_T
ω_{cr}
ω_L
L_α
L_β

FIG. 6.2

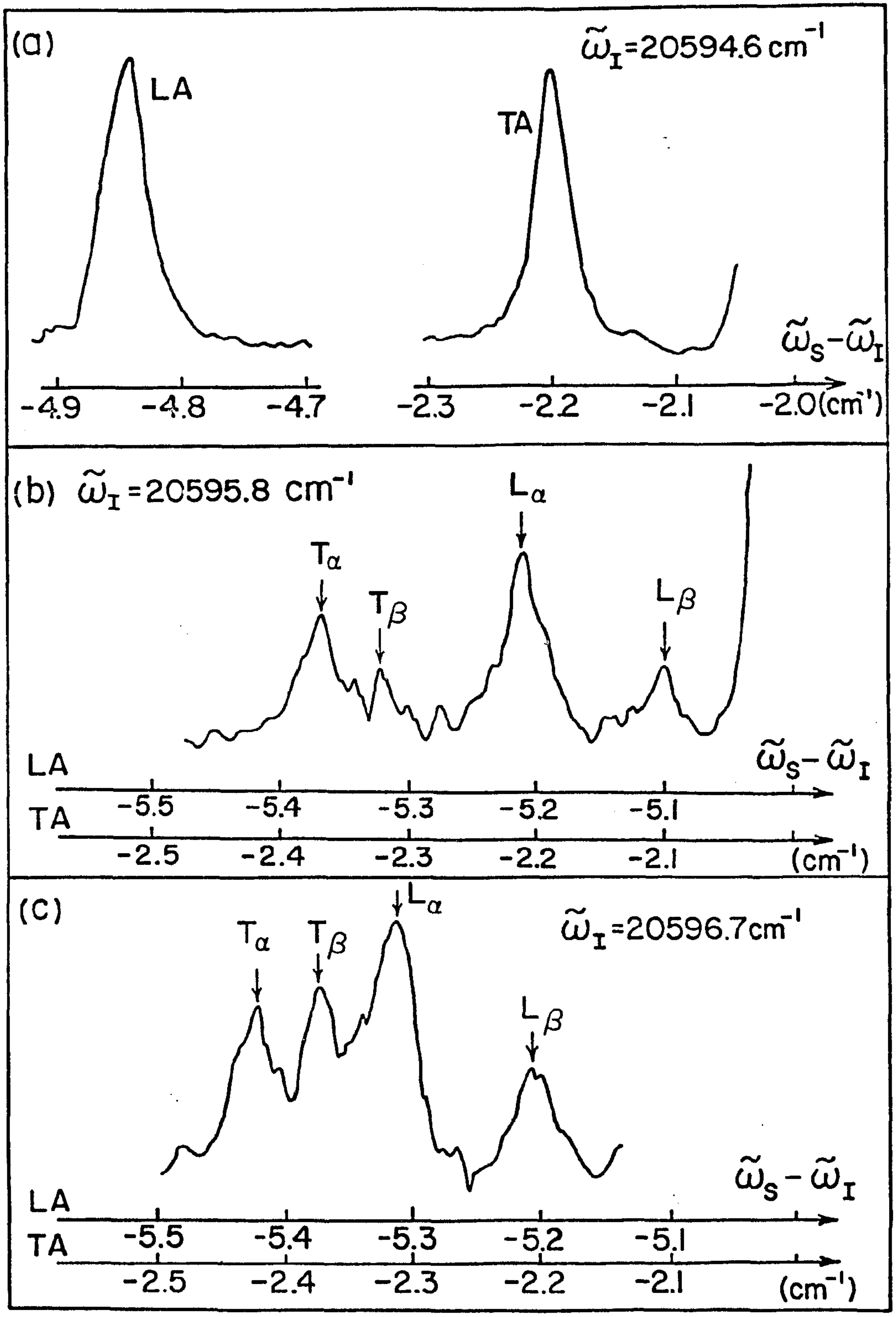
(a)
$\tilde{\omega}_I$=20594.6 cm^{-1}
LA
TA
$\tilde{\omega}_S-\tilde{\omega}_I$
-4.9
-4.8
-4.7
-2.3
-2.2
-2.1
-2.0(cm^{-1})
(b) $\tilde{\omega}_I$=20595.8 cm^{-1}
T_α
T_β
L_α
L_β
LA
TA
$\tilde{\omega}_S-\tilde{\omega}_I$
-5.5
-5.4
-5.3
-5.2
-5.1
-2.5
-2.4
-2.3
-2.2
-2.1
(cm^{-1})
(c)
$\tilde{\omega}_I$=20596.7cm^{-1}
T_α
T_β
L_α
L_β
LA
TA
$\tilde{\omega}_S-\tilde{\omega}_I$
-5.5
-5.4
-5.3
-5.2
-5.1
-2.5
-2.4
-2.3
-2.2
-2.1
(cm^{-1})

FIG.6.3

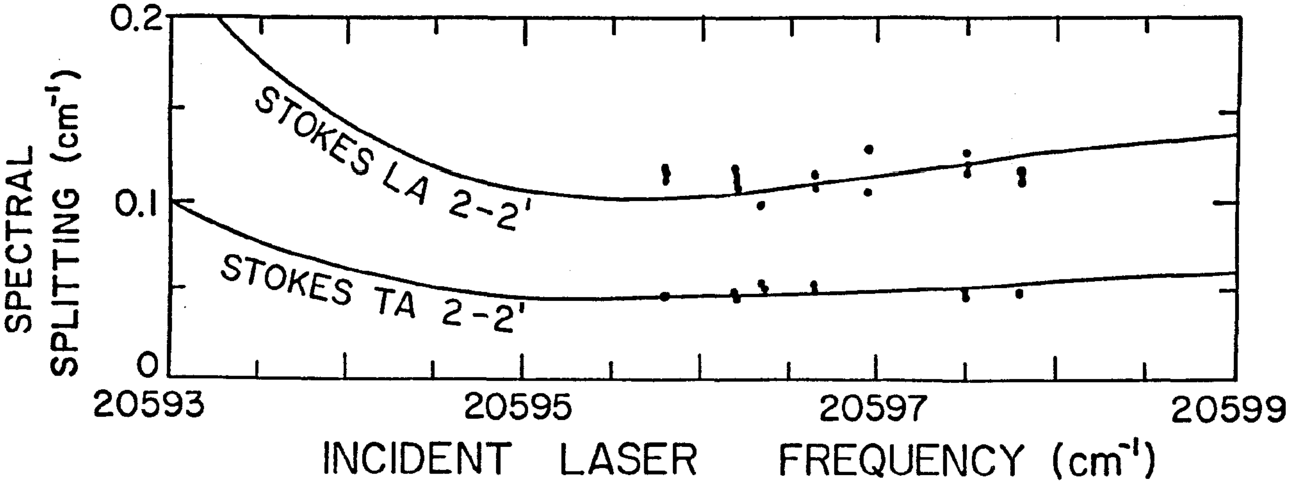
0.2
0.1
0
SPECTRAL SPLITTING (cm^{-1})
STOKES LA 2-2'
STOKES TA 2-2'
20593
20595
20597
20599
INCIDENT LASER FREQUENCY (cm^{-1})

FIG. 6.4

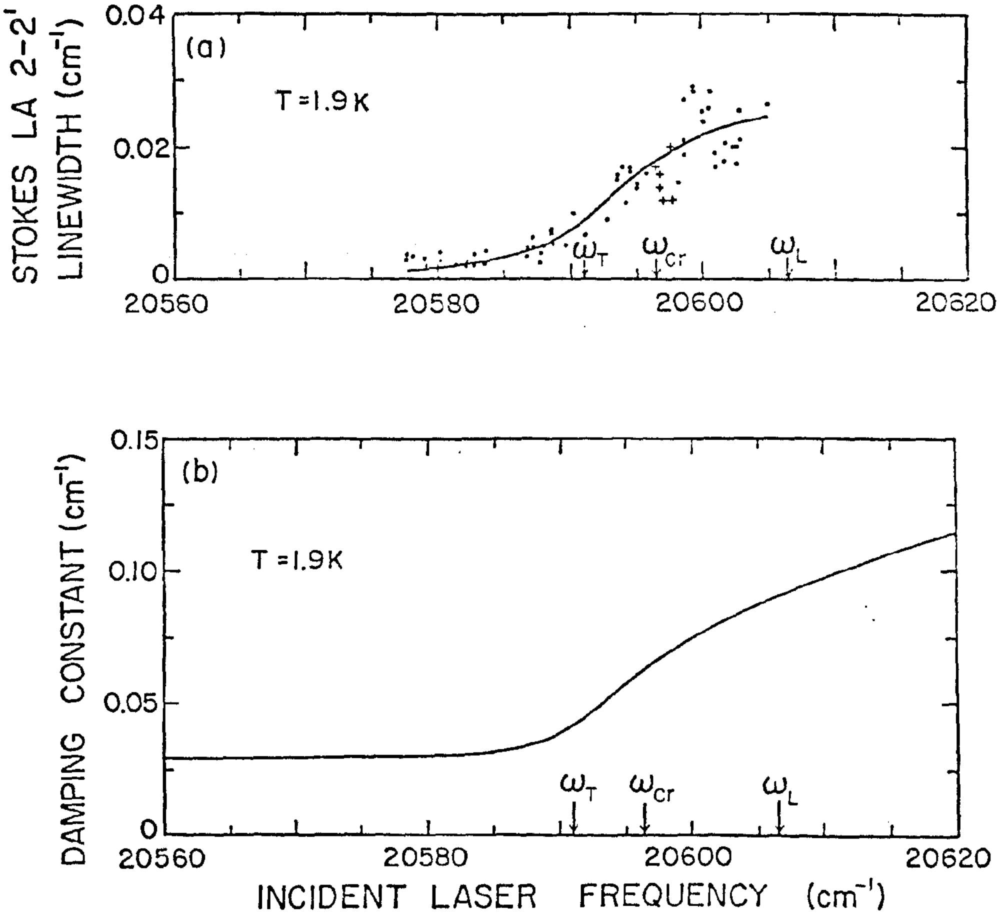
STOKES LA 2-2' LINEWIDTH (cm⁻¹)
0.04
0.02
0
(a)
T = 1.9 K
ω_T
ω_cr
ω_L
20560
20580
20600
20620
DAMPING CONSTANT (cm⁻¹)
0.15
0.10
0.05
0
(b)
T = 1.9K
ω_T
ω_cr
ω_L
20560
20580
20600
20620
INCIDENT LASER FREQUENCY (cm⁻¹)

FIG. 6.5

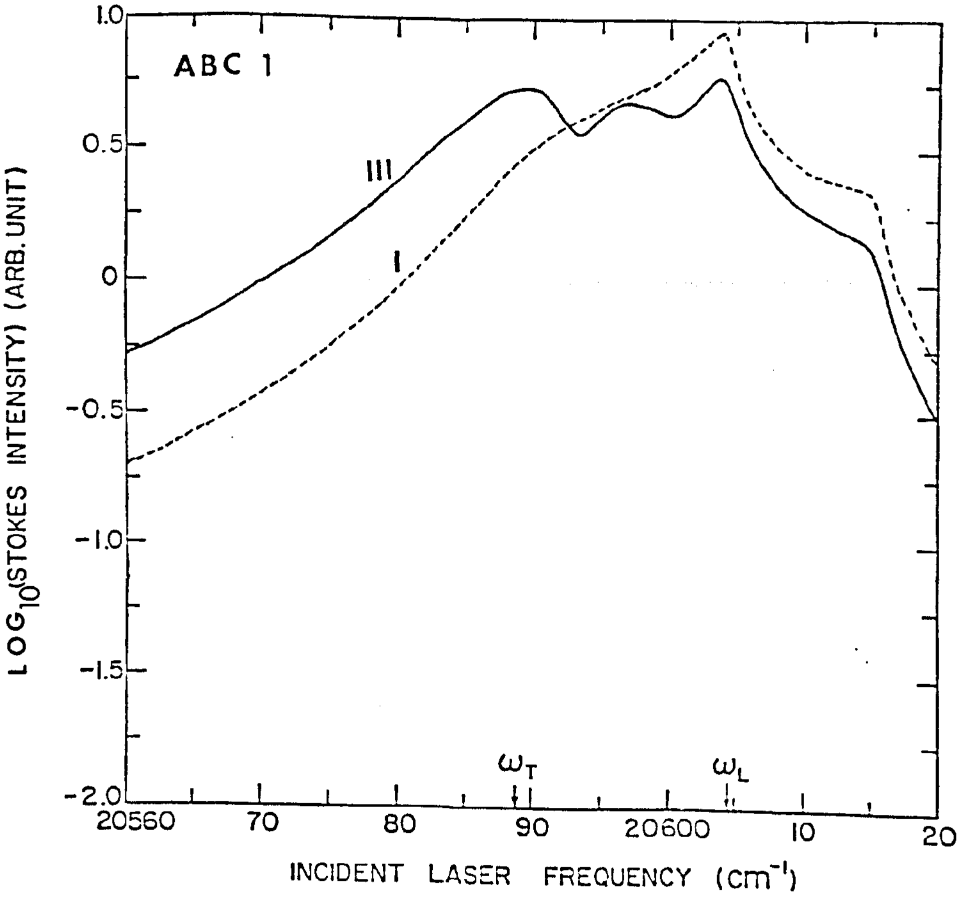
ABC 1
III
I
1.0
0.5
0
-0.5
-1.0
-1.5
-2.0
LOG10(STOKES INTENSITY) (ARB. UNIT)
20560
70
80
90
20600
10
20
ωT
ωL
INCIDENT LASER FREQUENCY (cm-1)

FIG.7.1

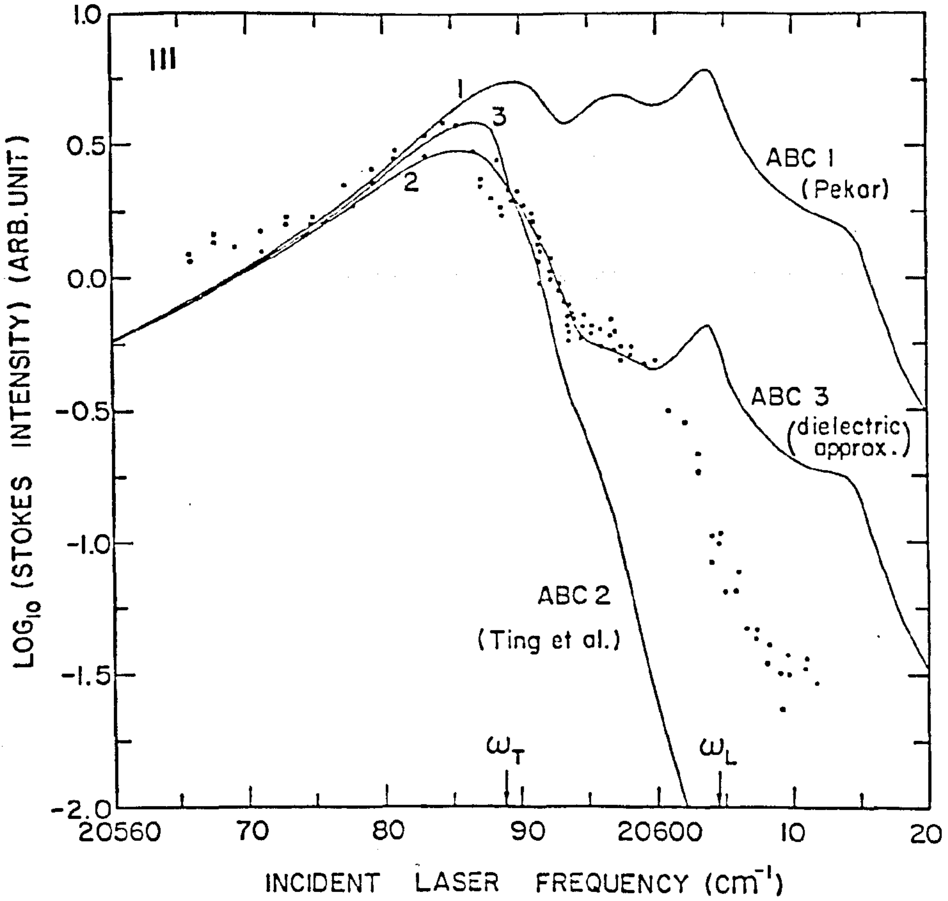
III
1
3
2
ABC 1
(Pekar)
ABC 3
(dielectric approx.)
ABC 2
(Ting et al.)
ω_T
ω_L
1.0
0.5
0.0
-0.5
-1.0
-1.5
-2.0
20560
70
80
90
20600
10
20
LOG$_{10}$ (STOKES INTENSITY) (ARB. UNIT)
INCIDENT LASER FREQUENCY (cm^{-1})

FIG.7.2

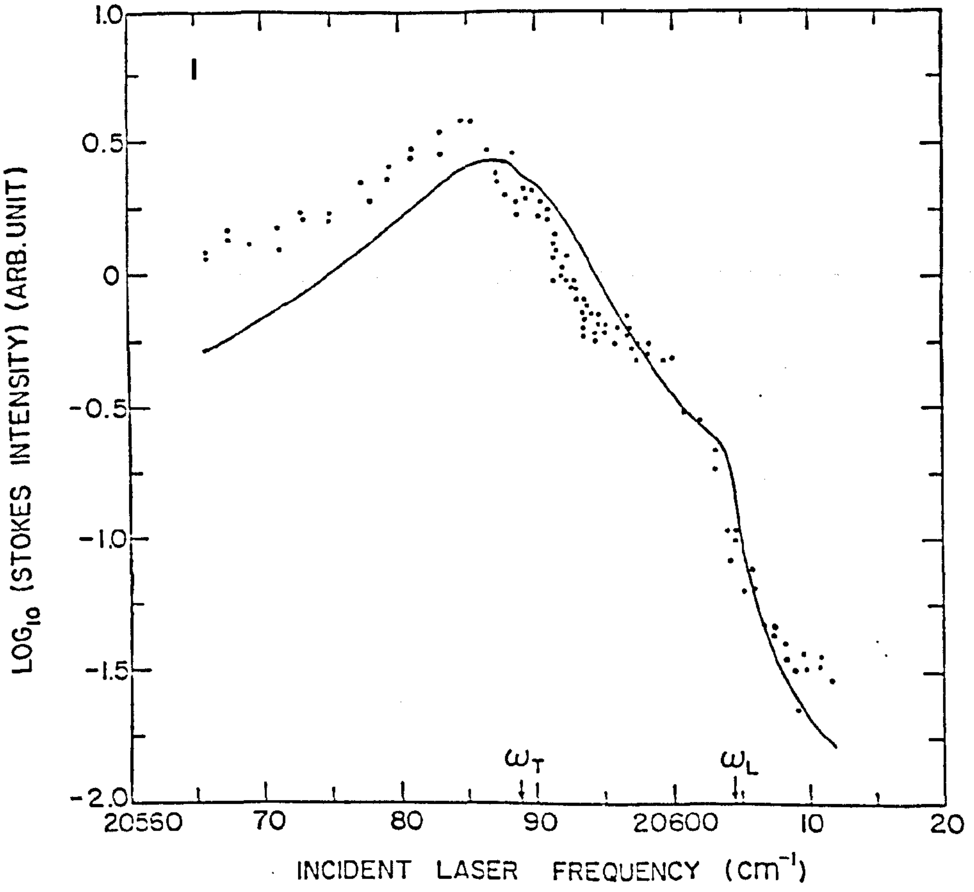
1.0
0.5
0
-0.5
-1.0
-1.5
-2.0
I
LOG$_{10}$ (STOKES INTENSITY) (ARB. UNIT)
ω_T
ω_L
20550
70
80
90
20600
10
20
INCIDENT LASER FREQUENCY (cm^{-1})

FIG.7.3

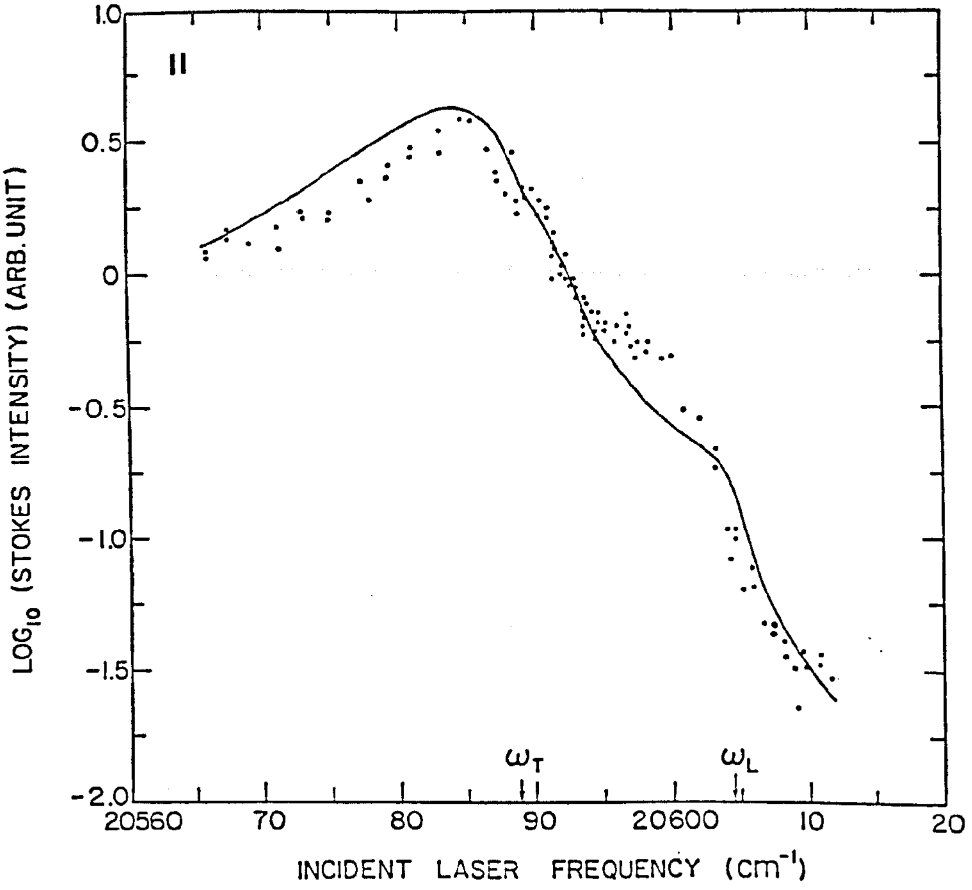

II
1.0
0.5
0
-0.5
-1.0
-1.5
-2.0
LOG$_{10}$ (STOKES INTENSITY) (ARB. UNIT)
20560
70
80
90
20600
10
20
ω_T
ω_L
INCIDENT LASER FREQUENCY (cm^{-1})

FIG.7.4

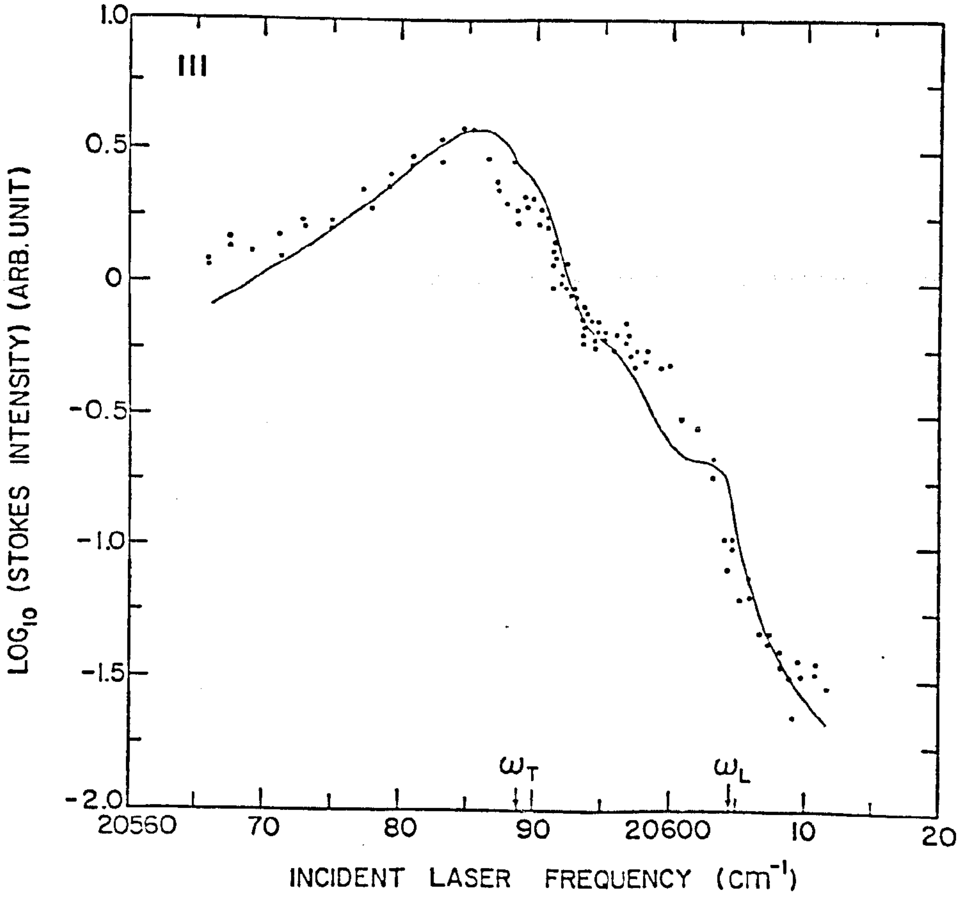
1.0
0.5
0
-0.5
-1.0
-1.5
-2.0
III
LOG$_{10}$ (STOKES INTENSITY) (ARB. UNIT)
ω_T
ω_L
20560
70
80
90
20600
10
20
INCIDENT LASER FREQUENCY (cm^{-1})

FIG. 7. 5

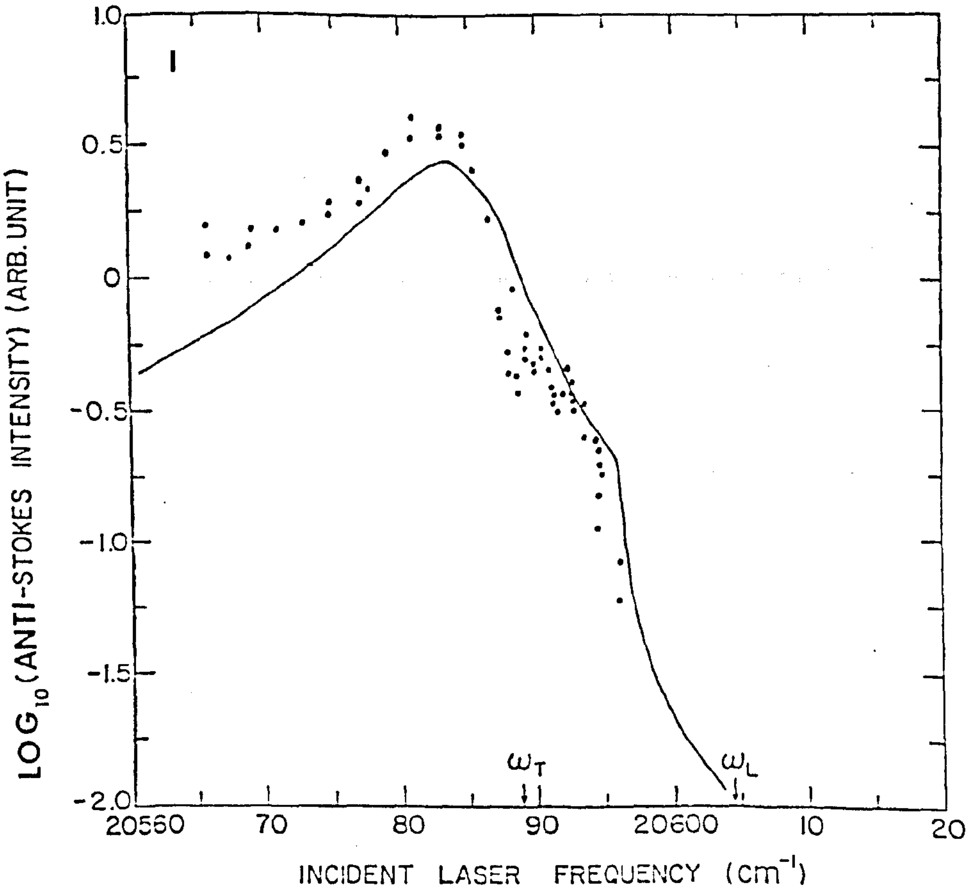
LOG$_{10}$ (ANTI-STOKES INTENSITY) (ARB. UNIT)
1.0
0.5
0
-0.5
-1.0
-1.5
-2.0
I
ω_T
ω_L
20560
70
80
90
20600
10
20
INCIDENT LASER FREQUENCY (cm^{-1})

FIG. 7.6

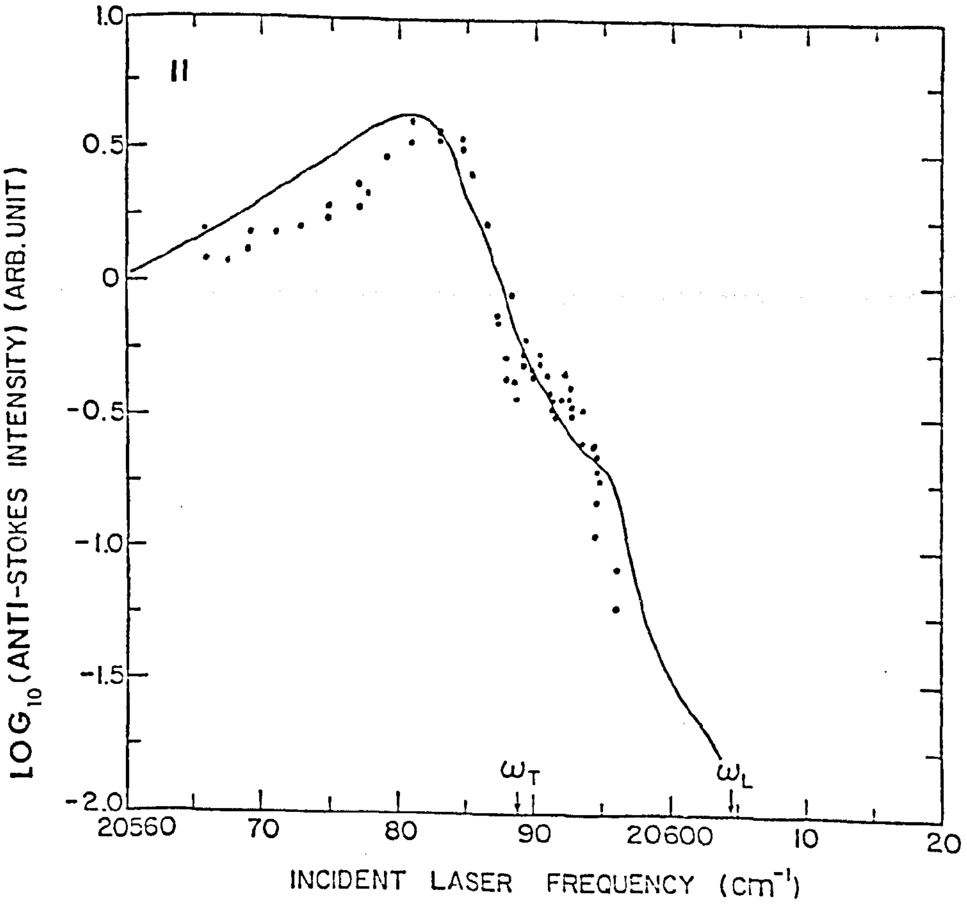
LOG₁₀ (ANTI-STOKES INTENSITY) (ARB. UNIT)
1.0
0.5
0
-0.5
-1.0
-1.5
-2.0
II
ωT
ωL
20560
70
80
90
20600
10
20
INCIDENT LASER FREQUENCY (cm⁻¹)

FIG. 7.7

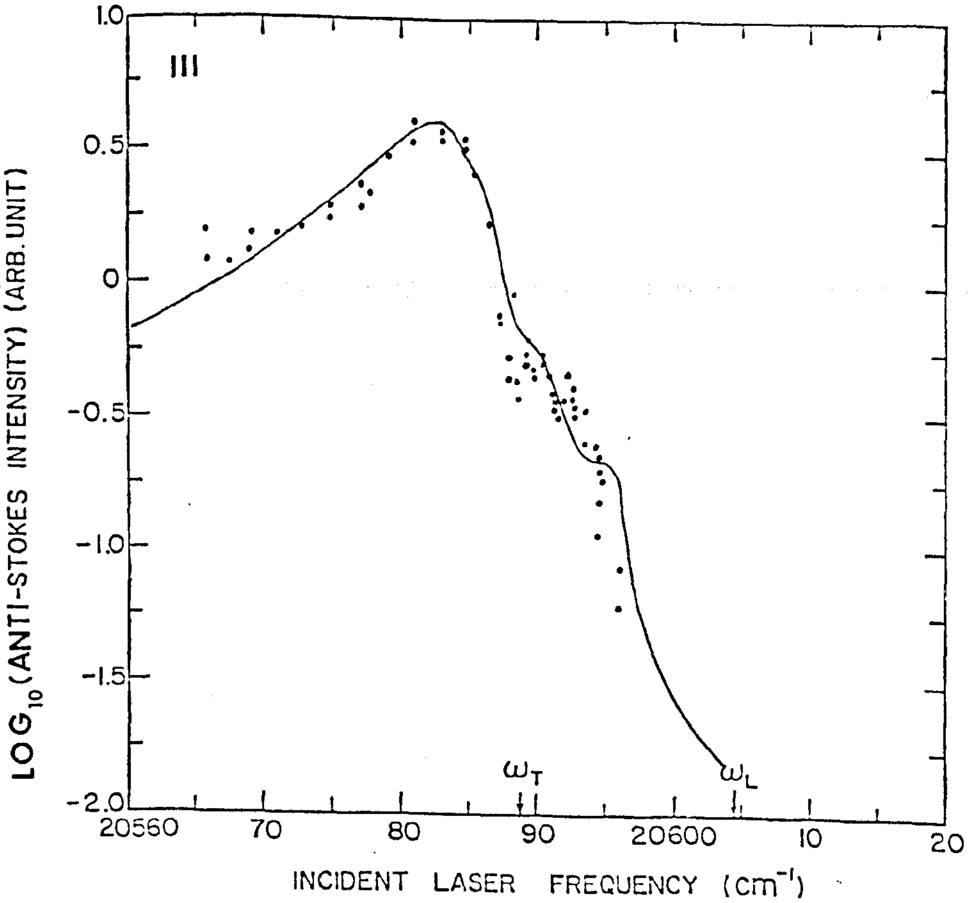
1.0
0.5
0
-0.5
-1.0
-1.5
-2.0
III
LOG$_{10}$(ANTI-STOKES INTENSITY) (ARB. UNIT)
20560
70
80
90
20600
10
20
ω_T
ω_L
INCIDENT LASER FREQUENCY (cm^{-1})

FIG. 7.8

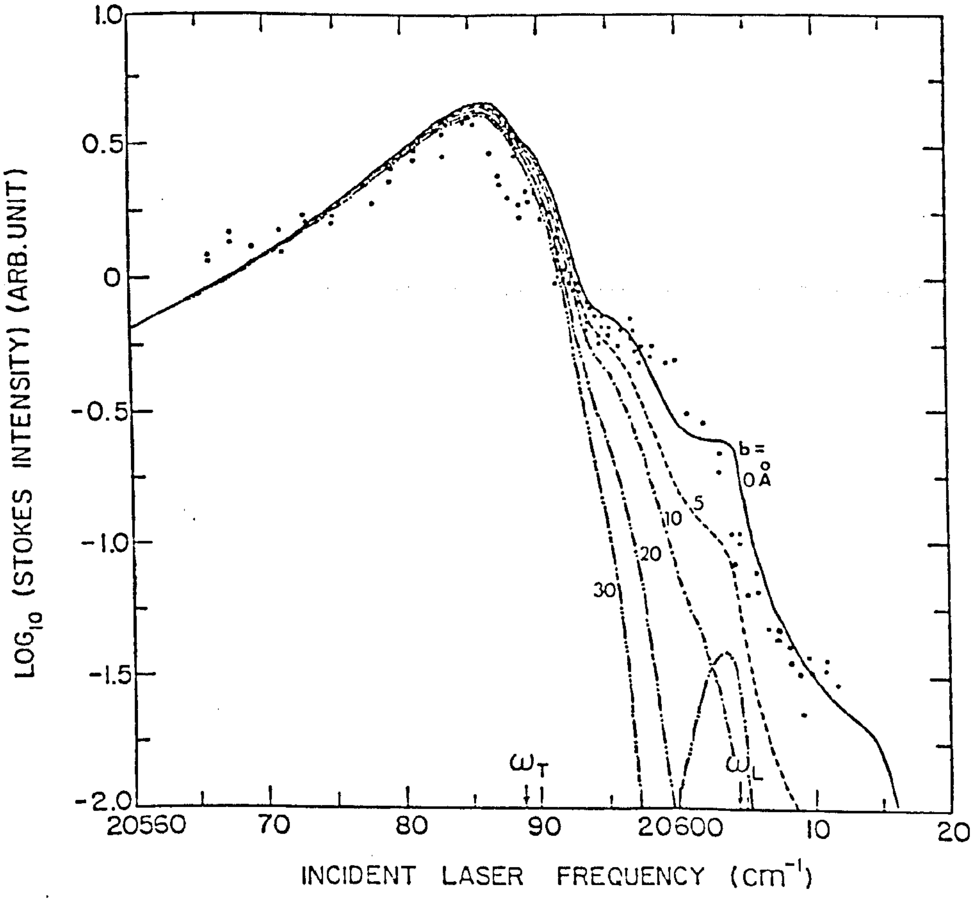
1.0
0.5
0
-0.5
-1.0
-1.5
-2.0
LOG$_{10}$ (STOKES INTENSITY) (ARB.UNIT)
20560
70
80
90
20600
10
20
INCIDENT LASER FREQUENCY (cm^{-1})
ω_T
ω_L
b =
0 Å
5
10
20
30

FIG.7.9

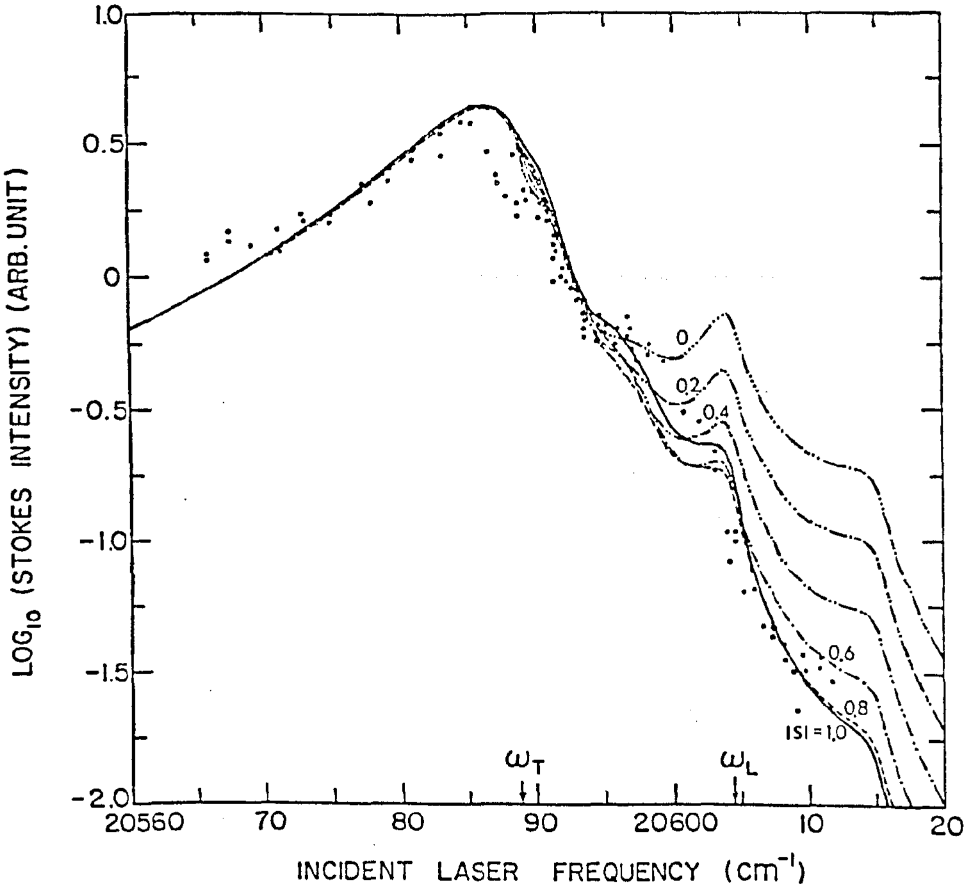
LOG$_{10}$ (STOKES INTENSITY) (ARB. UNIT)
1.0
0.5
0
-0.5
-1.0
-1.5
-2.0
20560
70
80
90
20600
10
20
INCIDENT LASER FREQUENCY (cm^{-1})
ω_T
ω_L
0
0.2
0.4
0.6
0.8
|S| = 1.0

FIG. 7. 10

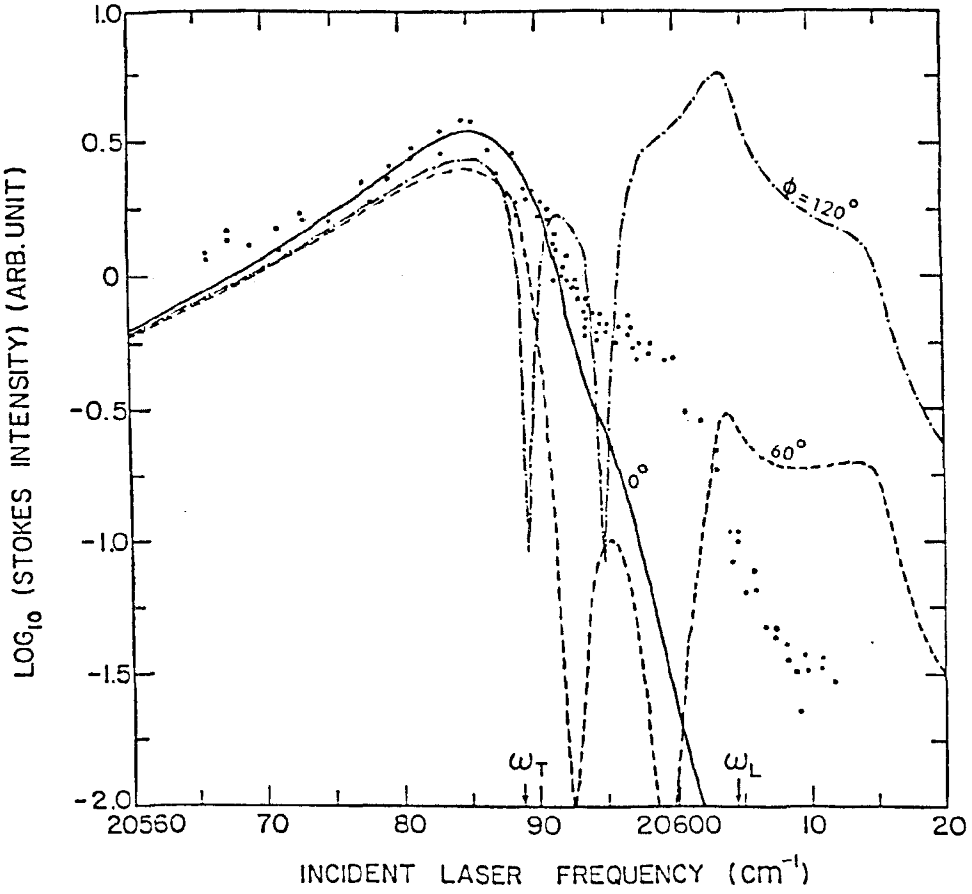
LOG$_{10}$ (STOKES INTENSITY) (ARB. UNIT)
1.0
0.5
0
-0.5
-1.0
-1.5
-2.0
20550
70
80
90
20600
10
20
INCIDENT LASER FREQUENCY (cm^{-1})
ω_T
ω_L
$\phi = 120°$
60°
0°

FIG.7.11

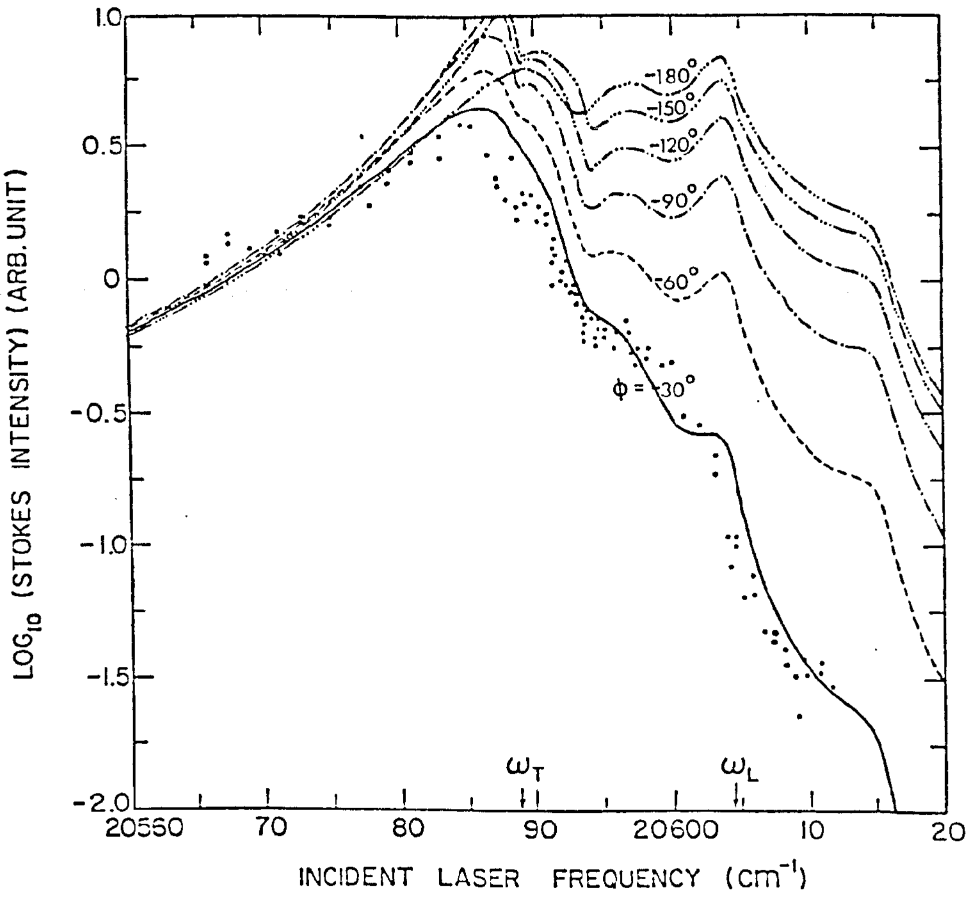
LOG$_{10}$ (STOKES INTENSITY) (ARB. UNIT)
1.0
0.5
0
-0.5
-1.0
-1.5
-2.0
20550
70
80
90
20600
10
20
INCIDENT LASER FREQUENCY (cm^{-1})
ω_T
ω_L
-180°
-150°
-120°
-90°
-60°
ϕ = -30°

FIG. 7.12